2017

# EXPLORING THE STRUCTURE AND PROPERTIES OF NANOMATERIALS USING ADVANCED ELECTRON MICROSCOPY TECHNIQUES

Yao-Jen Chang
*University of Kentucky*, carito7891@gmail.com
Author ORCID Identifier:
http://orcid.org/0000-0002-5515-7254
Digital Object Identifier: https://doi.org/10.13023/ETD.2017.016

STUDENT AGREEMENT:

I represent that my thesis or dissertation and abstract are my original work. Proper attribution has been given to all outside sources. I understand that I am solely responsible for obtaining any needed copyright permissions. I have obtained needed written permission statement(s) from the owner(s) of each third-party copyrighted matter to be included in my work, allowing electronic distribution (if such use is not permitted by the fair use doctrine) which will be submitted to UKnowledge as Additional File.

I hereby grant to The University of Kentucky and its agents the irrevocable, non-exclusive, and royalty-free license to archive and make accessible my work in whole or in part in all forms of media, now or hereafter known. I agree that the document mentioned above may be made available immediately for worldwide access unless an embargo applies.

I retain all other ownership rights to the copyright of my work. I also retain the right to use in future works (such as articles or books) all or part of my work. I understand that I am free to register the copyright to my work.

REVIEW, APPROVAL AND ACCEPTANCE

The document mentioned above has been reviewed and accepted by the student's advisor, on behalf of the advisory committee, and by the Director of Graduate Studies (DGS), on behalf of the program; we verify that this is the final, approved version of the student's thesis including all changes required by the advisory committee. The undersigned agree to abide by the statements above.

Yao-Jen Chang, Student

Dr. Beth S. Guiton, Major Professor

Dr. Mark Lovell, Director of Graduate Studies

# EXPLORING THE STRUCTURE AND PROPERTIES OF NANOMATERIALS USING ADVANCED ELECTRON MICROSCOPY TECHNIQUES

DISSERTATION

A dissertation submitted in partial fulfillment of the requirements for the degree of Doctor of Philosophy in the College of Arts and Sciences at the University of Kentucky

By
Yao-Jen Chang
Lexington, KY

Director: Dr. Beth S. Guiton, Assistant Professor of Chemistry
Lexington, KY 2017

ABSTRACT OF DISSERTATION

EXPLORING THE STRUCTURE AND PROPERTIES OF NANOMATERIALS USING ADVANCED ELECTRON MICROSCOPY TECHNIQUES

Nowadays people are relying on all kinds of electronic devices in their daily life. All these devices are getting smaller and lighter with longer battery life due to the improvement of nanotechnology and materials sciences. Electron microscopy (EM) plays a vital role in the evolution of materials characterization which shapes the technology in today's life. In electron microscopy, electron beam is used as the illumination source instead of visible light used in traditional optical microscopy, the wavelength of an electron is about $10^5$ times shorter than visible light. By taking this advantage, the resolving power and magnification are greatly improved which gives us the ability to understand the morphology and the structure of smaller materials.

Besides high resolution and high magnifications, the electron-matter interactions in electron microscopy are also very interesting and provide useful information. Typically, there are three types of post electron-matter interaction electrons, and they are: secondary electrons, backscattered electrons and transmitted electrons. Different signals are carried out with these electron-matter interactions, the most common techniques including electron dispersive X-ray spectroscopy (EDS), electron energy loss spectroscopy (EELS) and selected area electron diffraction (SAED). In this dissertation, I will discuss how electron microscopy techniques approach complicated nanostructures, such as $MnSb_2Se_4$ nanorods to reveal the composition, structure, surfactant controlled size, and relative magnetic properties. Other important features such as mapping localized surface plasmon resonance (LSPR) using EELS and newly developed liquid cell scanning mode transmission electron microscopy (STEM) in situ observation are also presented.

KEYWORDS: transmission electron microscopy, electron dispersive spectroscopy, electron energy loss spectroscopy, selected area electron diffraction, localized surface plasmon resonance, *in situ*

Student's signature: Yao-Jen, Chang

Date: January 24, 2017

EXPLORING THE STRUCTURE AND PROPERTIES OF NANOMATERIALS USING ADVANCED ELECTRON MICROSCOPY TECHNIQUES

By

Yao-Jen, Chang

Dr. Beth S. Guiton
Director of Dissertation

Dr. Mark Lovell
Director of Graduate Studies

January 24, 2017

ACKNOWLEDGEMENTS

The process of getting a Ph.D degree could be frustrating, tedious, and tiring. I am very lucky to have a lot of help from some great people. First of all, I am very glad I choose Dr. Beth Guiton as my research adviser. A great amount of time in my graduate student life, I had to perform experiments in Oak Ridge National Laboratory and University of Tennessee-Knoxville with more advanced transmission electron microscopes. These experiences have an extraordinary importance because I got to learn from some top scientists and use the most advanced equipment. None of this could happen without Dr. Beth Guiton's help. Dr. Beth Guiton not only served as a great academic adviser, but also provided experiences in taking good care of my new born daughter. I really could not ask for a better adviser.

I would also like to thank my committee members: Dr. Dong-Sheng Yang, Dr. Folami Ladipo, and Dr. Todd Hastings. Thanks for asking me some tough questions and guiding me to the right direction in our meetings.

Many people helped me during this long journey of graduate school. Specials thanks to Dr. John Dunlap, Dr. Mengkun Tian, Dr. Gred Duscher, and Dr. Jinxuan Ge for helping me on the TEM at UTK. I would also like to thank Dr. Ray Unocic, Dr. Andy Lupini, Dr. Iberi Vighter, and Dr. Juan-Carlos Idrobo for teaching me a lot of useful skills in electron microscopy at ORNL.

It would be so much more difficult to finish this long journey of graduate school if I did not have good relationships with my lab mates. I am very proud to say that Guiton lab has the best atmosphere in the chemistry department. People in this lab are very friendly,

and most importantly, we support each other. I really appreciate the friendships and supports from all my lab mates.

Many thanks to Evie Zhou for all the coffee breaks and gossiping. You are such a hard worker; I truly believe you deserve a good career. Never give up!

I could not say enough thanks to Alice Hsu. A lot of things would not happen without your support. Thanks for everything! Wish you all the best to your career!

Finally, I want to thank my family for their long-term support both financially and mentally. My baby daughter, Chloe, is my little angle. I wish you grow up happily and healthy. This is the first Ph. D degree in Chang's family, more to come in the future.

TABLE OF CONTENTS

LIST OF FIGURES

# Chapter 1: Introduction

## 1.1 Motivation

Nanostructured solid-state materials have been extensively studied in the past 30 years due to their strong demands in various types of technology.[1-6] It is extremely important to study the morphology, surface, structure, and the interesting physical/chemical properties before we can improve the synthesis, fabrication, and applications.[7] The characteristics of materials in nano-scales can be very different from their bulk characteristics, even with the same chemical composition. In nanostructured materials, the phenomena of large surface-to-volume (S/V) ratio not only greatly increases the reactivity of the material, but also increases the surface energy enormously because a larger fraction of atoms are exposed to the environment.[8]

In order to fully understand the properties of low dimensional nanostructured materials, it is necessary to carefully study the materials from many different levels. In the most fundamental level, the atomic structures are studied to predict the bonding, valence states, and magnetic properties. In the mid-levels, the crystal structure, inter-molecular forces, and electronic structure are the most investigated areas. In the advanced levels, the kinetics, thermodynamics, optical properties, and many other important properties are studied because they directly related to their performance and applications.[9-13] All these properties mentioned above are a multidisciplinary field which overlaps physical chemistry, crystallography, electrochemistry, solid-state physics, and various other emerging fields. A single instrument or method that cannot do all the analysis work and reveal all the information of a given nanostructured material. Traditional optical microscopy has limits since the probe size is limited within visible

light range, and the detection limit is not sufficient to investigate the materials in nano-scales.[14]

The use of electron microscopy (EM) becomes an essential tool for nanostructured materials characterization. Thanks to the wavelength of an electron is about $10^5$ times shorter than visible light. Utilizing an electron beam as the probe, the resolving power and magnifications are greatly improved.[15] The associated techniques in EM provides a wide range of information helping us to understand the morphology, topology, chemical composition, crystal structure, valence state and even plasmon behaviors of the materials.

In this dissertation, the background of EM and its associated techniques will be broken down into different sections and will discussed in detail.

### 1.2 Electron microscopy

Electron microscopes were first invented in the 1930's and have since become a standard characterization tool in modern science.[16] All kinds of new technologies have been added to the electron microscope to introduce multi-functionality and improve the image quality. For the projects described in this paper we use both scanning electron microscopes (SEMs) and transmission electron microscopes (TEMs) available through the Electron Microscopy Facility at University of Kentucky, as well as scanning TEMs (STEMs), available to us at Oak Ridge National Laboratory. Both SEMs and TEMs are able to create high resolution images at high magnification, but utilize different electron beam-matter interactions. An SEM works by scanning a relatively low energy electron beam over the sample specimen in a raster scan pattern, whereas a TEM works by high energy electrons transmitting through the sample specimen. Secondary interactions of the

electrons with the sample enable compositional analysis techniques such as energy dispersive x-ray spectroscopy (EDS) and electron energy loss spectroscopy (EELS), as well as imaging capabilities.

### *1.2.1 Scanning electron microscopy*

SEM is a very powerful tool for elemental composition analysis and surface structure characterization. It is very convenient that there's no further preparation needed for the sample, since a dry as-grown substrate can be inserted into the SEM right after the reaction is done so that the original morphology of the sample remains intact. When electrons hit the sample, interactions between electrons and the atoms of the sample will cause the electron beam to lose energy in several different ways, producing different signal types including back-scattered electrons (BSE), characteristic X-rays (for EDS), cathodoluminescence (CL), specimen current, transmitted electrons and secondary electrons (SE). The signals from the sample are shown in Figure 1.1. At the accelerating voltages used in an SEM most of the incident electrons are scattered as SEs. BSE and SE are used for sample imaging since BSEs demonstrate contrast in composition and SEs measure sample morphology. In order to collect as much information as possible, multiple detectors are needed and some of the signals can be collected simultaneously. The SEM data presented in this thesis were taken on a Hitachi S4300SE with a maximum of 25 nA current at 20 kV. Transmission electron microscopy will be discussed in a separate section.

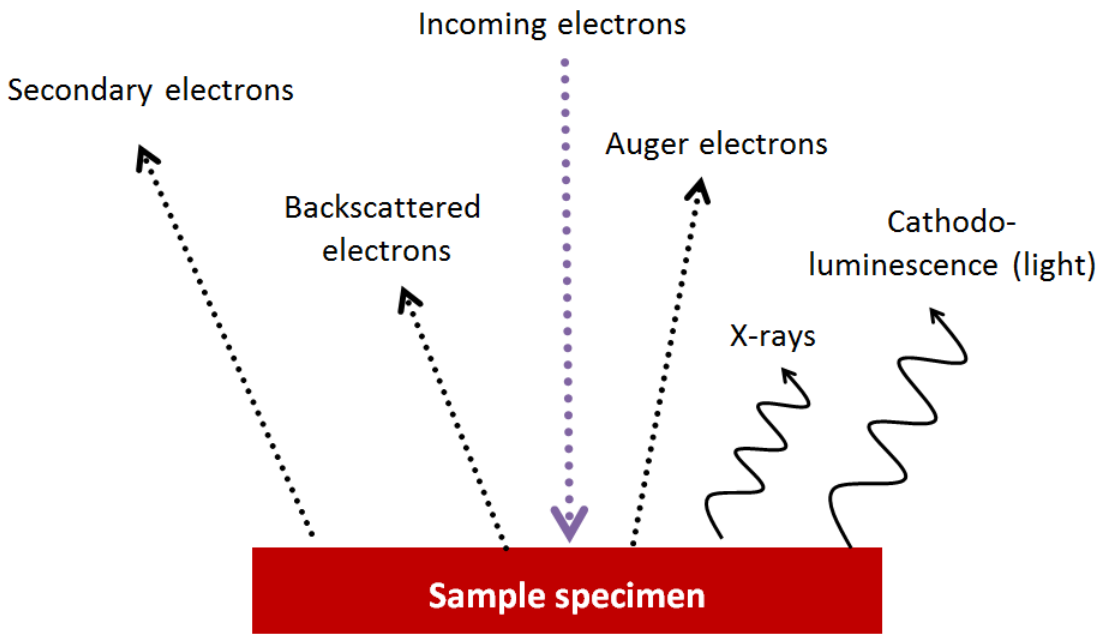


**Figure 1.1** Signals from the sample in an SEM.

## 1.3 Transmission electron microscopy

### *1.3.1 Introduction*

Transmission electron microscopy has been used as an essential multipurpose characterization technique for solid-state materials. Because there's no other equipment in this field can provide the same diversity of information for nanomaterials characterization. Conventional TEMs can easily reach sub-nanometer resolution, whereas the aberration corrected TEM is capable of reaching atomic resolution. Other than regular bright-field morphology characterization, scanning mode TEM (STEM) is also a powerful characterization method. In this method, the electron beam is converged into a fine spot and scanned on solid-state materials and generate dark-field images which are known as Z-contrast images. Z-contrast images are generated based on atomic numbers of the elements presented in the materials. Other associated techniques such as (SAED),

EDS and EELS are also powerful for resolving crystal structure, chemical compositional analysis, and compositional/electronic states/plasmon behaviors analysis respectively. The principles of all the techniques mentioned above will be discussed in detail in later sections; and the applications in different projects will be presented in chapter 3 to 6.

### *1.3.2 Principle of transmission electron microscopy*

Analogously to a conventional optical microscope, TEM uses high energy electrons in place of electromagnetic radiation, to pass through a very thin sample specimen; due to the electrons' far shorter wavelength than visible light, high resolution imaging results. The quality of images can be improved by raising the accelerating voltage, since according to de Broglie wavelength relation energy and wavelength are inversely proportional, and also in recent years with the use of aberration-correction. The TEM can be broken down conceptually into three major parts: a. the illumination system, b. the objective lens/stage, and c. the imaging system.

a. The illumination system can be further separated into two major parts: 1. the electron gun which is the electron source, and 2. the condenser lenses which are used to guide electrons from the source to the sample specimen and also to the focus electron beam to a desired diameter. The illumination system is operated in two modes: a parallel mode which is used for TEM imaging, and a convergent mode which is used for STEM.

b. The objective lens and the specimen stage system is where all of the electron-sample interactions occur. Images and diffraction patterns are created and magnified in this system and they are subsequently viewed and recorded.

c. The imaging system consists several lenses in order to magnify the signals or the diffraction patterns generated by the objective lens and then focus the signal which then captured by charge-coupled device (CCD) camera, a detector, or TV camera. Images are presented on a fluorescent screen or digitized by CCD or TV camera.

Electrons are manipulated by magnetic field lenses to focus and guide them as they travel through the vacuum in the column of the microscope. The signals are generated in many forms when electrons travel through and interact with the sample. Unlike SEM, other than back scattered radiation and electrons, there is the direct beam (which passes through the sample specimen without interaction), elastically scattered electrons (which have no or negligible energy loss after interaction with sample) and inelastically scattered electrons (in which energy is transferred to the sample specimen to generated a few different forms of signals). The elastically scattered electrons are used in the TEM for imaging and electron diffraction methods. The signals generated by inelastically scattered electrons are mainly used in analytical electron microscopy methods. The TEM image contrast depends on the effect of Z (atomic) number of the material and the effect of electron density lying in the path of the electron beam. Combining these two effects produces so called mass-thickness contrast. The electrons are mostly scattered forward with smaller angles when interacting with low Z materials, and the electrons are partially back scattered and mostly scattered forward with higher angles causing beam broadening when interacting with high Z materials. More electrons are scattered in thicker samples than in thinner ones and result in darker regions. The bright field (BF) images are analog images of variations of electron density on the image plane of the objective lens

generated by the direct beam while the scattered electrons are blocked by the objective aperture. Spherical and chromatic aberrations limit the TEM resolution due to the intrinsic imperfection of the electron lens; when extra “lenses” are installed in order to improve these problems, the extra lens is called an aberration corrector. The TEM/STEM imaging in this paper was done using a JEOL 2010F (S)TEM with an acceleration voltage of 200 kV (UK), a Hitachi HF3300 operating at 100 and 300kV (ORNL), and a Nion UltraSTEM (ORNL) operating at 60 and 100kV.

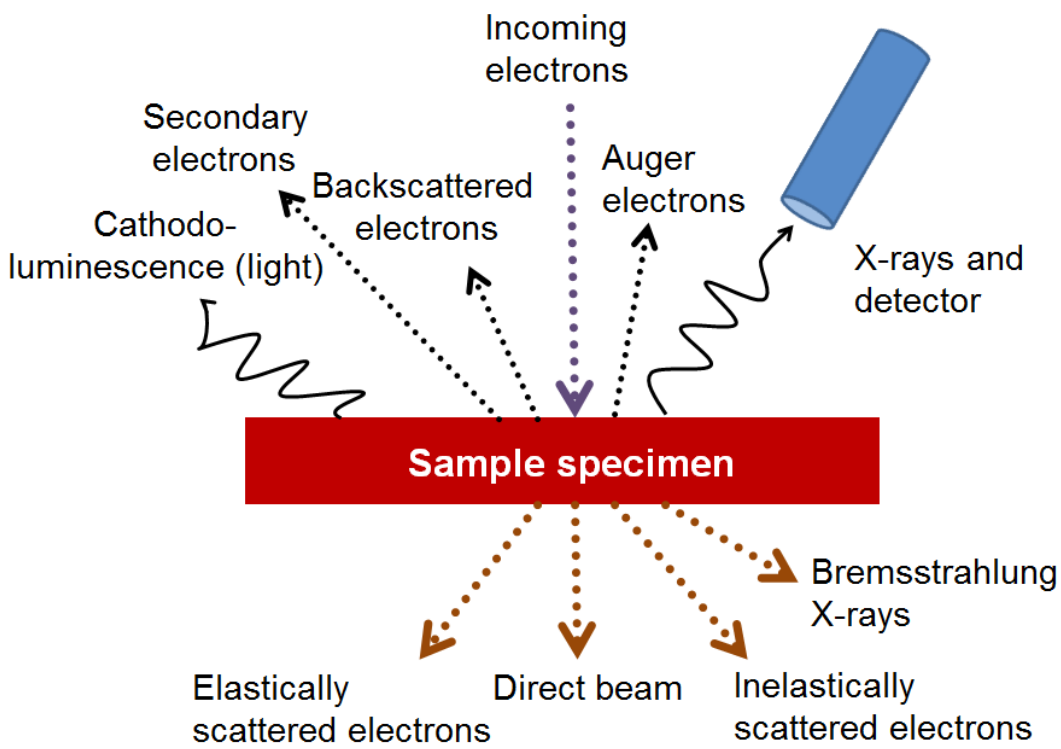


**Figure 1.2** Electron-sample interactions in the TEM.

### *1.3.3 Scanning mode TEM*

Scanning Transmission Electron Microscopy (STEM) combines the principles of TEM and SEM. Unlike TEM, the specimen in STEM is illuminated with a convergent electron beam as shown in Figure 1.3 and scanned in a raster pattern to collect data in a serial acquisition mode. In order to do so, additional scanning coils, detectors and circuitry are necessary to install on a conventional TEM. The secondary or backscattered electrons can be used for imaging in both SEM and STEM, but higher signal levels and better spatial resolution are available by detecting transmitted electrons when using the higher accelerating voltages utilized by STEM. Many characterization techniques are available during scanning such as EDS, EELS, bright field imaging, and annular dark-field (ADF) imaging,[18] and these signals can be acquired simultaneously with multiple detectors to collect complementary data.

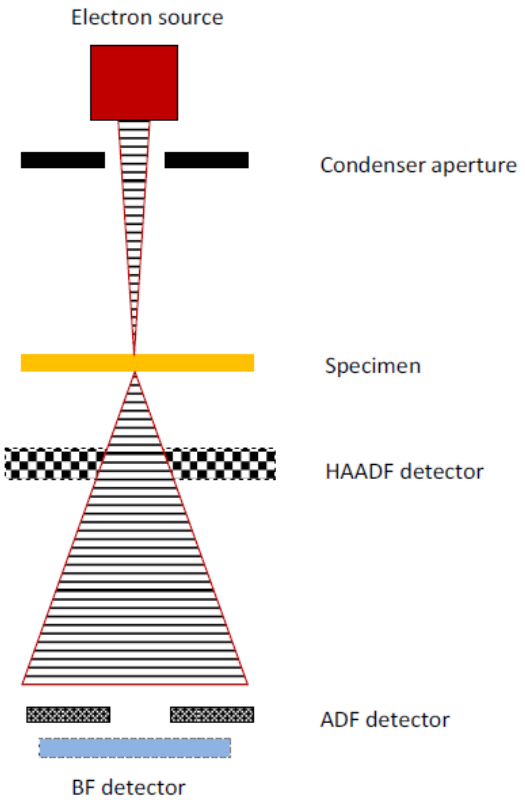


**Figure 1.3** BF, ADF and HAADF detectors set up in STEM.[30] (Figure adapted from Ref. 30)

### *1.3.4 Z-contrast imaging*

In STEM the transmitted electrons, depending on the scattering angle, can be collected by different detectors in different regions as shown in Figure 1.4. The ADF detector is placed to surround the transmitted beam (the bright field region) to collect scattered electrons. The inner angle of this detector can be increased to several times higher than its minimum angle to reach the maximum efficiency of collection of the scattered electrons. At sufficiently high angle this technique is called high angle ADF (HAADF) or Z-contrast imaging, due to the strong dependence of the intensity of signal on the HAADF detector on the atomic number (Z).[19,20]

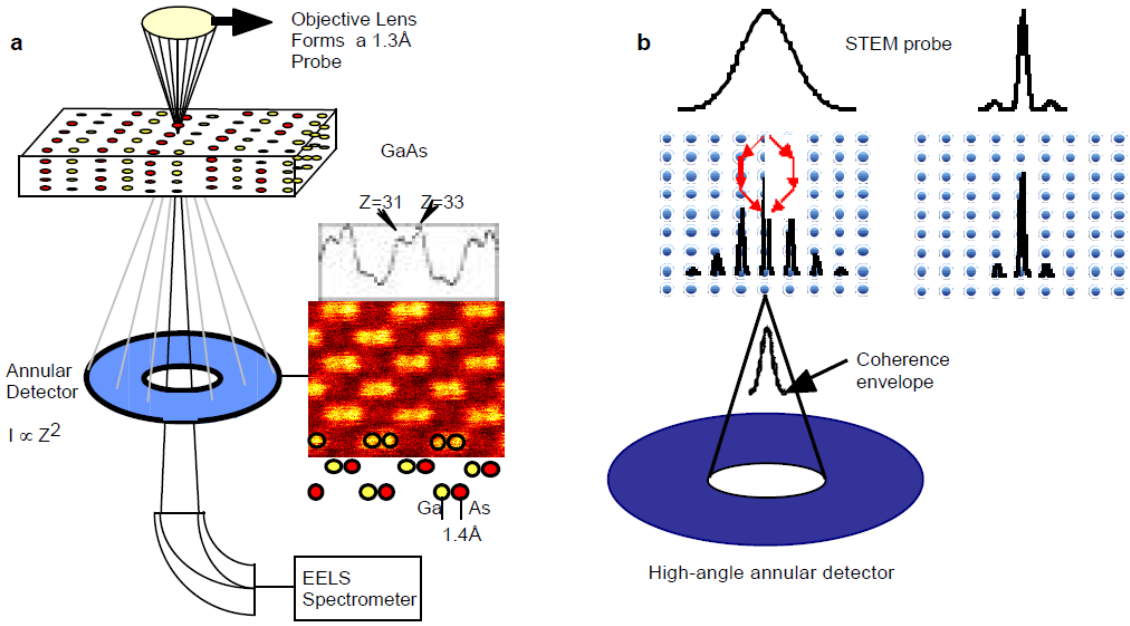


**Figure 1.4** (a) Schematic of STEM showing the formation of a Z-contrast image. (b) Schematic showing the effective propagation of the probes as viewed by the high angle detector.[31] (Figure adapted from Ref. 31)

### *1.3.5 Energy dispersive X-ray spectroscopy*

EDS is a very useful tool for elemental analysis in electron microscopy. Electrons are focused into a very fine beam to hit the sample and may kick off the inner shell electrons of an atom to form an electron hole which will be then filled up by higher energy electrons in an outer shell. The energy difference between the higher energy and lower energy shells may then be released in x-ray form. The x-ray will then be collected by the energy-dispersive spectrometer equipped on the SEM/TEM to generate spectra of intensity versus energy (in keV) which gives elemental composition information.[21]

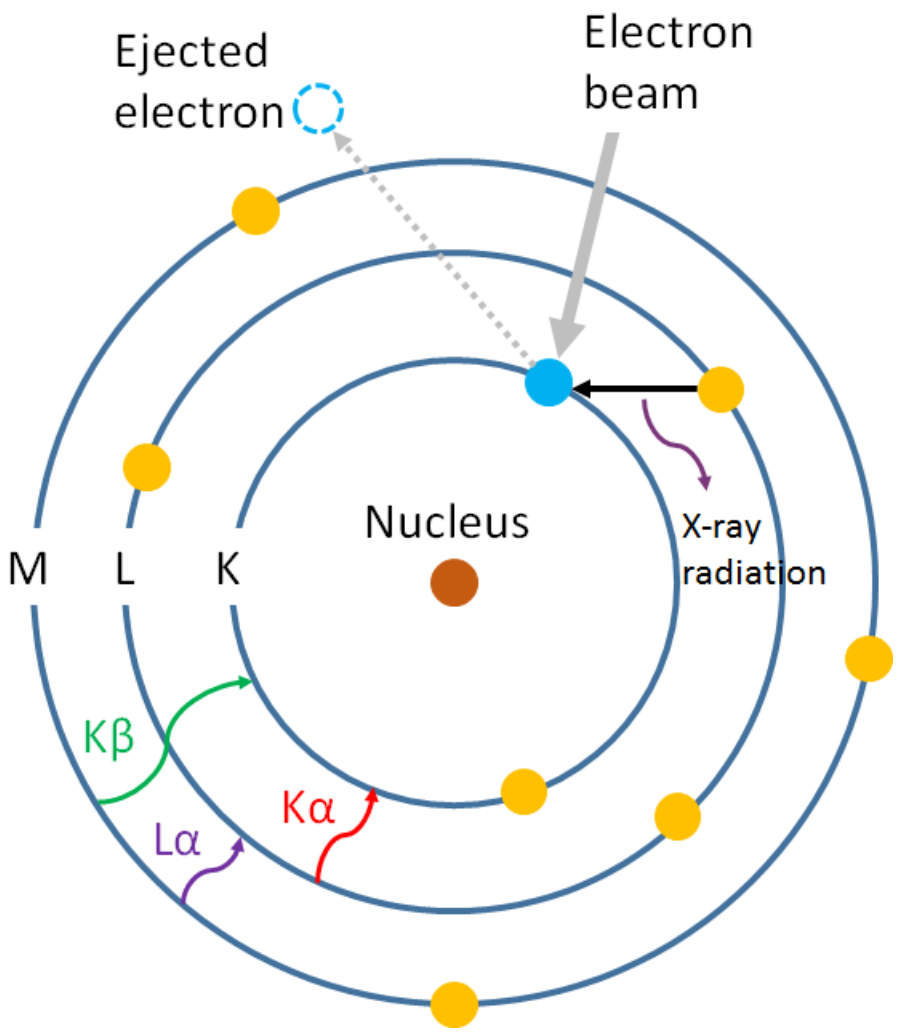


**Figure 1.5** Schematic of high energy electron beam interact with an atom and generate a characteristic X-ray radiation emission.

### *1.3.6 Electron energy loss spectroscopy*

After the electron beam pass through sample specimen, the energy of electrons can be lost in several forms. The energies typically measured by EELS are due to core loss events similar to those detected by EDS, and are useful for elemental compositional analysis. At lower energies, however, one form of energy loss in which we are particularly interested is the excitation of plasmon modes; these can be observed by detecting emitted optical radiation or by measuring the energy loss of the electron. The

emitted optical radiation, known as cathodoluminescence (CL), has been used for resolving higher-order plasmons in small metallic nanostructures. However, CL is limited by the quality of electron beam and signal intensity and can only be used for resolving bright modes while the dark modes can be captured by EELS. It is possible to piece together the full spectrum of plasmonic behavior when both dark and bright modes are detected.[22,23] Previously in our group we have shown STEM-EELS to be a very powerful technique for mapping the spatial distribution of surface plasmon modes of metallic nanoparticles by taking EELS and HAADF simultaneously with both high spatial and energy resolution.[24,25]

An EEL spectrum is composed of three parts:

1. By several orders of magnitude, the most intense peak in the spectrum is the zero-loss peak at 0 eV from those electrons still possessing their original energy. The full width half maximum (FWHM) of this peak is typically taken as a measure of the energy resolution of the microscope.
2. The low-loss region (<100 eV) where the most frequent inelastic interactions occur, including those which generate plasmons. The intensity of bulk plasmon is relatively high.

The core-loss region (>100 eV) where the electrons have the most interactions with inner-shell electrons to provide useful information for elemental analysis.

### *1.3.7 EELS mapping of plamons*

Our samples will be prepared for TEM/STEM characterization on both silicon nitride and carbon substrates by using drop-casting methods. A micro-Raman confocal

microscope equipped with an external spectrometer with a white light source will be used to perform resonant-Rayleigh scattering measurements in order to elucidate optically active (bright) localized surface plasmon resonance (LSPR) modes (as described in section 1.3). The x-y motorized stage on this microscope can be used for mapping the plasmonic structures with a roughly 500 nm spatial resolution. In order to be able to find the same target sample for STEM mapping, a low-resolution optical dark-field image will be taken to be used as a map for subsequent STEM-EELS analysis. After inserting the sample into the STEM, the target peapod nanowire or self-assembled chain will be located by the assistance of the dark field maps made previously. A STEM-EELS technique previously developed by us will be performed to identify the spatial distribution and discrete energies of all of the plasmon modes that appear in the target sample.[17] Using the JEOL 2010F microscope at UK (theoretical spectral resolution of 0.8 eV), it is anticipated that mapping modes of energy of about 1.5eV and greater will be possible, which are suitable for the known energies of Au LSPRs. In order to separate individual plasmonic resonance peaks from the background, Digital Micrograph software will be used to extract the zero loss peak. The Automated eXpert Spectral Image Analysis (AXSIA) program developed by Kotula *et al*. has been used to perform a matrix-rotated principal components analysis in recent literatures.[26-28] In this thesis, we performed the similar analysis using Python with a script written by Dr. Gerd Duscher from University of Tennessee-Knoxville.

Since both optical and electronic methods will be used to characterize the sample, a major advantage is that this will allow us to determine both bright and dark optical modes (dark modes are excited by electron beam in STEM). This is of interest for sub-

diffraction limit wave-guiding without radiative loss. In the long term, correlated measurements such as these should allow for a direct link between synthetic conditions and plasmonic functionality to be established. An example of a previous work done by our group, STEM-EELS mapping of Ag nanorod, is presented in Figure 1.6.

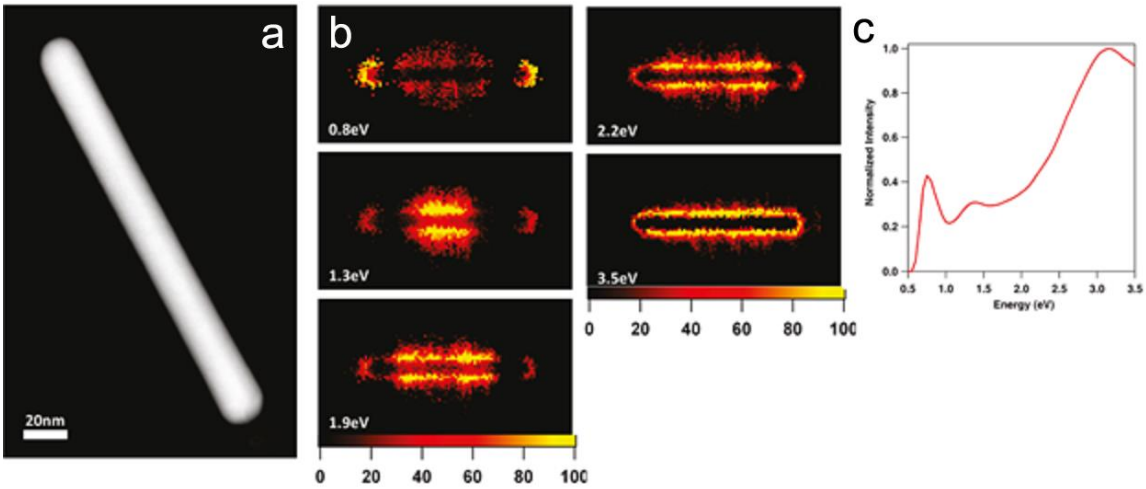


**Figure 1.6** An example of EELS mapping of a single Ag nanorod. (a) ADF image of the Ag nanorod. (b) Multivariate statistical analysis (MVSA) score images. (c) Summed EEL spectrum.[24] (Figure adapted from Ref. 24)

### *1.3.8 Liquid cell in situ S/TEM*

For a long time, only solid phase samples could be inserted into a TEM. The Hummingbird liquid cell holder is a special TEM sample holder with a liquid cell design which makes it possible for solution phase samples can be inserted into the TEM for in situ imaging without breaking the vacuum system. The tip of the liquid cell holder is composed of two pieces of silicon microchip with a small etched viewing window within allowing the electron beam to pass through. The microchips are covered by thin silicon nitride membrane for sealing in the liquid solutions. Further details of this experimental set-up are given below in Chapter two. This experiment was performed on a Hitachi 3300

TEM with a maximum acceleration voltage of 300 kV at Oak Ridge National Lab (ORNL).

## 1.4 Other characterization techniques used in this dissertation

### *1.4.1 X-ray diffraction*

Powder XRD is used for fundamental crystal structure analysis which is based on observing the scattered angle and intensities of an incident x-ray beam. XRD is used to identify the phase purity and crystal structures of the as-grown materials from solid-state materials. XRD patterns are taken on a Bruker D8 Advanced diffractometer using Cu K2-alpha radiation. Normal scans are taken from 10-80 degrees two theta. The XRD patterns were compared with standards from the database or indexed using simulations calculated with CrystalMaker software. The incident X-rays are scattered from atomic planes in crystals and produce peaks that helps us to identify crystal phases and crystal structures of the materials. The diffracted rays satisfy the Bragg's law:[29]

$$n\lambda = 2d \sin \theta$$

Where $\lambda$ is the wavelength of incident X-rays, d is the spacing between planes, and $\theta$ is the angle between atomic planes and scattered rays.

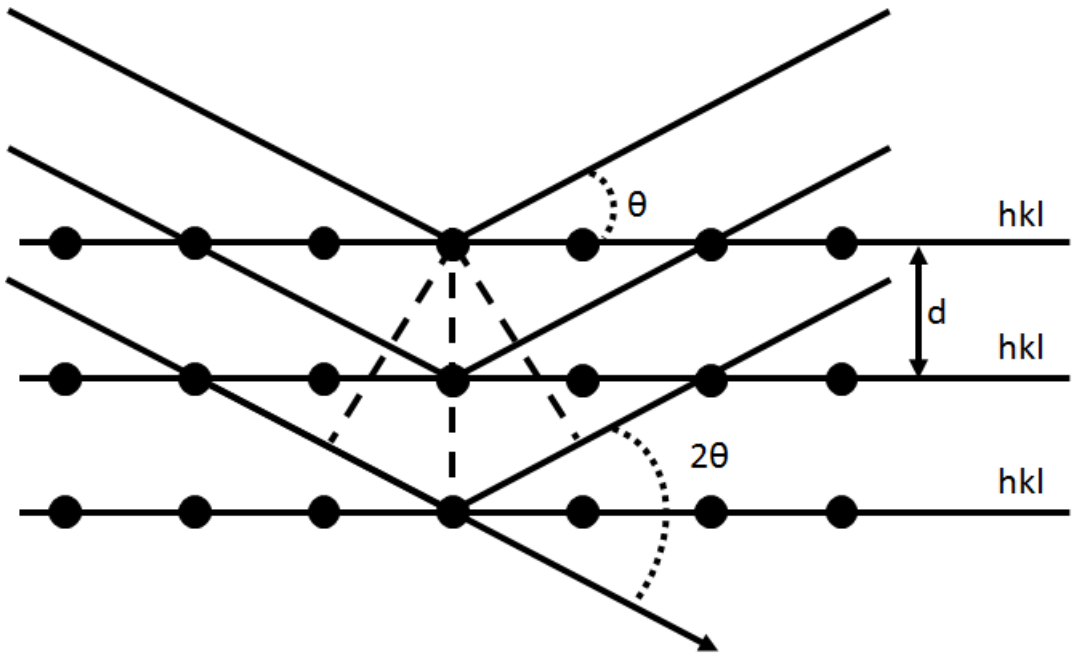


**Figure 1.7** A schematic shows the incident rays, scattered rays and the angle between atomic planes and scatted rays.

## Chapter 2: Experimental methods

### 2.1 Sample Synthesis

#### *2.1.1 Gold nanorods synthesis*

Au nanorods were synthesized by the commonly used seed mediated method published by the Murphy group.[32]

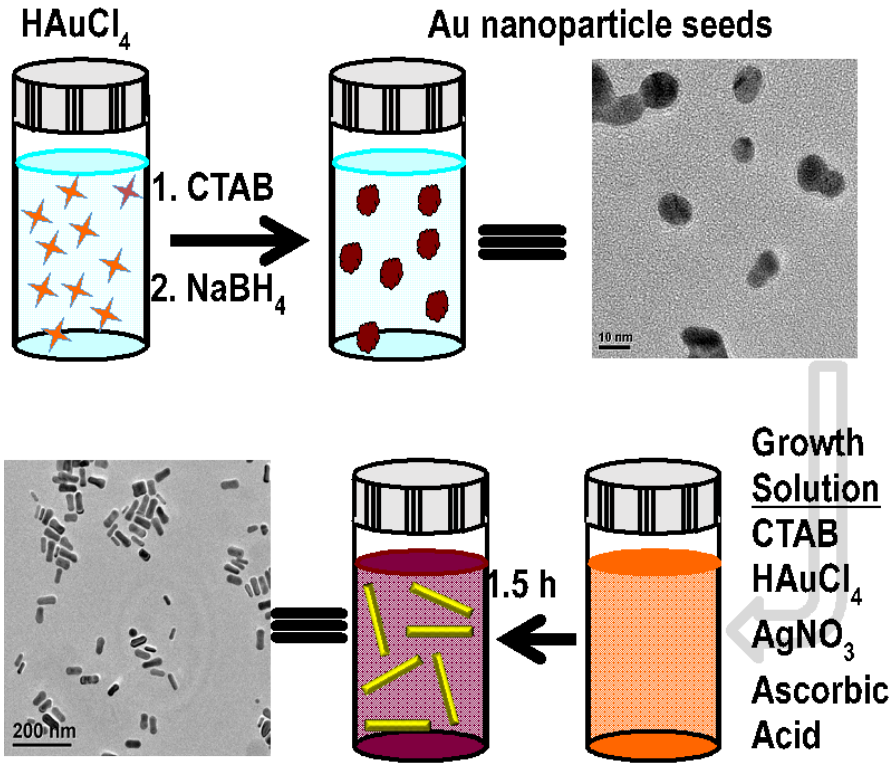


**Figure 2.1** Step-by-step gold nanorods synthesis using seed mediated method.

#### *2.1.2 Pd decorated $Cu_2O$ cubes synthesis*

Parts of this section are taken from "Light-Activated Tandem Catalysis Driven by Multicomponent Nanomaterials" *J. Am. Chem. Soc.* 2014, 136, 32−35.[33]

**Materials:**

3-chlorobiphenyl (PCB2), 3,3´,4,4´-tetrachlorobiphenyl (PCB77), and 2,4,5,6-tetrachloro-*m*-xylene (TCMX) were obtained from AccuStandard (New Haven, CT). $Cu_2SO_4$, sodium citrate, $Na_2CO_3$, glucose, and PVP were purchased from Sigma (St. Louis, MO), while $Pd(O_2CCH_3)_2$ was obtained from Alfa Aeser (Ward Hill, MA). Finally, hexane and ethyl alcohol were purchased from EMD (Gibbstown, NJ). 18.2 MΩ cm deionized water (E-pure water purification system; ThermoScientific, Marietta, OH) was used for all experiments.

**Synthesis of $Cu_2O$ and $Cu_2O$@Pd:**

$Cu_2O$ cubes were prepared using established techniques. Briefly, 2 g of PVP (MW 25 000 g/mol) was added to 100 mL of a 0.035 M $Cu_2SO_4$ solution in a 500 mL round bottom flask. The mixture was then vigorously stirred for 1 h. Subsequently, 50 mL of a 0.07 M sodium citrate and 0.12 M $Na_2CO_3$ solution was added drop wise, resulting in a dark blue color change. Next, 50 mL of a 0.14 M d/l-glucose solution was slowly injected into the reaction solution. The flask was then immersed in a water bath at 80 ºC for 3 h to drive the reduction process. The as-synthesized burnt orange material was filtered through a 200 nm track-etched polycarbonate membrane and dried at 60 °C overnight. Once the $Cu_2O$ cubes were prepared, Pd was deposited on the oxide surface via the galvanic exchange reaction. This reaction was performed by adding 10 mg of $Pd(O_2CCH_3)_2$ into a colloidal suspension of 100 mg of $Cu_2O$ in ethanol. The solution was stirred overnight, after which the $Cu_2O$@Pd was filtered, washed, and dried at 60 °C.

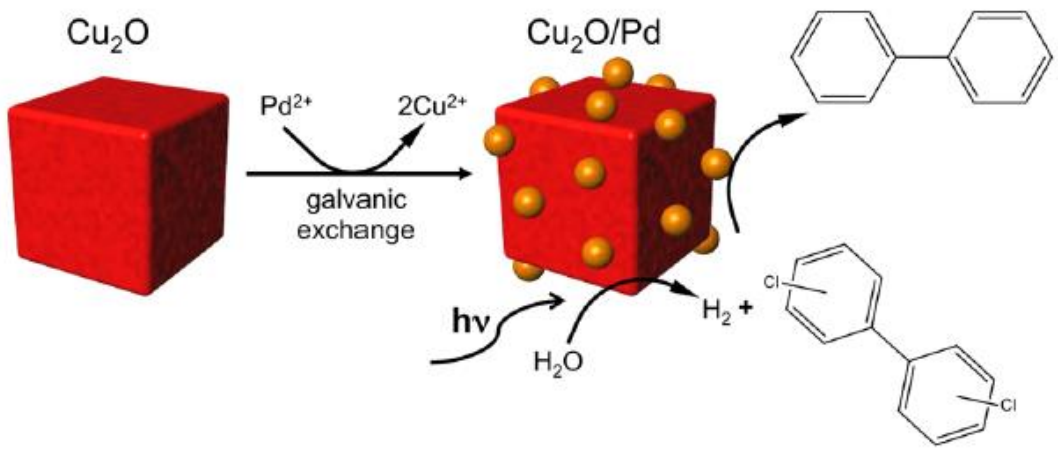


**Figure 2.2** Schematic for the fabrication of Pd decorated $Cu_2O$ nanocubes. (Figure adapted from Ref. 33)

### *2.1.3 Synthesis of $MnSb_2Se_4$ nanorods*[35]

**Materials**:

Antimony(III) acetate [$Sb(OOCCH_3)_3$] (97%) (1-Hexadecyl) trimethylammonium bromide (CTAB, 98%) [$C_{19}H_{42}BrN$] were from Alfa Aesar, and Selenium (powder, 99.999%) were purchased from Alfa Aesar. Manganese(II) acetate [$Mn(OOCCH_3)_2$] and Oleylamine (OLA) (70%) were obtained from Aldrich. All chemical were used as purchased.

**Synthesis of $MnSb_2Se_4$ 1g CTAB:**

0.81 mmol of $Mn(OOCCH_3)_2$, 1.62 mmol of $Sb(OOCCH_3)_3$ and 2.74 mmol of CTAB were dissolved in 20 ml of ethanol at room temperature under vigorous magnetic stirring for 10 minutes. 1.62 mmol of Selenium powder was added to the above solution and a black/silver precipitate appeared after 20 to 30 minutes. The mixture was sealed in a Teflon-lined stainless steel autoclave (45 mL) and placed in a preheated oven at 200 $^{o}$C under solvothermal processing for 12 h. The materials cooled naturally after removed to

room temperature. The resulting silver powder was collected by centrifugation and washed with ethanol and chloroform several times. The product was dried in the furnace under vacuum with 50 cc flowing argon at 200 ºC for 8 h.

**Synthesis of $MnSb_2Se_4$ 0.5 mL Oleylamine:**

A procedure similar to the one described above was employed, in this case without CTAB, and adding 5 mL of Oleylamine and 15mL of ethanol to the solution containing 0.81 mmol of $Mn(OOCCH_3)_2$, 1.62 mmol of $Sb(OOCCH_3)_3$ and 1.62 mmol of Selenium powder when transferring the solution into the Teflon-Lined stainless steel autoclave.

**Synthesis of $MnSb_2Se_4$ 1g CTAB/ 5 mL Oleylamine:** For this sample both CTAB and Oleylamine were used, added as described above.

*2.1.4 Synthesis of Au in Hexaniobate nano-peapod structures*

**Synthesis of Potassium Hexaniobate:**

$K_4Nb_6O_{17}$ was synthesized through a solid-state reaction using ground mixture of $K_2CO_3$ and $Nb_2O_5$ (in the molar ratio of 1.0:1.4). The mixture was treated at high temperature as 900 °C for 1h before continuing to heat at 1050 ºC for another 24 h. In order to compensate the loss of volatile potassium oxide species, a slight excess of $K_2CO_3$ was added. The product obtained after the solid-state reaction was washed twice with water and acetone and finally dried t at 80 °C for 24h.

**Synthesis of $H_xK_{4-x}Nb_6O_{17}$:**

In order to make $H_xK_{4-x}Nb_6O_{17}$, of $K_4Nb_6O_{17}$ powder (0.15 g) were mixed with 3 M HCl solution (15 mL) and stirred at 50 °C for 3 days. The obtained proton-exchange form of

hexaniobate was thoroughly washed using the mixture of *ca.* of milli-Q water and acetone and then dried at 80 °C for 24h.

**Solvothermal synthesis of intercalated multi-walled hexanioabte nanoscrolls:**

In a typical experiment, $H_xK_{4-x}Nb_6O_{17}$ (0.05 g), TBAOH (0.15 g), oleylamine 5 mL), and of toluene (8 mL) were mixed in a 20mL vial and magnetically stirred for half an hour. Final mixture was transferred into a Teflon-lined stainless steel autoclave (Parr, model 4749, 1800 psig, 23 mL) and solvothermally treated at 220 °C for 6 h. The obtained product was washed with ethanol and centrifuged for 5 minutes to remove extra agents.

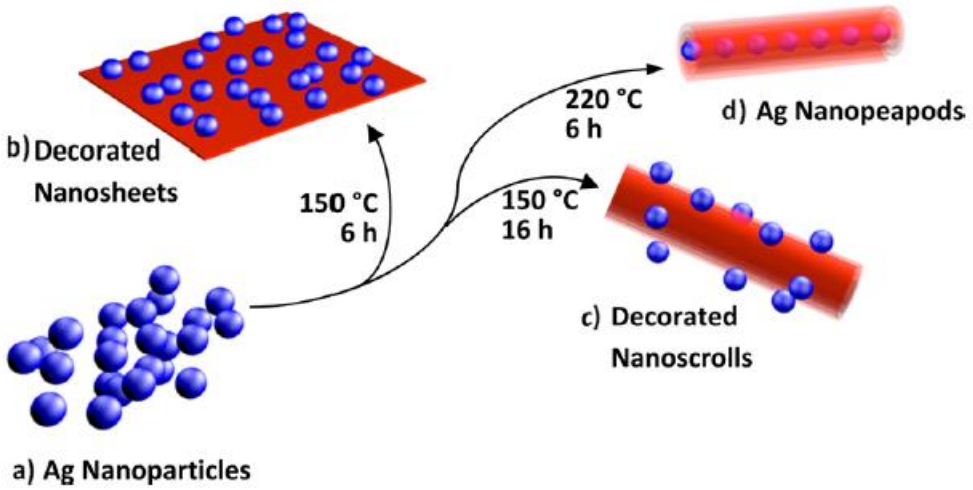


**Figure 2.3** Schematic for the fabrication of metal in hexaniobate nanocomposites via a solvothermal method.[34] (Figure adapted from Ref. 34)

## 2.2 Sample preparation for transmission electron microscopy

Most TEM samples are made by using the most common drop casting method. However, the procedures are slightly different in different projects. The detail TEM sample preparations are discussed in separation sections.

### *2.2.1 Liquid cell in situ observation preparation*

497μ$L$ Au nanorod solution was mixed with 3μ$L$ of cysteine solution in a vial. About 0.3μ$L$ of mixed solution was dropped onto a silicon microchips, and a second microchip was placed upside down on top of the first microchip to sandwich and seal the mixed solution. The Hummingbird liquid cell holder was then inserted into the Hitachi HF3300 TEM. The maximum accelerating voltage was 300 kV and videos were taken in STEM mode. Figure 2.4 shows a schematic illustration of our in situ liquid STEM set-up which utilizes silicon microchips and $Si_3N_4$ membranes as a platform for sealing liquid solutions and imaging the dynamics of nanoparticle self-assembly in liquid environments.

### *2.2.2 EM Characterization for Pd decorated $Cu_2O$ cubes*

Scanning electron microscopy (SEM) and transmission electron microscopy (TEM) were used to study the morphology of the Cu2O and Cu2O/Pd materials using a Philips XL30 field-emission environmental SEM equipped with an Oxford energy-dispersive X-ray detector and a JEOL JEM-1400 TEM, respectively. SEM experiments were performed at 20 kV, while TEM experiments were conducted at 80 kV. Annular dark-field Scanning TEM (ADF-STEM) experimentation was performed on a JEOL 2010F TEM/STEM at 200kV, equipped with Oxford EDS detector. Using this system, EDS mapping was performed and quantified employing Gatan Digital Micrograph software, which integrated the area of the Cu Kα peak and Pd Lα peak to form the compositional map.

### *2.2.3 $MnSb_2Se_4$ nanorods characterizations*

All samples were characterized by powder X-ray diffraction collected on a Bruker D8 Advanced diffractometer with $CuK_\alpha$ radiation (λ = 1.54056 Å). The morphology of the

nanostructures was observed by scanning electron microscope (SEM, S-4800). The high-resolution images, as well as the composition from the energy dispersive X-ray spectroscopy (EDS), were collected using a JOEL 2010F (200 kV) transmission electron microscope.

### *2.2.4 TEM sample preparation for gold in Hexaniobate nano-peapod*

Preformed hexaniobate nanoscrolls (NScs) were used as a template for the in-situ growth of gold nanoparticle within the hollow space of hexaniobate NScs. First, Hexaniobate NScs (10mg) were mixed with $HAuCl_4 .3H_2O$ (20 mg), toluene (3 mL), OAc (160 µL) and OAm (160 µL) and magnetically stirred. Then, the solution was heated to 60 °C and held at this temperature for 2h. The resulting product was washed with toluene and separated via centrifugation. The obtained sample was redispersed in toluene and further centrifugation was applied to remove/reduce free Au NPs. Finally, the separated Au@hexaniobate NPPs were dispersed in toluene and drop-casted on a TEM grid for TEM analysis.

## 2.3 Liquid cell in situ transmission electron microscopy

With the recently developed *in-situ* liquid cell TEM/STEM technique, a small amount of solution is allowed to insert into the TEM without breaking/contaminating the vacuum system. Nanoscale images/video are generated simultaneously as the reaction goes on. In this project, we investigate the solution mixed by cysteine and Au nanorod solutions with various pH environment, using a Hummingbird liquid cell holder equipped with a Hitachi HF3300 high resolution STEM. The liquid cell consists two pieces of silicon microchips with $Si_3N_4$ membranes for sealing solution. Gold nanorods have been extensively studied because of its interesting plasmonic characteristics which leads to a wide range of

applications. The surface passivant plays an important role of both stabilizing the Au nanorods, and its exposure to solution. The optical properties can be directly controlled by changing the shape, size and aspect ratio of the Au nanorods. At pH=2, two videos successfully captured the assembly process in real time. Both rotational and translational movements leading to Au nanoparticle chains formation are observed. By using the liquid cell STEM to study the dynamics of Au nanorod chain assembly, we hope to elucidate the key factors of controlling desired shape Au nanoparticle chains and their plasmonic behaviors. The self-assembly process is quite interesting and many theories have been proposed since nobody has visualized what really happened in the solution in nanoscale. More details of this project will be presented in chapter 3.

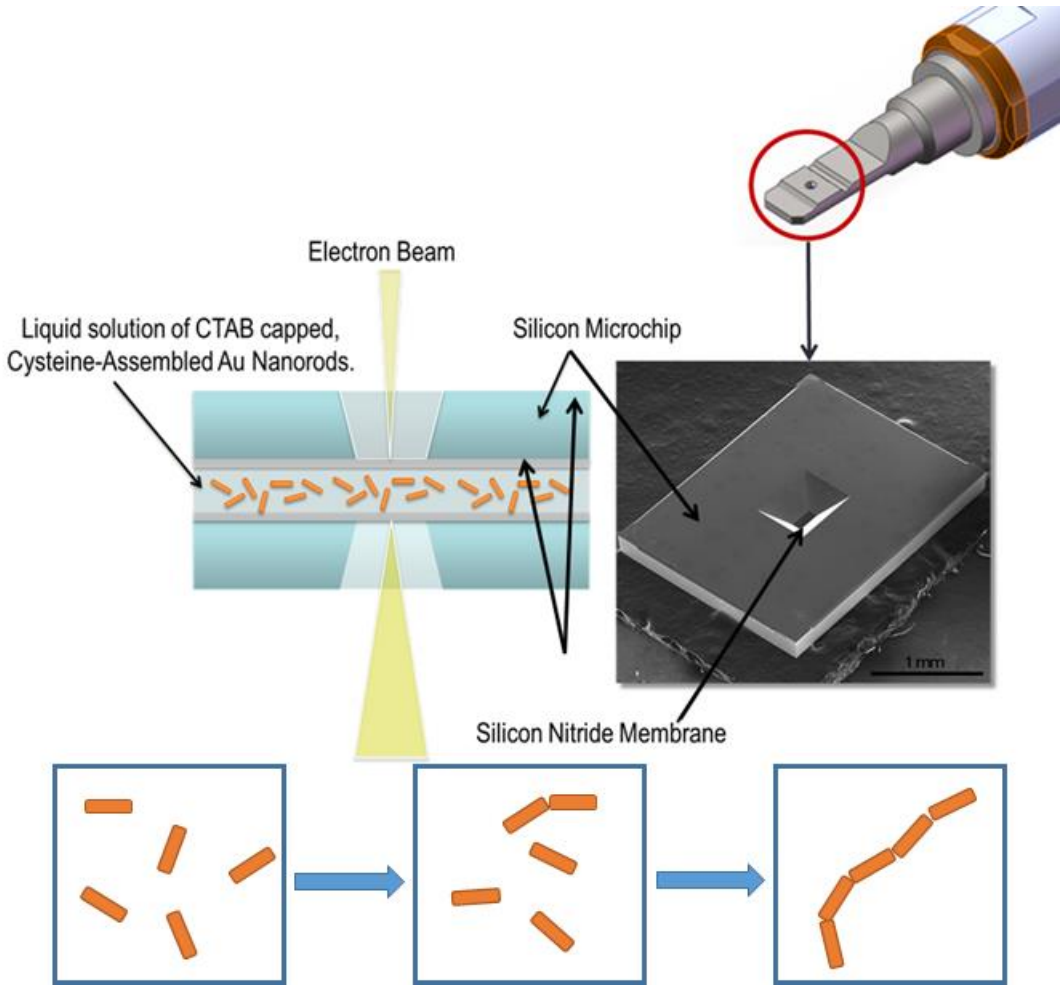


**Figure 2.4** Schematic for Liquid cell in situ experiment for gold nanorods self-assembly.

## Chapter 3: *In situ* liquid cell observation of localized surface plasmon resonance assisted gold nanorods assembly

### 3.1 Introduction

Liquid cell *in-situ* TEM/STEM has been an emerging field in the past few years, and has been reported as a very powerful tool for real-time imaging on the nanometer length scale for solution phase reactions. With a liquid cell holder, a little amount of liquid is allowed to be securely sealed and inserted into the TEM without breaking the vacuum system. The development of liquid cell has been directly beneficial to many areas of nanoscience because of its ability to directly visualize the dynamics of nanocrystals in liquids. So far, liquid cell in-situ TEM/STEM has been used for observing lithiation/delithiation of electrode materials in liquid battery systems,[36,37] *in situ* observation of fluid cells,[38,39] and for *in situ* electrochemical measurements in liquid battery systems.[40-43] The same techniques have also been widely used in visualizing nanostructure nucleation, growth and synthesis in order to elucidate the mechanisms of growth.[44-51]

Reports of *in situ* observation of nanostructure self-assembly are also rising rapidly.[52,53] Alivisatos et al. used a homemade graphene-based liquid cell to observe nanocrystal growth directly,[54] and to monitor structural changes and nanocrystal motion in 3-D.[55,56] One interesting experiment also reported by Alivisatos et al. was to observe the self-assembly of gold nanorods with no post synthesis modification, in a liquid cell holder.[57] The high ionic strength of solution and the anisotropic electrostatic repulsion were determined to be the driving forces for tip-to-tip alignment of the Au nanorod into chains. Following this report, Marquez et al. demonstrated that tip-to-tip assembly of

gold nanorods may be induced by exciting the localized surface plasmon resonance (LSPR) modes of the nanorods in polymer films.[58] In this report, the authors used a laser to selectively activate the longitudinal LSPR mode of the Au nanorods which eventually led to tip-to-tip alignments, opening up a new route to control Au nanorods self-assembly. Taken together these reports imply that the excitation of LSPR modes – a known driving force for self-assembly – may be mediated by high ionic strength in solution, and this is confirmed by Baral et al. who found that diluting an ionic solution attenuates the plasmon absorbance.[59] In combination these reports suggest that the observation by Alivisatos et al. could in fact have been LSPR-induced self-assembly, in which the high ionic strength they used helped to mediate the electron-beam activation of the LSPR modes.

In this thesis, we present results in support of this hypothesis, showing that Au nanorod self-assembly observed *in situ* within a liquid cell occurs via three stages: (i) a diffusive regime, in which nanorods initially diffuse to within each other's vicinity, with smaller rods moving more quickly due to reduced viscous drag; (ii) an approach period in which activation of the LSPR modes leads to faster approach speeds for larger particles/clusters, and relative orientation rather than proximity of the rods dictates which rods form attachments; and (iii) an attachment period during which irreversible attachment occurs. In this work we use cysteine-functionalized Au nanorods for which cysteine has been reported in *ex situ* measurements to functionalize the tip of the nanorod, leading to tip-to-tip self-assembly. In our investigations the cysteine does not appear to be the driving force for the initial approach, although it could be mediating the strong resulting attachment.

## 3.2 Materials and methods

Environmental fluid cell microscopy is a rapidly emerging field, very much in its infancy, due to the inherent, complex issues associated with containing and imaging through thin fluid layers within the high vacuum of a TEM column. This core challenge has recently been overcome through the sealing the fluid between two electron-transparent viewing membranes to prevent evaporation of high vapor pressure liquids (and consequent contamination of the microscope column). Typically, this is accomplished through the use of silicon microchip devices containing a thin electron transparent silicon nitride (SiNx) viewing membrane. To image the dynamics of the nanoparticle self-assembly process in the current work, a thin layer of the liquid solution containing a mixture of CTAB capped Au nanorods with cysteine was placed between two 50 nm electron transparent SiNx membranes (Fig. 3.1). A liquid flow cell TEM holder was used to support the silicon microchip frames. Prior to loading the solution, the microchips were cleaned in an acetone then methanol rinse, followed by plasma cleaning, which rendered the surface of the SiNx membranes clean and ready for liquid sample loading.

The in situ liquid STEM experiments were performed with a Hitachi HF3300 S/TEM instrument that is equipped with a cold-field emission gun that was operated in STEM mode at a 300kV accelerating voltage and 15nA probe current. A high angle annular dark field (HAADF) STEM detector was used to image the dynamics of nanorod assembly processes at high spatial resolution.

Au nanorods were synthesized by the commonly used seed mediated method published by the Murphy group.[62]

The surface of Au NRs are covered by CTAB, a surfactant to stabilize the Au and maintain its nanorod shape. Due to the curvature of the nanorod tips, the CTAB molecules are more widely spaced and result in greater surface area to which cysteine may bind. The following pHs of the mixed solutions were investigated: 1.0, 1.25, 1.5, 1.75 and 2.0, varying pH via the concentration of HCl in the synthesis solution.

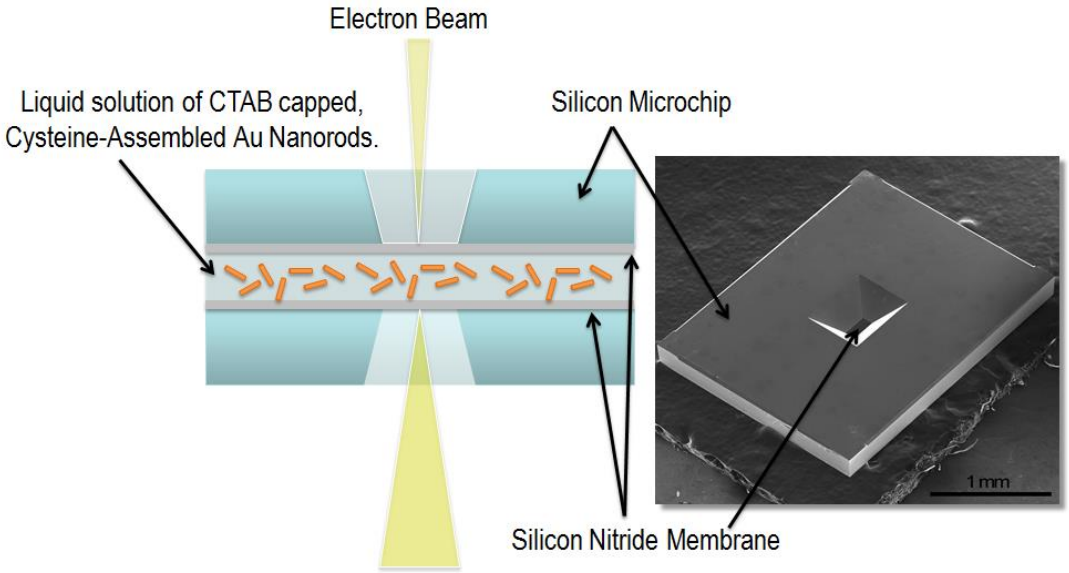


**Figure 3.1** Schematic illustration of the *in-situ* liquid cell used for these experiments.

## 3.3 Results and discussions

### *3.3.1 Ex situ results*

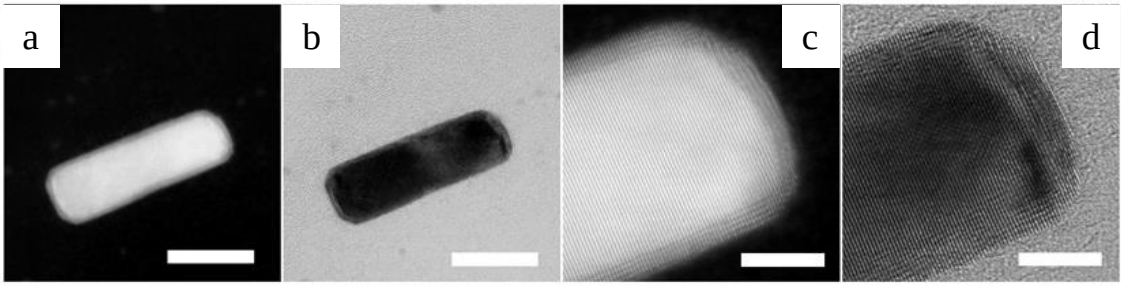


**Figure 3.2** High resolution Z-contrast (a, c) and bright field (b, d) images of a single Au nanorod. Scale bar, left to right= 20, 20, 5, 5 nm.

Figure 3.2 shows high-resolution Z-contrast and bright-field images, revealing the core-shell structure as Wright et al. reported,[60] where the surface of Au nanorods are capped with a few atomic layers of Ag originating from the $AgNO_3$ reactant. Ag caps the rod completely, with no preference for any particular region on the rod.

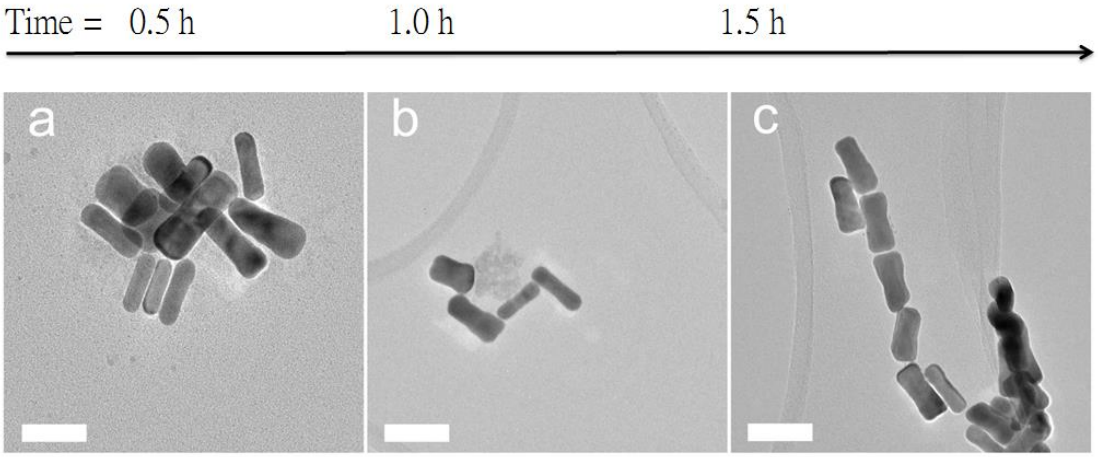


**Figure 3.3** Ex situ TEM images showing that the Au nanorods will self-assemble into nanoparticle chains over a period of ~60-90 mins at pH=2.0, without external stimulus. (Scale bar= 20nm)

Prior to running the *in situ* experiment, *ex situ* TEM (Fig. 3.3) was performed on samples allowed to assemble for increasing periods of time, for two purposes. First, to optimize the experimental conditions; and second, as a control to verify that nanoparticle chain assembly occurs without the presence of the electron beam. At the early stage (0.5 hour) of mixing, Au nanorods were distributed with every orientation. One hour after mixing, some short nanoparticle chains were observed as Au nanorods started to line up tip-to-tip. One and a half hours after mixing, many longer Au nanoparticle chains were observed. For these *ex situ* measurements, the cysteine's thiol, amine, and carboxyl groups provide the driving force for self-assembly. Once cysteine is added into the Au nanorod solution, the thiol groups selectively bind to the tip of the nanorods, since the density of the CTAB is lowest at this point of high curvature. The uncoordinated zwitterionic headgroups can electronically interact with other species in solution, and electrostatic interactions of the cationic amine and anionic carboxylate between multiple amino acids on the surfaces of adjacent Au nanoparticles can be used to attract the species closer together to begin the assembly process. Once particles are close enough for attachment, amine crosslinking occurs, where the amine on the head group binds to the surface of another particle to form an irreversible bond. In this scenario, the affinity of the amine group to the gold surface causes the amine to "snap" onto the other particle, once the electrostatics have drawn the particles close enough together for bonding to occur. The rate of this reaction may be mediated by the pH of the solution, which dictates the strength of the electrostatic interactions and can therefore be exploited to control the rate of assembly.

### *3.3.2 In situ results and discussions*

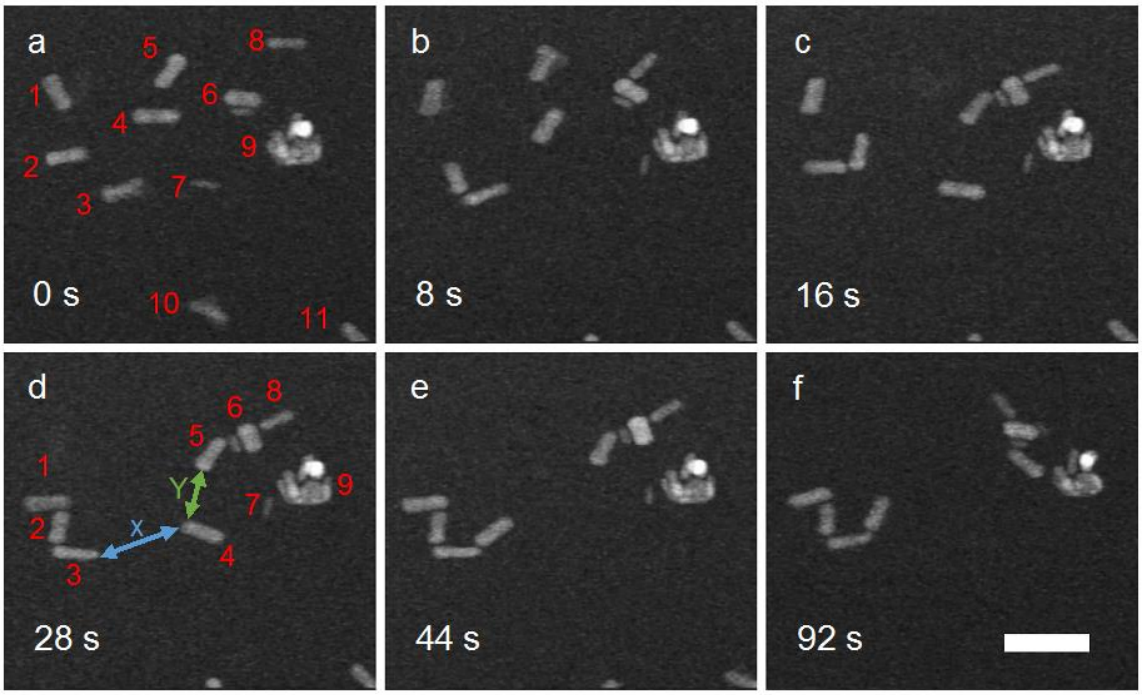


**Figure 3.4** Frames from a movie collected during self-assembly of Au nanorods in a pH2 solution, showing the diffusive, approach, and attachment stages. In (d), X= 105.10 nm and Y= 64.57 nm. Attachment completes by ~ 92 seconds. scale bar = 100 nm.

The self-assembly process was investigated using an *in situ* liquid cell setup. It is immediately apparent that the rate of assembly is much greater in the *in situ* experiment with respect to the data collected *ex situ*, occurring on the seconds to minutes timescale, as oppose to hours outside of the TEM. This suggests that electron beam plays a major role in either the diffusion and/or the approach regimes of assembly. The early stage diffusive motion of the Au nanorods appears to be activated by electron beam irradiation, and differs from Brownian motion. One important observation regarding the approach regime is that the specific particles which approach and assemble are not always those which are closest to one another, suggesting that proximity alone cannot govern the approach period of assembly. This is illustrated in Fig. 3.4(d), when particle 4 chooses to

join the cluster of particles labeled 1/2/3, rather than the closer grouping of particles 5/6/8. This suggests that neither electrostatic attraction nor hydrogen bonding is responsible for the approach of the nanorods in contrast to the ex situ case.

In order to investigate these stages we calculated the speed of each rod or cluster of rods at two points during the assembly process: once at the beginning of the assembly process (over a time period of 0.16 s between the first two frames), and a second time immediately before the rod attached to a cluster (over a time period of 0.16 s between the penultimate and final frames before attachment). In order to correlate these speeds to the mass of the particles we approximated the rods to be cylindrical, measuring length and diameter of each rod from the images, and used the density of bulk gold to calculate mass. The distance traveled for each Au nanorod was measured by the MTrackJ plugin of ImageJ. For the diffusive regime, the speed of each rod showed a strong inverse linear dependence on its mass (Fig. 3.5(a)). This observation is consistent with a picture in which the rods move due to thermal energy, and larger rods have greater viscosity.

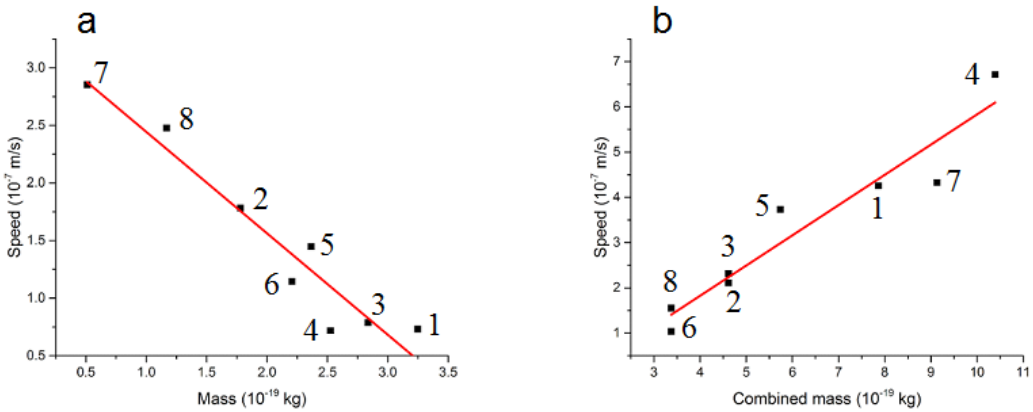


**Figure 3.5** (a) Speed vs mass for each Au nanorod or cluster of nanorods during first two recorded frames, and (b) two recorded frames immediately prior to attachment. Lines of best fit included to demonstrate linearity, with $R^2$ values of (a) 0.9251, and (b) 0.9182.

For the approach stage (Fig. (3.5b)), this trend changes to a direct proportionality between the speed of approach, and the *combined mass* of the nanorod and the group to which it is attaching. In other words, the larger the combined mass of the nanorod chain and its attaching nanorod, the faster the approach speed between these two entities. The speed of each nanorod in Fig. 3.5b is measured within the 0.16 second time frame immediately preceding attachment to a chain. Particles 6 and 8, 2 and 3, and 7 and 9 joined to create a two nanorod chain. Particles 1 and 5 joined the groups of (2+3) and (6+8) respectively, and finally particle 4 joined the group of (1+2+3) and has the greatest combined mass among all combined groups. Based on the mass and the speed of every Au nanorod, the kinetic energies were calculated, revealing an average kinetic energy prior to attachment that is about eight times greater than the kinetic energy measured during the early stage movements. This result implies two conclusions: (i) that a long range attraction exists to attract Au nanorods, and position them at the correct angle and alignment for tip-to-tip attachment, and (ii) this attractive force depends on mass (volume) rather than simply nanorod separation, since the heavier the combined mass or larger total volume, the faster the attaching speed.

In order to further investigate the driving force leading to tip-to-tip alignments, and to reduce the complexity of the problem, we selected an area with just three nanorods and performed the same experiment. Frames from the resulting video are presented in Fig. 3.6. To start, the Au nanorods are not oriented with respect to one another. After a series of rotational movements, at the 100 s mark (Fig. 3.6(e)) all of the nanorods suddenly and simultaneously align parallel. One explanation for this interesting behavior is that when the scanning electron probe approach one of the Au nanorods, the longitudinal LSPR

modes on this rod are excited which may cause the conduction electrons oscillate locally along longitudinal direction within a very short period of time. Within this short period of time, free electrons on nearby rods are induced by the activated LSPR and result in induced coupling which drives nearby Au nanorods to align parallel to one another, placing them in a tip-to-tip position. This can be understood since the electron beam would be expected to excite all possible LSPR modes, and that the collective excitement of LSPRs on closely spaced nanorods might lead to a coupling of these modes.

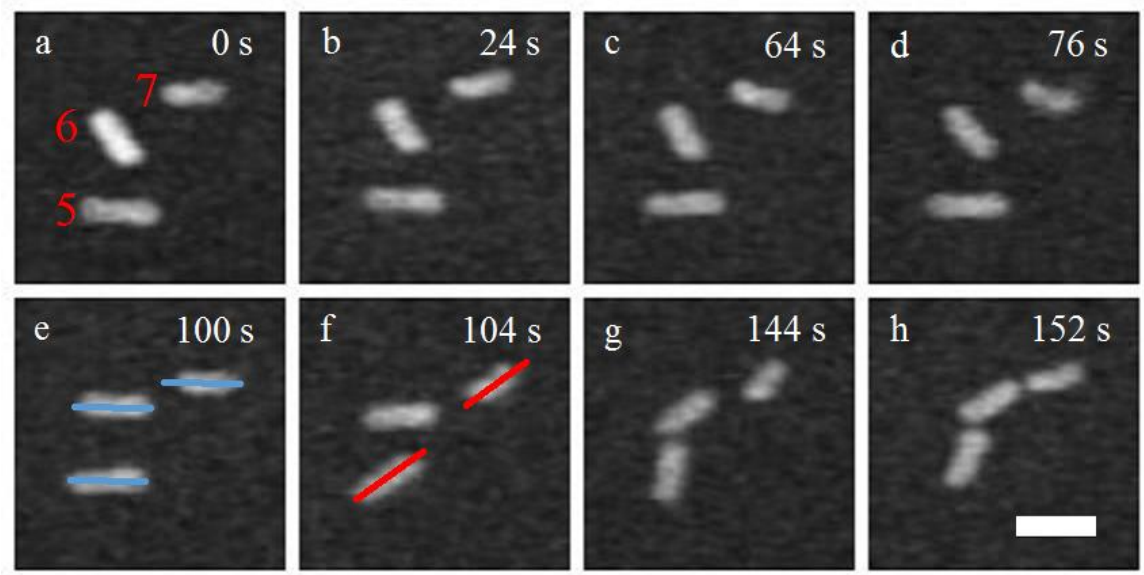


**Figure 3.6** Frames from a movie collected during self-assembly of Au nanorods in a pH2 solution, showing the approach, and attachment regimes. Alignment occurs at 25 s, and attachment completes by ~ 152 seconds. scale bar = 100 nm.

Taking our observations collectively, there are three different stages in the self-assembly process. The first stage is a diffusive regime in which Au nanorods diffuse in the solution, without feeling the presence of one another by long range attractive forces. In the second stage, the electron beam activates the longitudinal LSPR modes, causing the nanorods to couple once they are within proximity of one another, with a coupling

strength that is dependent on the combined mass (volume) of the nanorods, via the Clausius-Mossotti relation:

$$\alpha = 3V[\frac{\varepsilon_r - 1}{\varepsilon_r + 2}]$$

Where $\varepsilon_r$ is the relative permittivity of a material, V is the volume, and α is the polarizability.[61] The LSPR activated by electron probe on one Au nanorod induces nearby free electrons to join the oscillation in the same direction which directly increase the polarizability. According to the equation, polarizability is directly proportional to the volume. The coupling resulting in tip-to-tip alignment of the rods in this second stage. In the final stage, the aligned rods attach, tip-to-tip, via a strong and irreversible interaction, presumably the same cysteine bonding observed in the *ex situ* measurements. Over time, the metal atoms at the tip of the rods are seen to migrate, resulting in an eventual fusion of the rods (Fig. 3.7). This phenomenon could be caused by electron beam irradiation.

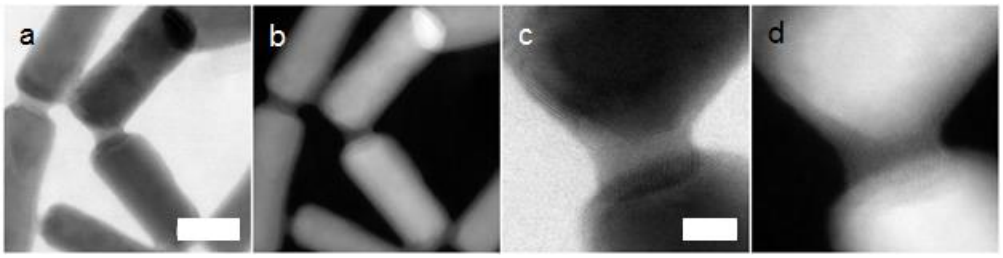


**Figure 3.7** HRTEM of dried assembled sample, showing nanorod tips fused together. (a) and (c) bright-field images; (b) and (d) dark field images. Scale bars are (a, b) 20 nm and (c, d) 5 nm.

### 3.4 Conclusions

Au nanorod self-assembly was successfully observed in real-time, using a liquid cell holder in the STEM. Our results suggest that the assembly of nanorods as observed *in situ* in the electron microscope is likely driven by electron beam excitation of the LSPR

modes, and a coupling of these modes on adjacent nanorods. This is consistent with previous observations that assembly can be induced by laser excitation of the nanorods longitudinal LSPR, and that high ionic strength can mediate the excitation of LSPR modes in solution. The primary supporting evidence for our suggested three-stage model is that assembly occurs much more rapidly in the electron microscope than when performed externally to the microscope, and that assembly speed depends on combined mass (and correspondingly more intense plasmon resonance), rather than inter-rod separation.

## Chapter 4: Pd decorated $Cu_2O$ nanocubes studied by electron microscopy

Parts of this chapter are taken from "Light-Activated Tandem Catalysis Driven by Multicomponent Nanomaterials" *J. Am. Chem. Soc.* 2014, 136, 32−35. The aim of this work was to use electron microscopy techniques to (i) confirm the core-shell structure of the nanocubes; and (ii) perform EDS mapping technique for compositional analysis and map Pd and Cu spatially. Without such characterization, the morphology, size and structure of as-synthesized nanocubes cannot be studied. More importantly, the EDS map is the crucial evidence to show multicomponent nanostructures and explain their high catalytic reactivity.

### 4.1 Introduction

Catalytic technologies must be redesigned for optimal reactivity under sustainable conditions with minimal to no energy input. While organometallic-based systems are traditionally used,[63,64] nanotechnology provides new avenues to achieve such sustainability goals without compromising on the reactivity.[65,66] Furthermore, nanomaterial syntheses have recently matured to allow for the production of highly refined particles that control the size, shape, and morphology of the structure;[67,68] however, the ability to design multicomponent nanosystems remains challenging. Such systems are likely to be highly important, especially for tandem catalytic reactions that require multiple catalysts interfaced into a single system.

Nano- and micro-scale metal oxides have been the focus of research due to their photo-induced electrical properties. This phenomenon can be exploited for important photocatalytic reactions that drive redox- based chemical processes,[69,70] which arise from

the semiconductor band gap; upon irradiation of the material with photons of appropriate energy, electron excitation from the valence to conduction band occurs, where the holes remain in the valence band. These electrons and holes then travel to the oxide surface to drive reduction and oxidation reactions, respectively.[71] Given suitable band positions, this process can split water into $H_2$ and $O_2$.[72,73] As such, photocatalytic $H_2$ production is of enormous value given the potential to generate significant energy sources using available resources and sunlight. Moreover, this sustainably produced $H_2$ could find other important uses in catalytic reactions such as hydrogenation and hydrodehalogenation, given the scale these reactions are performed. Decorating the metal oxide with noble metal nanocatalysts could result in a tandem catalytic system for reactions that are not traditionally driven by light. As such, this approach could transition unsustainable catalytic processes towards more sustainable, light-driven methods.

Here we describe the production of multicomponent tandem nanocatalysts that exploit light for multistep reactivity. In this regard, $Cu_2O$ cubes are generated, where addition of $Pd^{2+}$ salts results in oxide surface decoration with $Pd^0$ nanoparticles via galvanic exchange. Once characterized, the materials were used for the hydrodehalogenation of polychlorinated biphenyls (PCBs), where quantitative reactivity to produce biphenyl was observed using just an aqueous solution and light. For this tandem catalytic system, the $Cu_2O$ participates in $H_2$ production via photocatalysis that is subsequently activated on the Pd surface to drive hydrodehalogenation. These results are important for two key reasons. First, they demonstrate a simple and aqueous-based method for the production of multicomponent tandem catalysts. Such catalytic systems can require surface immobilization to generate the appropriate structures,[74] thus increasing their synthetic

complexity. Second, the materials are reactive using light as an energy source for reactions typically driven by an external $H_2$ source. As such, the adaptation of critically important sustainable approaches towards energy and/or material intensive processes is demonstrated. The Pd decorated $Cu_2O$ nano-cubes are carefully studied by SEM and TEM to study their morphology. Most importantly, Pd and Cu are mapped using EDS technique in the TEM. More details are presented in the next section.

### 4.2 SEM and conventional TEM characterizations

Further characterization of the $Cu_2O$@Pd materials was conducted using both scanning and transmission electron microscopy (SEM and TEM, respectively). Figure 4.1a presents the morphology of the $Cu_2O$ materials prior to Pd addition. From this, well-defined cubic structures were generated with an edge length of 700 ± 120 nm. Note that a small fraction of the $Cu_2O$ structures were truncated cubes. SEM analysis of the materials after Pd deposition is presented in Figure 4.1b. For these structures, the incorporation of Pd nanoparticles did not significantly alter the size of the materials (690 ± 110 nm). As anticipated, the Pd nanoparticles on the faces of the oxide cubes could not be observed using SEM, likely due to their small size. Energy dispersive spectroscopy (EDS) analysis (Figure 4.2) confirmed the Pd content of 3.0 wt%, consistent with the synthetic conditions. Finally, TEM imaging of the $Cu_2O$@Pd materials was also conducted in both dark and bright fields. Figure 4.1c presents the dark field TEM image, displaying showing the cubic morphology of the structures, while, while Figure 4.1d displays a higher resolution bright field image of the edge of the $Cu_2O$ cubes demonstrating Pd nanoparticle incorporation. Here, Pd nanoparticles are evident along the edge of the structure.

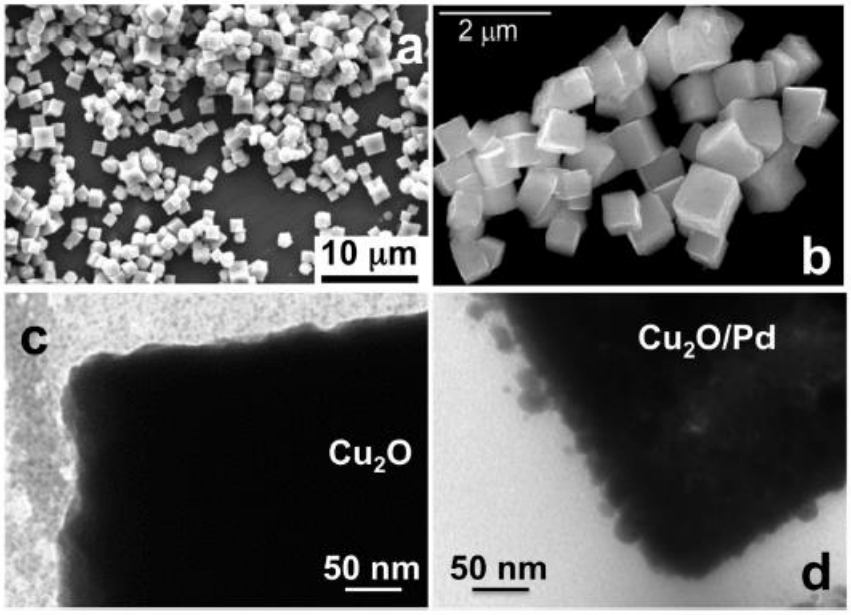


**Figure 4.1** EM characterization: (a,b) SEM images and (c,d) TEM images of the $Cu_2O$ cubes before (a,c) after (b,d) Pd deposition.

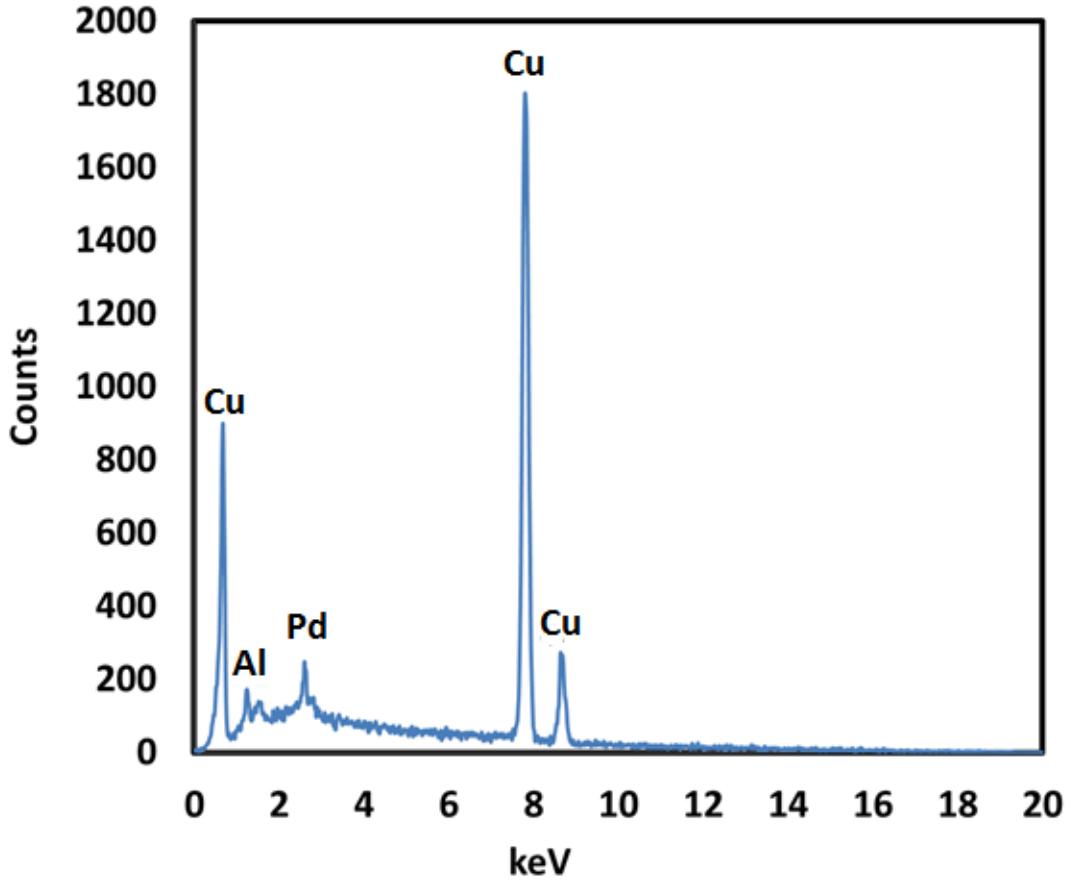


**Figure 4.2** EDS analysis of the $Cu_2O$@Pd materials.

### 4.3 EDS mapping on a single nanocube

Due to the thickness of the $Cu_2O$, complete TEM imaging of the composite structure was not possible, especially along the cube faces. To confirm the $Cu_2O$@Pd morphology, EDS mapping of the materials was conducted using high-angle annular dark-field scanning TEM (HAADF-STEM) equipped with an EDS detector. Cu was detected at 2.84keV and Pd at 8.04keV. Figure 4.3 presents the elemental map and overlay for the composite structures. The images confirmed that the Pd component is deposited along the surface of the $Cu_2O$ cubes, forming the $Cu_2O$@Pd core@shell structure. This design is likely to maximize the

catalytically reactive surface area due to the morphology at the interface between the two components.

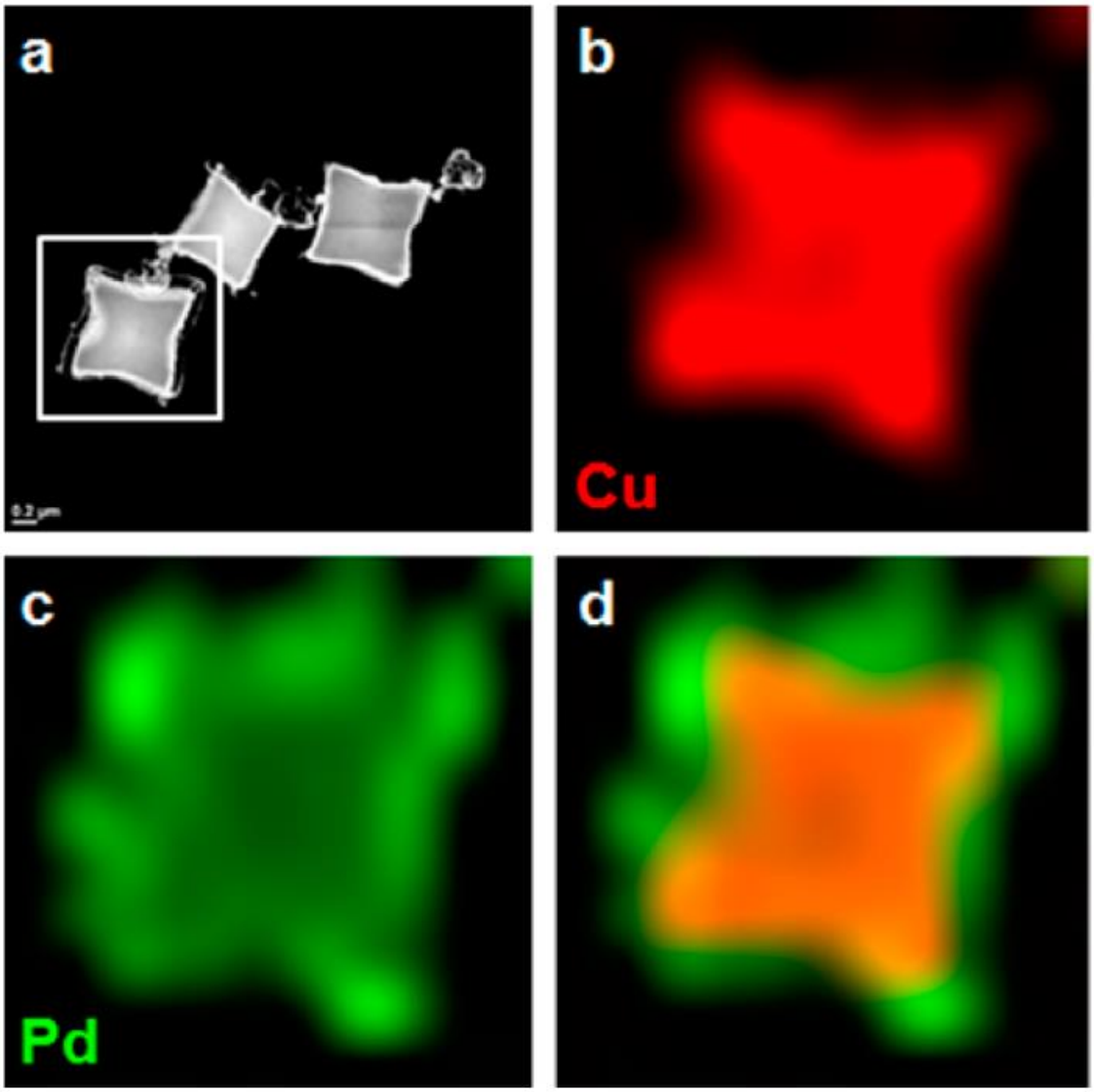


**Figure 4.3** Compositional EDS mapping of the $Cu_2O$@Pd structures using STEM. Part (a) presents the dark field image of the materials, while parts (b and c) show the Cu and Pd maps, respectively. Part (d) displays the composite overlay of the Pd and Cu maps, demonstrating the core@shell structure.

### 4.4 Conclusions

In summary, we have demonstrated the generation of a unique, multicomponent nanocatalyst based upon $Cu_2O$@Pd core@shell materials. These structures were fabricated using a facile electroless method, where the Pd nanoparticles form a uniformly

distributed layer on the surface of the $Cu_2O$ cubes. This architecture provides advantages for light-activated tandem catalytic reactions that are dependent upon $H_2$ as a reagent. The $Cu_2O$@Pd materials demonstrated significant tandem catalytic functionality for the dechlorination of PCBs, which occurred via a reductive process, generating no toxic oxidation products. It is anticipated that this unique light-activated system could establish the foundation for the development of new class of materials for sustainable reactivity that is dependent upon the use of $H_2$, including industrially important reactions such as olefin hydrogenation.

## Chapter 5: Case study: Hydrothermal synthesis of $MnSb_2Se_4$: Effect of surfactant on magnetic properties

### 5.1 Introduction

In recent years there has been considerable interest in transition metal - heavy main group metal chalcogenides as a result of their unique chemical and physical properties.[75-78] These properties include high energy efficiency conversion,[79,80] spintronics,[81-83] thermoelectrics,[77,83] solid state lighting and batteries,[85,86] photovoltaics,[79,87-89] optics, and optoelectronics.[90,91] The chemistry and materials interest in the chalcogenides is strongly tied to the need for low cost, high performance and environmentally friendly materials for energy, electronics, and to mimic biological system for medical applications.[78,80,92] For example, ternary and binary chalcogenide such as $CuInS_2$, $CuInSe_2$, $AgInS_2$ , $CuFeS_2$ , $FeSe_2$, $CuZnSb_2Se_4$, $CuSe_2$ and $CuInSe_2$ have been explored for new high-performance photovoltaic solar cell materials, thermoelectrics, and bioimaging probes.[80,87,88,90,92-96] The properties of the main group and transition metals are, however, sensitive to the specific synthetic method employed, and especially when examining the characteristics of the nanophase, where properties are often strikingly different from their bulk counterparts.[76,86-88,97] The exploration of nanostructured transition metal and heavy main group metal chalcogenides therefore presents a pathway to efficiently discover exceptional properties, with significant unrealized potential. The current library of nanophase chalcogenides continues to grow exponentially, with diverse morphologies such as nanowires, nanorods, nanospheres and nanosheets. The shape and size control of such materials has been significantly aided by the development of new colloidal synthesis methods. For example, nanocati and spherical particles of high Curie temperature $Fe_{3-}$

$_xCr_xSe_4$ with giant coercivity has been reported recently via colloidal synthesis,[98,99] and nanocrystals (NCs) of $Cu_2ZnSnS_4$, $Cu_2ZnSnSe_4$, and $CuZnSnS_xSe_{4-x}$, with the wurtzite-type structure have been explored by the same methods and demonstrate exception photodetector properties.

Within these transition metal-heavy main group metal chalcogenides, those with general formula $MSb_2Q_4$ (M = Mn, Fe; Q = S, Se) are of particular interest for their magnetic properties. [81-83,99-103] The $MnSb_2Se_4$ and $MnSb_2S_4$ for example, which crystallize in monoclinic crystal symmetry, have shown antiferromagnetic (AFM) ordering with Neel temperature $T_N$ ~ 21 K and 25 K. [101,103] Anisotropic multiferroic behavior with the ferroelectric polarization of ~ 14μC/m$^2$ is predicted in $MnSb_2S_4$.[100] More recently, Cu-doped $MnSb_2Se_4$ has been reported as very good thermoelectric material with a figure of merit ZT~0.64 in addition to the very low thermal conductivity that is remarkable in the Cu-free composition.[104] Interesting magnetic properties have also been observed in a Sn-doped phase of $MnSb_2Se_4$ with a remarkable switching from dominant AFM interactions in the Sn-free sample, to ferromagnetic (FM) interactions with $T_c$ ~ 56 K on the introduction of Sn.[103] Nanostructures of $MnSb_2Se_4$ have not been reported, however, and warrant special attention given the rich field of properties observed in bulk $MnSb_2Se_4$. [101,103,104] Here we report the colloidal synthesis of micron to nanophase $MnSb_2Se_4$ using different surfactants. We observe nanowire formation with diameters strongly influenced by the nature of the surfactant, with magnetic anomalies below 40K. Furthermore, a weak ferromagnetism is observed whenever (1-Hexadecyl) trimethylammonium bromide (CTAB) is used, despite the samples remaining phase pure

$MnSb_2Se_4$. This demonstrates the first report of FM within pure $MnSb_2Se_4$, using only morphology control (rather than doping) to determine the magnetic properties.

## 5.2 Methods

All samples were characterized by powder X-ray diffraction collected on a Bruker D8 Advanced diffractometer with $CuK_\alpha$ radiation ($\lambda$ = 1.54056 Å). The morphology of the nanostructures was observed by scanning electron microscope (SEM, S-4800). The high-resolution images, as well as the composition from the energy dispersive X-ray spectroscopy (EDS), were collected using a JOEL 2010F (200 kV) transmission electron microscope. The temperature- and field-dependent magnetization were performed using Superconductivity Quantum Interference Device (SQUID) MPMS. The samples were loaded into a gelatin capsule, which was sealed with a small strip of scotch tape and suspended inside a standard drinking straw. The sample was then loaded into a Quantum Design Magnetic Measurement System (MPMS) for M(T) and M(H) scans. M(T) scans were completed after zero field cooling the sample to the desired starting temperature of the scan and then applying a magnetic field. Data was taken as the sample was warmed to 400 K under an applied field of 500 Oe and then cooled again to the starting temperature, allowing for any hysteresis in the M(T) scans to be detected. M(H) scans were prepared in the same manner and data was taken as the field was swept to +/- 5T.

## 5.3 Results and discussions

All three preparations obtained under different surfactants and surfactant concentrations were metallic light gray with little reflective lustre. The powder X-ray

diffraction (XRD) data of all of the polycrystalline as-prepared samples are presented in Figure 5.1.

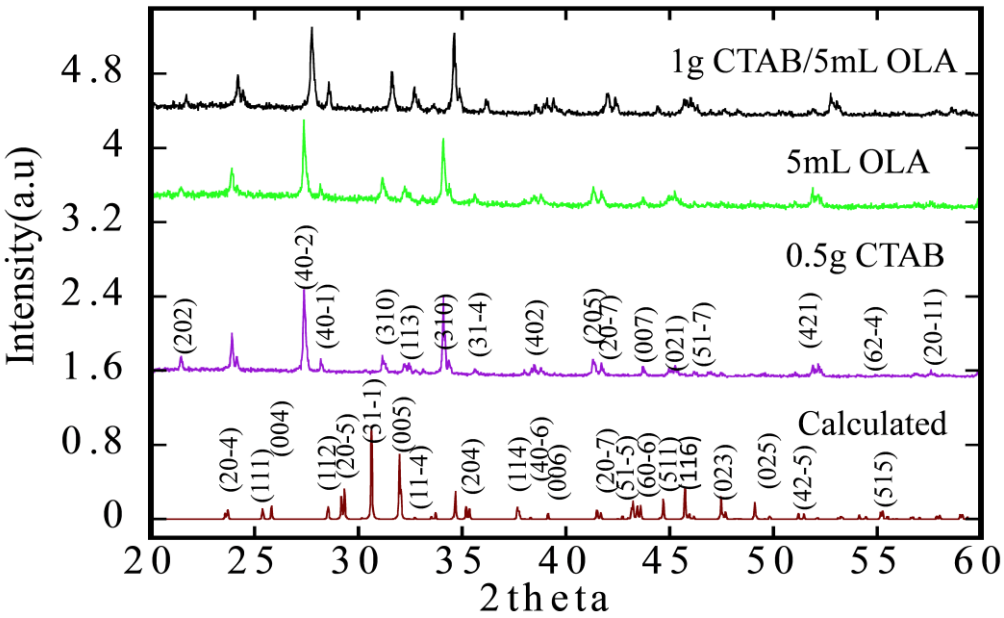


**Figure 5.1** Powder X-ray diffraction of $MnSb_2Se_4$ prepared in 1g CTAB, 5mLOLA and mixture of 1g CTAB/5mL OLA.

The diffraction patterns can be readily indexed to the monoclinic crystal structure of reported $MnSb_2Se_4$ (ICSD no. 421940) with lattice constant $a$ = 13.076(3) Å, $b$ = 3.9651(8) Å, $c$ = 15.236(3) Å and β = 115.07°. Indexed reflections (Fig. 5.1) (201), (20-3), (40-2), (40-5) which seem to be absent from the experimental diffraction pattern or appear with weak intensity on the calculated pattern, all belong to [010] plane of the crystal. This may suggest that the $MnSb_2Se_4$ could have a preferential growth direction presumably along the *b*-axis The morphologies of the nanostructures of $MnSb_2Se_4$ prepared under different conditions as described above are characterized by SEM as shown in Figure 5.2.

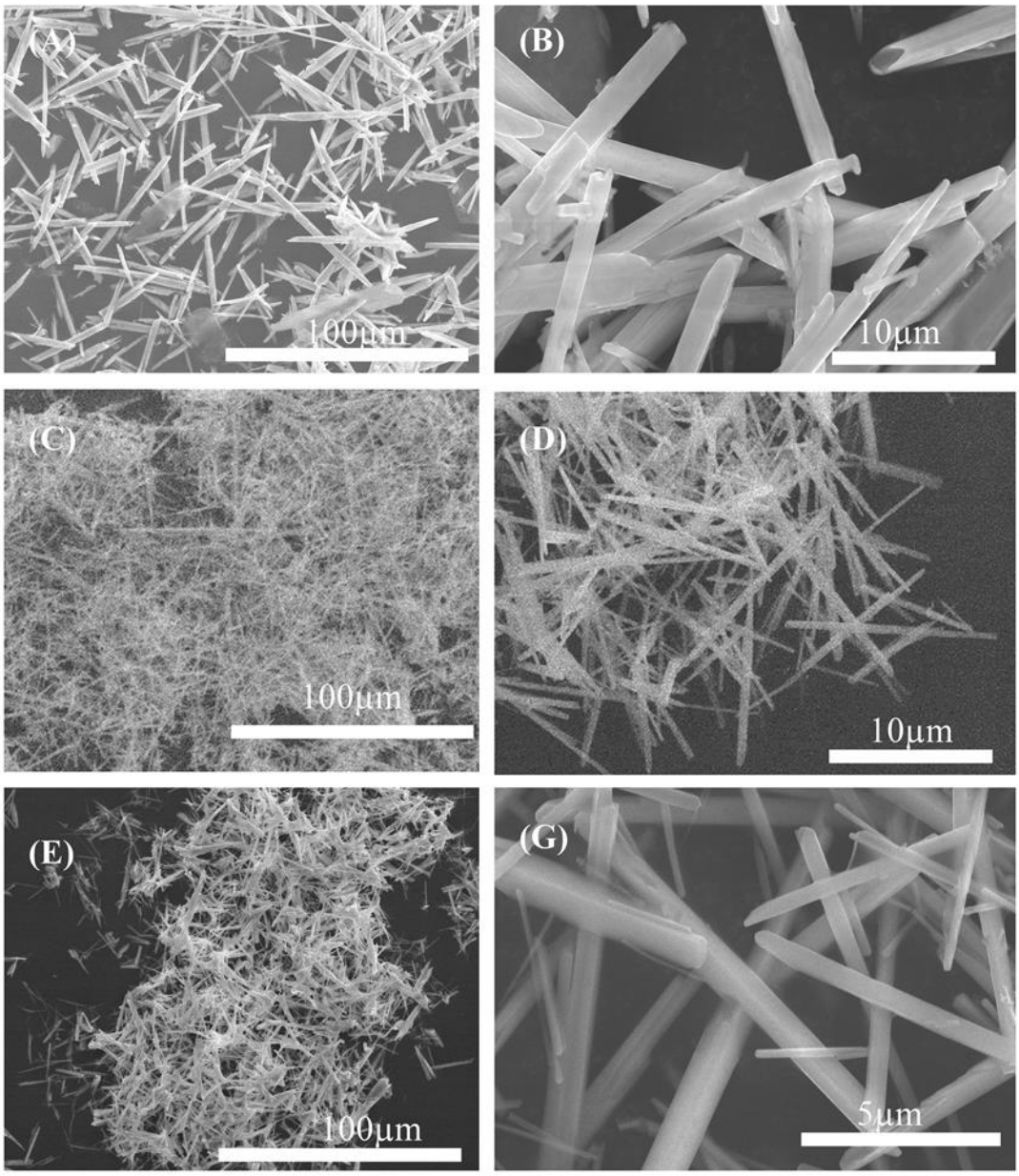


**Figure 5.2** SEM images of $MnSb_2Se_4$ for different preparations with rods and filaments (A, C, and E) morphologies. The inset on B show hollow tube obtained with 1g CTAB. (B), (D) and (G) are high magnification images of the samples prepared in different conditions. (CTAB (A and B), OLA (C and D), CTAB/OLA (E and G))

The low magnification and high magnification of as-grown particles are strikingly affected by the surfactant (Fig. 5.2A-2G). From lower magnification $MnSb_2Se_4$ prepared in CTAB and mixture of CTAB/OLA are all non-uniform (Fig. 5.2A and Fig. 5.2E) rods

compared to the filament morphology of the sample growth in OLA (Fig. 5.2C). The relative diameters of $MnSb_2Se_4$ synthesized in the 1.0 g of CTAB range from 0.8 µm to 5 µm (Fig. 5.2B), and are relatively larger than particles from a mixture of 1.0 g CTAB/5 ml OLA with a relative diameter between 150 nm to 1400 nm (Fig. 5.2G). The particles obtained from pure OLA have a diameter between 150nm to 800nm (Fig. 5.2D) with average particle diameter ~ 300nm – relatively smaller than the average particle diameter obtained with a mixture of CTAB and OLA (~400 nm). This suggests that the CTAB enhances the lateral growth of the particles. The CTAB is known to minimize the surface energy of certain crystals to induce anisotropic growth of the particles.[97] Such preferential surface absorption could explain the difference observed in the particles synthesized. Additonally, the inset to Fig. 5.2B shows that some particles exhibit hollow structures when grown with CTAB. This might be anticipated from the 2D-type structure of $MnSb_2Se_4$.

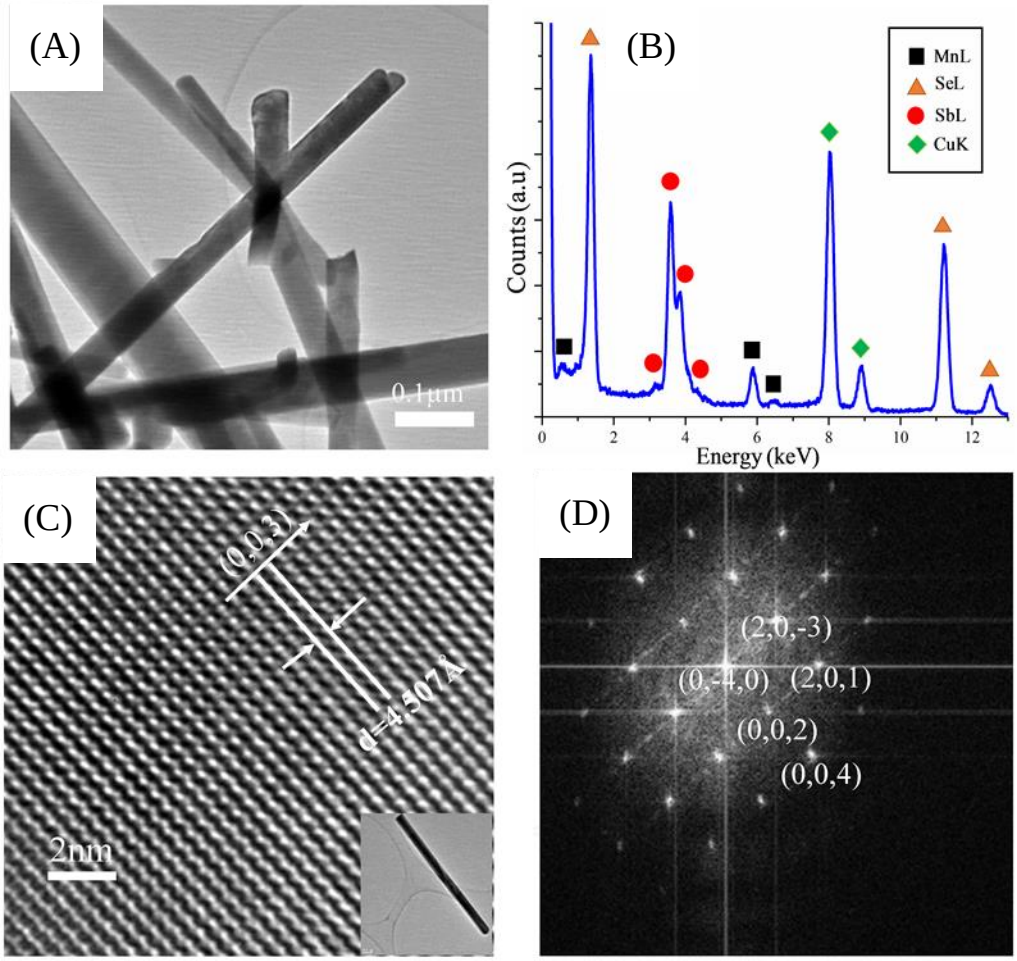


**Figure 5.3** The TEM images observed at higher magnification of nanarods (A), the EDX (B) showing all the elements expected on $MnSb_2Se_4$. The high resolution TEM (C) showing lattice planes consistent with the d-spacing of (003) equivalent the observed d-spacing of $MnSb_2Se_4$ in monoclinic crystal symmetry. The fast fourrier transom of the HRTEM (D) is indexed.

The crystal structure of $MnSb_2Se_4$ and its composition was further investigated using the transmission electron microscope to collect higher resolution images (Fig. 5.3). HRTEM of the sample grown with 1.0g CTAB (Fig. 5.3A) confirmed the rod-like structure of $MnSb_2Se_4$. From energy dispersive X-ray spectroscopy (EDX) spectra on several typical crystals (for example, Fig. 5.3B) only Mn, Sb and Se were detected. Close examination by HRTEM of selected rodlike crystals (shown on the inset to Fig. 5.3C) suggests that the nanoparticles are single-crystalline nanorods. HRTEM of selected rods

show lattice planes parallel to the long axis of the single crystal. The lattice planes are spaced at approximatively 4.507 Å, corresponding to (003) plane of monoclinic $MnSb_2Se_4$. The Fast Fourier Transform (FFT) (Fig. 5.3D) shows lattice planes projected along the (0-40) zone axis. All the lattice plane calculated from the image are consistents and equivalents to the monoclinic crystal structure symmetry of $MnSb_2Se_4$ projected on (0-40).

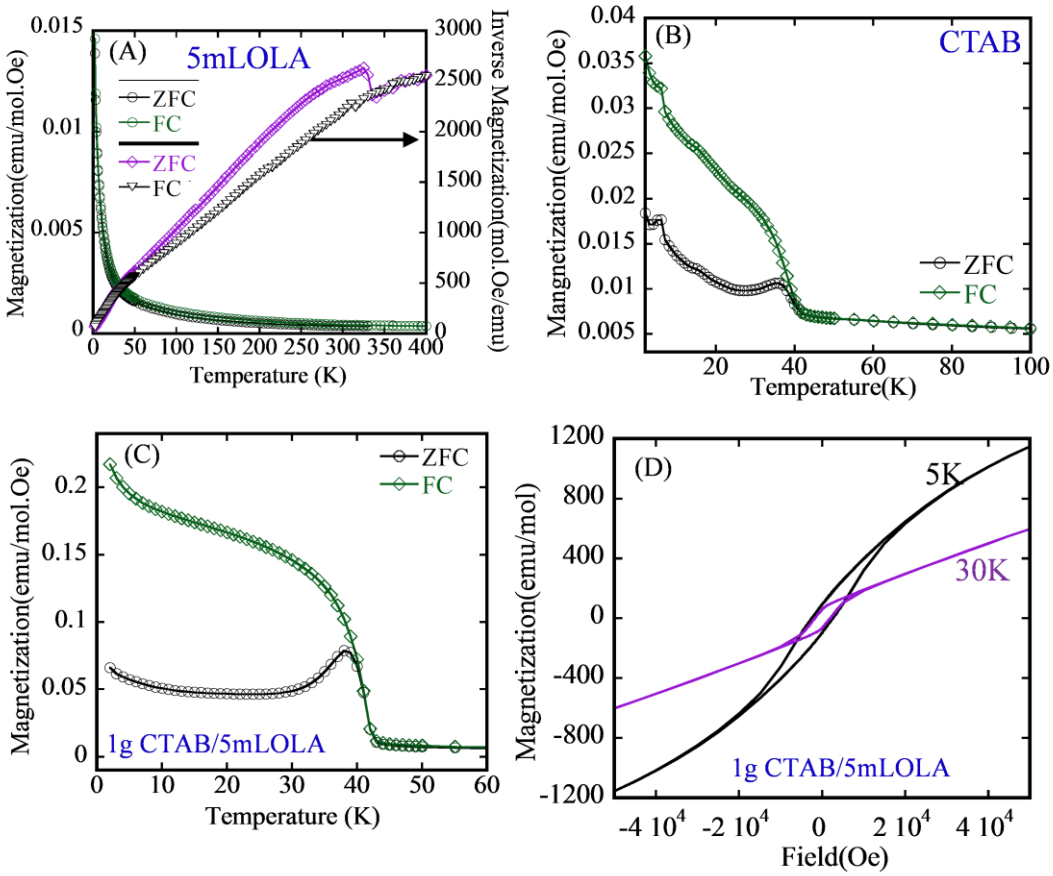


**Figure 5.4** Magnetic properties of $MnSb_2Se_4$ microstructures. (A-C) Temperature dependence field cooled(FC) and zero field-cooled (ZFC) magnetic susceptibility measured under 500 Oe. (A) show the inverse susceptibility versus temperature. (D) Magnetization as function of field at 5K and 30K.

**Magnetic Properties**

Figure 5.4 shows the temperature and field dependence magnetization of the different nanostructures of $MnSb_2Se_4$ at different synthesis conditions. The temperature dependence was measured under applied field of 500 Oe in the temperature range from 2 K to 300 K. The zero field cooled (ZFC) and field cooled magnetization of $MnSb_2Se_4$ nanostructures grown in 5 mL OAL as well as for other wires grown from CTAB and 1.0g CTAB/5 mL (OAL) were found to be strikingly different from magnetic behavior of the bulk phase,[27] which is reported to be AFM with Neel temperature $T_N \sim 21$ K. The magnetization of the $MnSb_2Se_4$ under 5 mL OLA (Fig. 5.4A) increases with decreasing temperature with the ZFC and FC superimposing almost to each other. This means that magnetization of these wire is not field dependent. Such behavior is typical for paramagnetic materials, however the inverse magnetization could not be fitted to the Curie-Weiss law or Curie law, suggesting that the magnetic interaction may be dominated by another type of interaction than paramagnetism and is presumably a spin glass. The magnetization of $MnSb_2Se_4$ nanostructures obtained in CTAB (Fig. 5.4B) and the mixture of CTAB and OAL present a magnetic anomaly with ordering below 40 K. The magnetic susceptibility of both samples shows an increasing magnetization with decreasing temperature with strong field dependence of the magnetization. This may suggest the presence of FM ordering in this nanophase. The field dependence magnetization of wires grown in CTAB, however, suggests paramagnetism in this particular sample while a weak FM ordering with coercivity force of 2500 Oe is observed at 5K and 30k in the wire synthesized with a mixture of CTAB and OAL as surfactants. Yet, the hysteresis loop did not reach the magnetization at an applied field of 60 KOe,

suggesting that there is a high anisotropy field or disorder due to noncollinear spin in the nanostructure. It is also well known that $MnSb_2Se_4$, $MnSb_2S_4$ and $FeSb_2Se_4$ [8,9,27,29] are subject to spin canting at very low temperature in the bulk phase. This may suggest that within the whole nanostructure, the coupling is due to canting AFM, with uncompensated magnetization at grain boundaries responsible for the weak ferromagnetism we observed in the sample prepared in CTAB. The hollow structure of the nanowires obtained whenever we used CTAB may also effect the magnetism in the nanophase, though the specific role that this morphology plays on magnetic ordering in $MnSb_2Se_4$ is still under investigation. It is important to note that only samples prepared under CTAB exhibited magnetic anomalies.

### 5.4 Conclusions

Nanostructures of $MnSb_2Se_4$ were readily obtained using low-temperature colloidal synthesis. Weak ferromagnetism can be obtained by adjusting the composition of the surfactant. The Curie Temperature Tc, ~ 40K with Coercivity force of 2500 Oe, was observed with a mixture 1.0g CTAB/ 5ml OAL. X-ray diffraction confirms the purity of the materials suggesting preferred orientation growth of the wires and rods along the b-axis.

## Chapter 6: Plasmon mapping of hetero-structured nanowires

### 6.1 Introduction

Plasmonic materials have generated great interest in recent years because of their outstanding optical properties and wide range of potential applications. A plasmonic material is characterized as one which displays a localized surface plasmon resonance (LSPR), which is a collective oscillation of the conduction electrons on the surface of a metallic nanoparticle.[105] A LSPR mode is typically excited by an incident electromagnetic field, although fast moving electrons can also excite the LSPR. The LSPR is of particular interest because the discrete energies of different plasmon modes can be tuned by the size, shape and the surrounding environment of an individual nanostructure,[106] and the resonance energy scale overlaps with that of visible light, which means LSPR modes of noble metal nanostructures have the potential to be used in applications such as wave-guiding,[107] photonic circuits,[108] and bio-sensing devices.[109,110] The plasmonic characteristics can further be manipulated when multiple similar nanoparticles are organized in an ordered array, such that coupling may occur, resulting in additional and tunable LSPR modes, and the ability to direct and even propagate electromagnetic radiation. These tunable characteristics have the potential for a wide range of energy and optical applications. Though noble metal particles arranged on a surface, with coupling propagated through a vacuum, have been widely investigated, less attention has been focused by the plasmonics community on metal particles embedded within a solid matrix; embedded particles have several potential advantages, however, such as the ability to develop spontaneously as part of the synthetic process, and the

versatility of a variety of dielectric environments which further act to protect the particles.

In recent years, nano-rods, nano-belts, nano-dots and many other kinds of nano-structures have drawn great attention because of their stunning optical and electric properties; their novel applications such as wave-guiding, bio-sensing and photo-electronic devices greatly enriched the field of nanotechnology. Among these nano-structures, nanowires seem to be the most functional with a wide range of applications. Specifically, hetero-nanostructures such as core–shell nanowires and nanopeapods have attracted great attention because of their unique optical and electrical properties. These heterostructured systems are of particular interest due to their potential for wave-guiding applications, and their excellent photoelectric response. Among these materials are systems as diverse as Au in $Ga_2O_3$ peapod nanowires,[152] peapod-like Ni@mesoporous carbon core-shell nanowire,[157] $\alpha$-$Si_3N_4$/Si-$SiO_x$ core-shell/Au-$SiO_x$ peapod-like axial double heterostructures,[134] Au embedded ITO nanowire,[151,158] Pt@$CoAl_2O_4$ nanopeapods,[159] $Fe_3O_4$/$SiO_2$/$TiO_2$ peapod-like nanostructures,[160] and InN/$In_3O_4$ peapod nanostructures.[161] Among these, the Au embedded gallium oxide and the Au embedded ITO nanowires are of most interest to us, since they display the most well-defined metal/metal oxide interfaces.[162] These two systems are surprisingly similar: they are made by the VLS growth mechanism, catalyzed with Au, show a remarkable photoelectric response, and both have corundum structures. The purpose of our research is to study the growth mechanism and plasmonic behavior of these systems, and use our findings to design new nanowire heterostructures in which we tailor the materials and properties. To do this we will first reproduce the two existing core-shell and peapod

nanowire systems, and then experiment with different metal catalysts, metal oxide encasings, and catalyst particle diameters.

We are investigating several composite systems in which noble metal nanoparticles assemble as part of the synthesis process, including Au and Ag particles encased in hexaniobate scrolls, and Au particles embedded in metal oxide nanowires, in which spherical shape Au particles are reduced from $Au^{3+}$ in solution and are encapsulated in Hexaniobate nanoscrolls and forced to form Au particle chain uniformly.

In this project, we use scanning transmission electron microscopy-electron energy loss spectroscopy (STEM-EELS) to elucidate the relationship between the synthetic processes and the resulting plasmonic coupling. EELS maps are taken in selected areas where covers two or more Au particles with similar size and spacing in the peapod structure. The energy loss signal comes from the transmitted inelastic electrons that are collected and measured by the electron spectrometer which may be absorbed by the sample to excite certain LSPR modes.

### 6.2 Solution phase synthesis and electron beam lithography

Plasmonic materials have been synthesized and fabricated by a large number of varying techniques, most commonly the bottom up approach of synthesizing individual metal nanoparticles,[111-114] and the top down technique of electron beam lithography.[115-119] Synthesizing individual particles in solution has the advantage of being able to build up complex nanostructure architectures from individual nano-scale components in order to improve and tune the desired properties of the used components through the fabrication process, whereas lithography enables short-wavelength light sources to pattern and build

nanostructures without the need for further assembly steps. Within the large body of literature detailing solution-based nanoparticle synthetic methods, the photo-mediated approach of the group of Chad Mirkin has drawn particular interest by the plasmonics community, due to their demonstrated systematic control of the shape of Ag nanoparticles, for example in the synthesis of Ag nanoprisms from spherical nanoparticles, and subsequent control of the optical properties.[120]

Lithographic fabrication of arrays of metallic nanodots, for example by Maier et al,[121-127] has also drawn intense interest, due to demonstrations of applications such as optical data storage and optical wave-guiding arising from the ability to control nanoparticle shape and size to produce the desired LSP modes.[107,108,128,129]

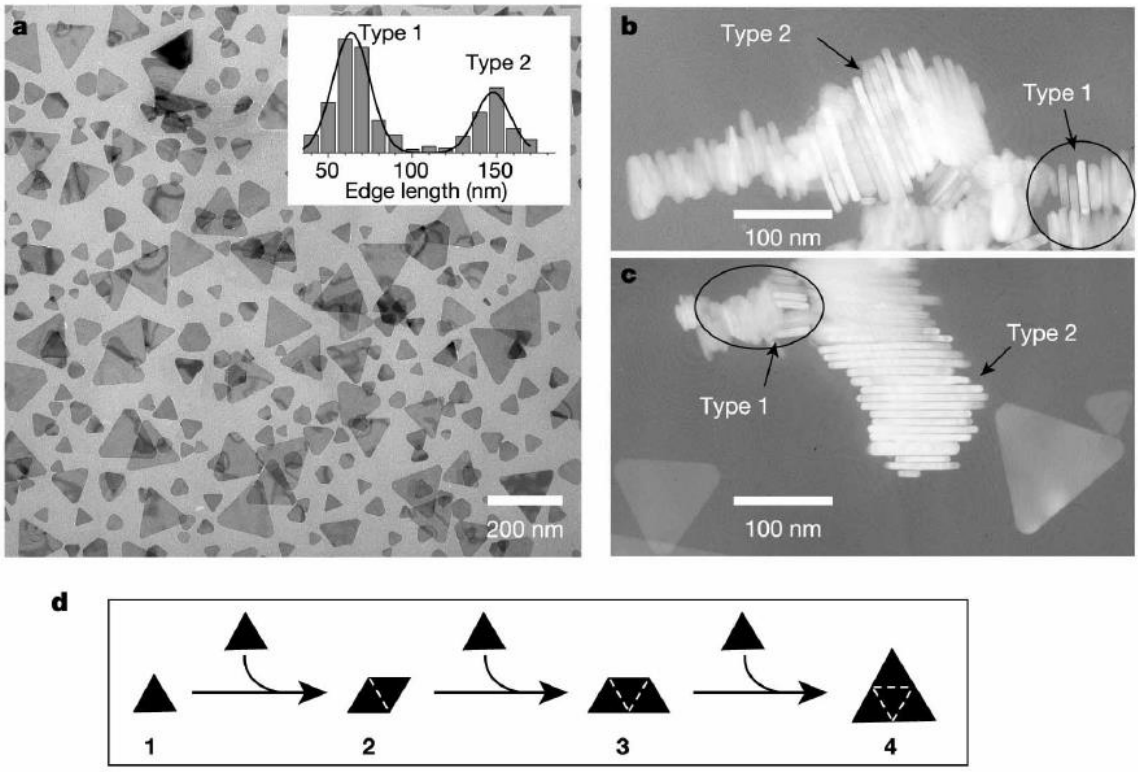


**Figure 6.1** Schematic showing (a) silver nanoprisms and their size distribution. (b, c) TEM images showing two types of silver nanoprism stacking. (d) Schematic showing light-induced fusion growth of silver nanoprisms.[204] (Figure adapted from Ref. 204)

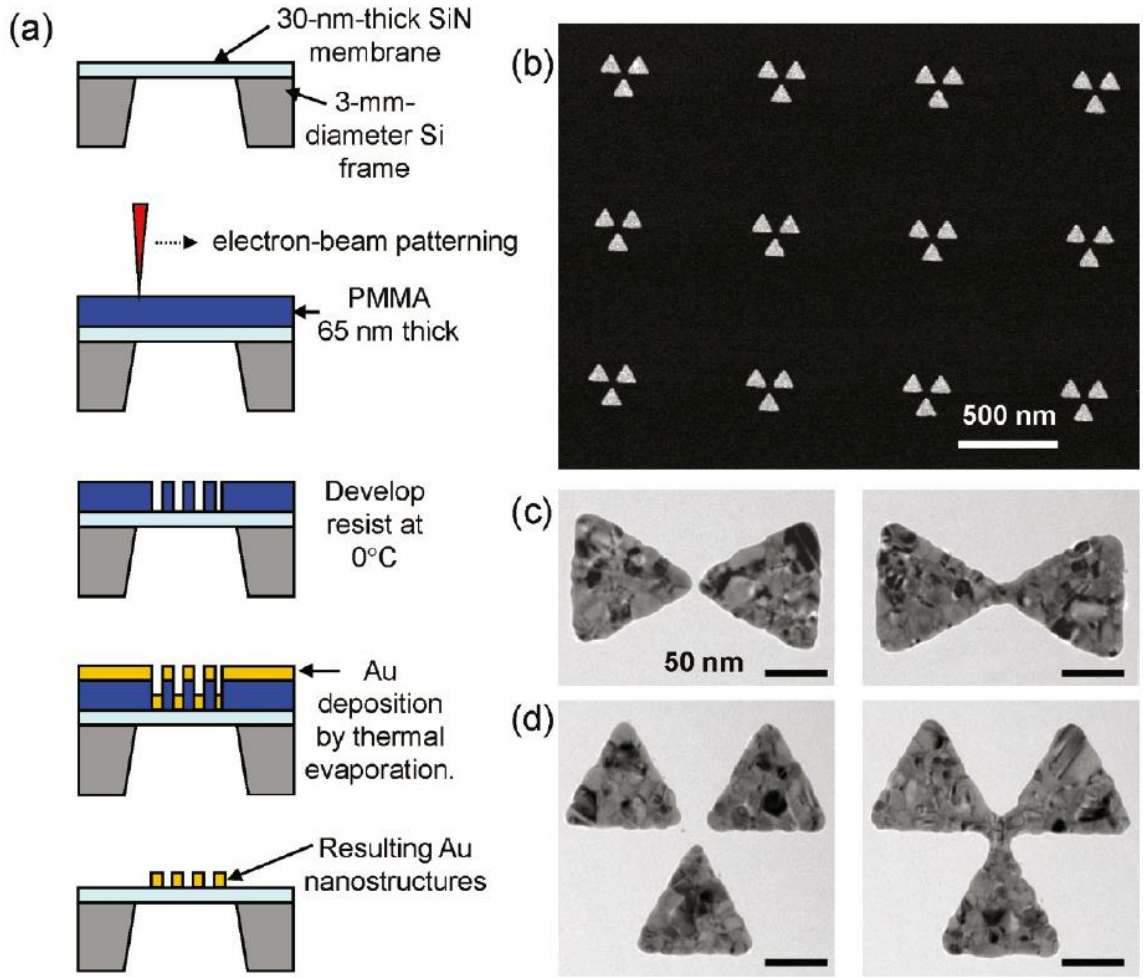


**Figure 6.2** Schematic of (a) Electron lithography patterning metal nanostructures on a SiN membrane, (b) Dark-field image of an array of patterned nanostructures, (c,d) Bright field images of two disconnected triangles (c, left); two connected triangle (c, right), and (d) Three disconnected triangles (d, left); three connected triangles (d, right).[205] (Figure adapted from Ref. 205)

### 6.3 Chemical vapor deposition

CVD is a well-known process to deposit high purity particles,[155,156] in which a quartz tube acting as reaction chamber is heated up to a certain temperature for the starting materials to become vapor phase. The pressure inside the chamber is usually reduced in order to create a low contamination environment, and to encourage sublimation of solid state reactants. The vapor phase chemical will be carried by inert carrier gas to react or

decompose on a substrate contained downstream from the reactant, in a cooler part of the furnace. The CVD system can be divided into three major parts: (a) the reaction chamber, (b) the vacuum pump and (c) the flow system. A schematic diagram of CVD system is presented in Figure 6.3.

a. The reaction chamber is made of a quartz tube with one-inch diameter which is placed horizontally inside the furnace. The furnace is programmable to control the reaction temperature, ramping rate and the reaction time.

b. The vacuum pump (combined with a valve which is used to control the efficiency of the pump) controls the pressure inside the reaction chamber.

c. The flow system is equipped with a mass flow controller in order to control the flow rate of carrier gas which is directly related to the concentration of starting material in vapor phase.

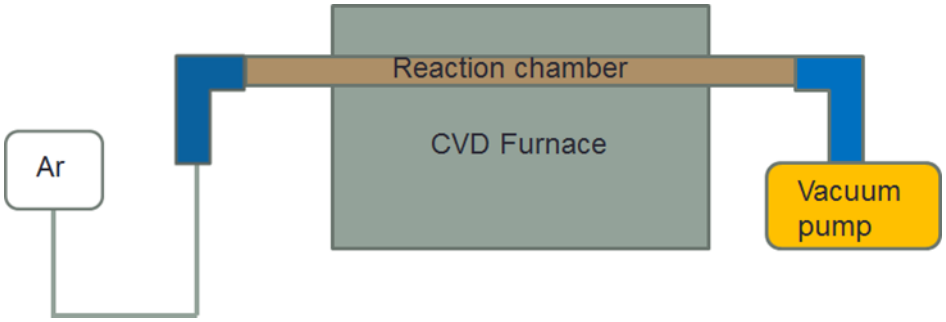


**Figure 6.3** A sketch of CVD furnace.

In this thesis we will discuss three systems in which we attempt to assemble arrays of metallic nanoparticles using synthetic methods, and characterize the resulting plasmonic functionality with a variety of techniques – both established and under development.

First, we will discuss the use of chemistry to spontaneously assemble metallic particles within the casing of a single nanowire, in the form of a peapod nanowire

morphology. In recent years, core-shell and peapod metal oxide nanowires have drawn attention because of their excellent photoelectric responses. They are grown by a vapor phase synthesis which is different from more conventional solution growth or lithographic methods.

A detailed understanding of the synthesis and the plasmonic behavior might be valuable not only to improve the system response but also to develop diverse optoelectronic devices. The systematic growth of one dimensional nanostructures such as the metal/metal oxide nanowire systems in which we are interested, have been reported by a number of groups,[130-135] using a chemical vapor deposition method. These groups report that these nanowire heterostructures were synthesized by a vapor-liquid-solid (VLS) mechanism which uses a metal droplet as a soft template to limit nanowire lateral growth.[136,137] However, metal droplets may end up with different morphologies depending on different experimental parameters. In this paper we experiment with different growth parameters, metal particles, and metal oxide encasing materials, to design and control the growth of these nanowire heterostructures.

Secondly, we will discuss the assembly of arrays of nanorods in solution, using a bio-molecule mediated approach, in which nanorod chains will be formed. A new characterization technique will be described in which a liquid cell TEM holder is utilized as a reaction chamber for solution phase chemical reactions, allowing in situ observation of nanoparticle chain assembly. By monitoring the assembly under a variety of experimental conditions, the importance of factors such as ligand structure, pH, and concentration on assembly rates may be determined. Biomolecule mediated plasmonic coupling will also be studied using both dark-field optical and electron microscopy

techniques. Understanding the plasmonic behaviors of nanoparticle chain assemblies should lead in the long term to the use of this method for the controlled organization of functional plasmonic materials.

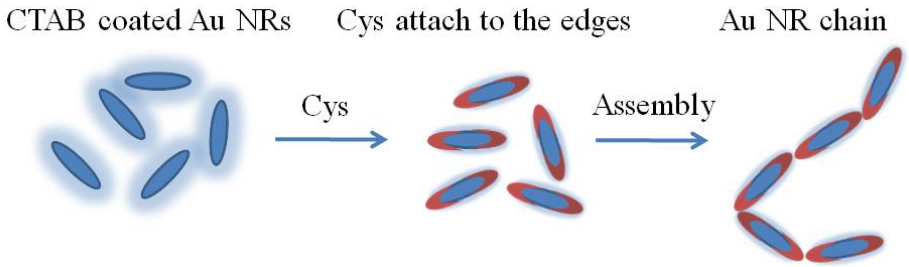


**Figure 6.4** An illustration of bio-ligand mediated nanorod chain formation.

Thirdly, our collaborators at University of New Orleans have successfully synthesized a metal in Hexaniobate nano-peapod nanowires systems using Solvothermal method, the details are discussed in section 2.1.4.

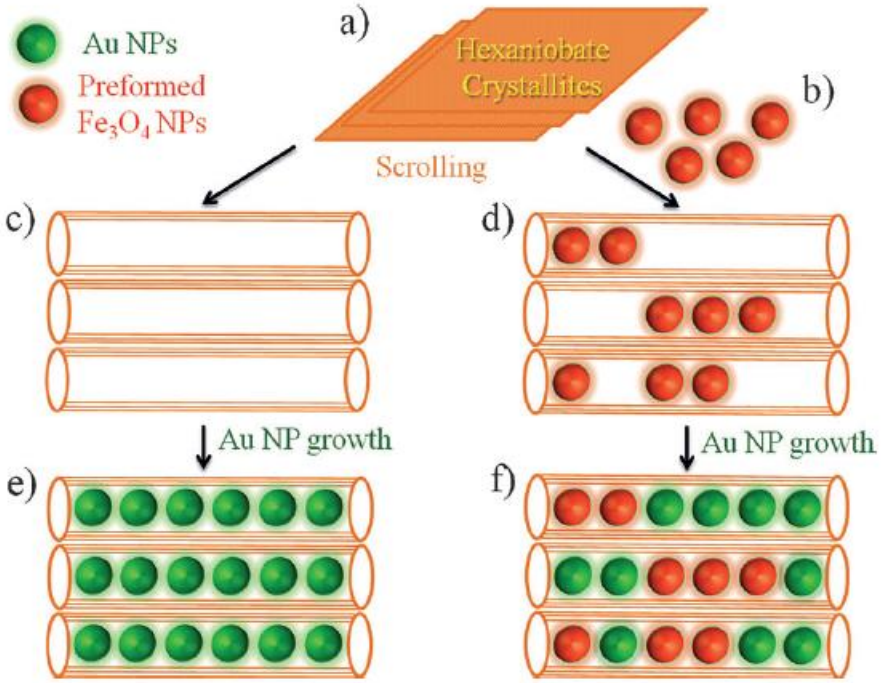


**Figure 6.5** An illustration of metal/metal oxides in hexaniobate nano-peapod formation. (Figure adapted from Ref. 206)

### *6.3.1 Vapor-liquid-solid (VLS) growth*

The VLS growth mechanism is a common formation mechanism for one dimensional nanostructures (nanowires) grown using a CVD furnace.[137,156] This mechanism uses metal nanoparticle catalysts which are usually coated on the surface of the substrate either by electron beam evaporation or drop coating from solution. To form nanoparticle catalysts using the e-beam evaporation technique, a thin layer of metal is coated on the surface, and melts to form liquid droplets during the reaction process. Vapor phase reactants alloy with the catalyst, until the super-saturation point of the liquid metal is reached, at which point the precipitation of high purity nanowires starts to occur at the liquid/solid interface. The metal catalyst head is pushed out perpendicular to the substrate as nanowires with uniform diameter are grown. A schematic illustration of VLS growth is shown in Figure 6.6.

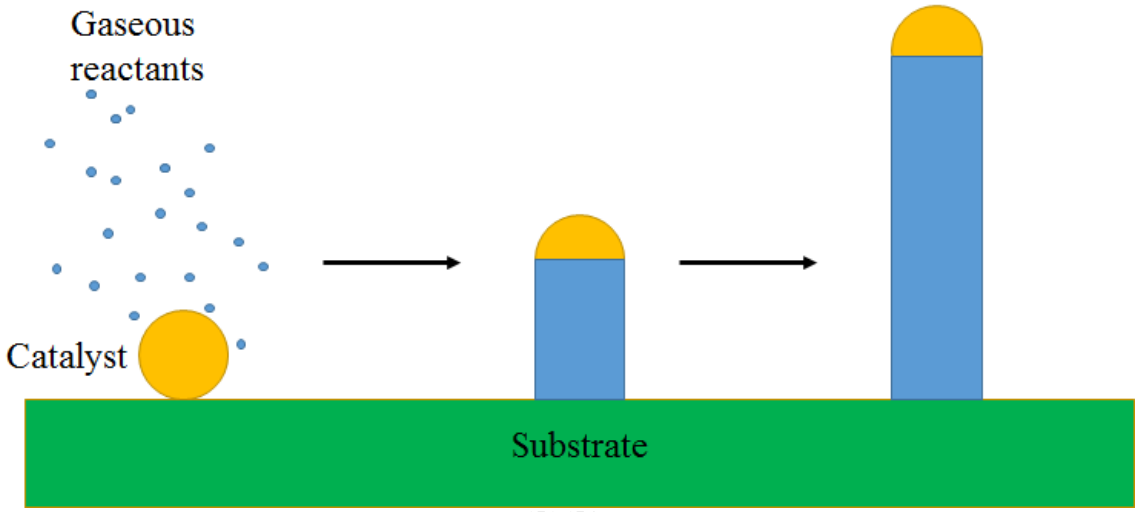


**Figure 6.6** An illustration of VLS growth.[151-154]

### *6.3.2 Preparation of $SiO_2$ substrate*

Before depositing Au, the substrates are sonicated to clean the surface with three different solvents: acetone, isopropanol and DI water. The substrates are sonicated for three minutes with each solvent and dried under Argon gas to remove any residual water from the surface.

### *6.3.3 Gold catalyst deposition*

We use two methods to deposit Au catalyst nanoparticles onto our growth substrates:

1. 2 µL of commercially available Au nanoparticle solution (available in diameters from 2 to 100nm) is applied to the substrate by micro-pipette and dried in an oven at 120$^{o}$C for a few minutes. This method is quick and easy but produces low quality substrates, since the particles are not evenly dispersed, and are coated with an organic stabilization ligand from solution. Figure 6.7 shows two SEM images of Au nanoparticles on substrates prepared by this method.
2. An electron beam evaporator is used to deposit a thin layer of Au onto the substrates in a vacuum chamber. This method is more time consuming and complex, but produces high quality Au nanoparticles which are evenly dispersed and have low contamination. The thickness of the Au can be precisely monitored and controlled by Crystal Monitor. We use 4 nm of Au for the ITO project, and a 40 nm layer for the gallium oxide project. Thermal annealing of the substrate during the reaction causes a balling up of the Au film into small particles, which act as the catalysts for nanowire growth.

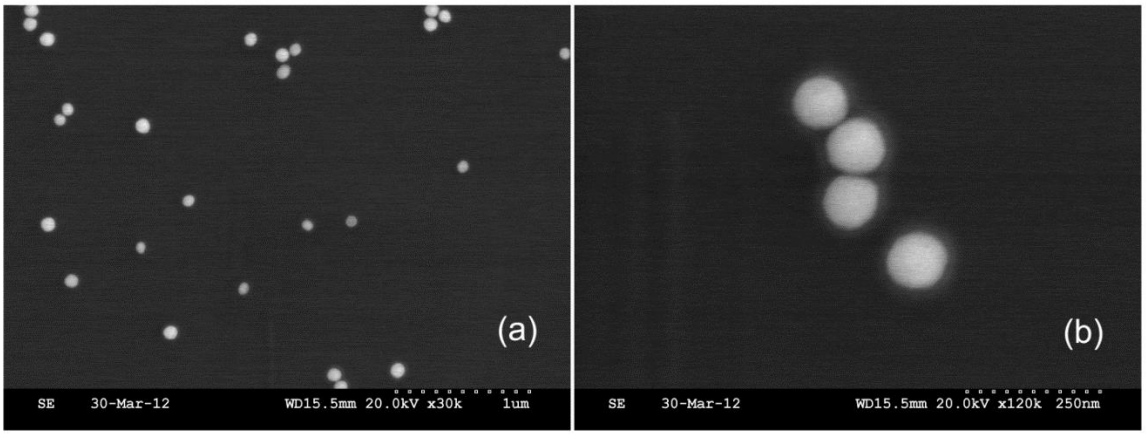


**Figure 6.7** SEM images of Au nanoparticle catalysts on substrates. Image (a) shows Au nanoparticles are well dispersed on substrate. Image (b) provides a closer look at Au nanoparticles and their diameters are roughly 100 nm.

### *6.3.4 $Ga_2O_3$ nanowire synthesis*

Gallium oxide usually exists in ambient condition in β-$Ga_2O_3$ which is known to be a wide band gap material ($E_g$≈4.3 eV).[159] The conduction and blue luminescence properties have made it a well-discussed compound which is also a popular material for semiconductor fabrication.[161] However, the material we have synthesized may actually be the hexagonal α-$Ga_2O_3$, which was reportedly observed under high pressure and in nanostructures.[164] In α-$Ga_2O_3$, the Ga atoms occupy 2/3 of the octahedral sites and the oxygen atoms have a hexagonal close packed arrangement, which makes the α-$Ga_2O_3$ a corundum structure.[165] The starting material for $Ga_2O_3$ project is a gallium metal pellet. Core-shell structures are made in the lower temperature range between 600 to $800^{o}C$. The peapod structures are made at temperature higher than $800^{o}C$. The reaction temperature is set to $800^{o}C$ in $Ga_2O_3$ project with the ramping rate of $20^{o}C/min$. Argon flow rate is 30 sccm and the pressure is around 0.7 torr.

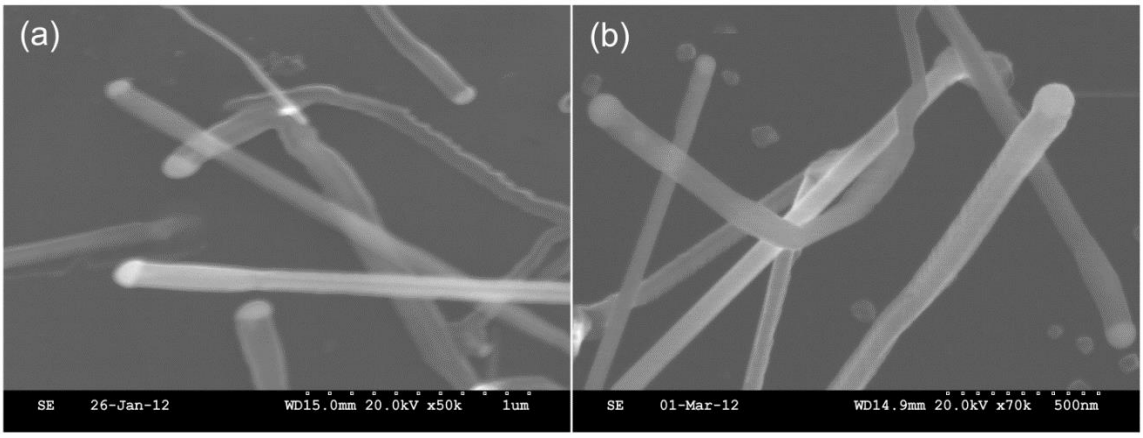


**Figure 6.8** Gallium oxide nanowires produced at reaction temperature of $680^{o}C$ is shown in (a). Image (b) shows nanowires grown under reaction temperature at $800^{o}C$.

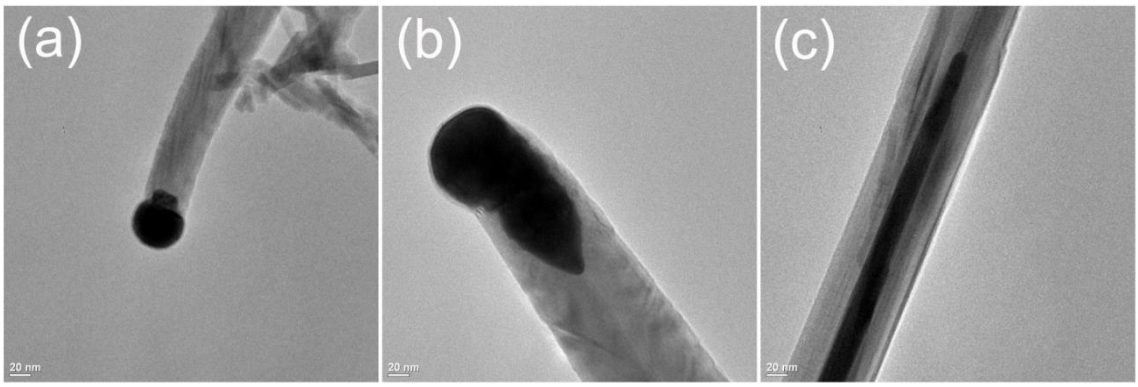


**Figure 6.9** VLS grown Gallium oxide nanowires at different stages in heterostructure growth. (a) A gold head is seen to extend into the body of the nanowire. (b) The gold nanoparticle head extends further into the twin boundary region. (c) A gold core encased in a gallium oxide shell has grown with a well-defined metal/oxide interface.

### *6.3.5 Indium Tin oxide nanowire synthesis*

Tin doped indium oxide is a known n-type semiconductor which combines both conducting and transparency properties with a wide band gap ($E_g$=3.5~4.3 eV).[166] ITO has been used in a wide range of applications such as liquid crystal displays, solar cells, camera lens and etc. Moreover, the tin-doped indium oxide (III) has also been reported to be corundum structure under ambient conditions due to the reduction in effective cation radius effected by replacement of $In^{3+}$ by the smaller $Sn^{4+}$and the formation of cation

vacancies to charge compensate.[167] The starting material for this project is a mixture of $In_2O_3$, $SnO_2$ and graphite with 4:1:1 ratio. ITO project takes two annealing steps; the first stage for the ITO project is to make ITO nanowires while the second stage is to make core-shell, dot rod mixture and peapod structures depending on different annealing temperature. The first annealing stage in ITO project has the following set up: the ramping rate is also $20^{o}C/min$ and the target temperature is $950^{o}C$ for one hour. Two temperature zones are required in this project, the temperature of starting material needs to be $100^{o}C$ higher than the substrate. According to the temperature diagram provided in the user manual of the furnace, the position of $850^{o}C$ can be precisely determined. The argon flow rate is 100 sccm and the pressure is around 1.7 torr. Three different temperatures have been used in the second stage annealing for ITO project which lead to three different structures. With temperatures of $550^{o}C$, $650^{o}C$ and $750^{o}C$, core-shell, rod dot mixture and peapod structure will be made respectively.

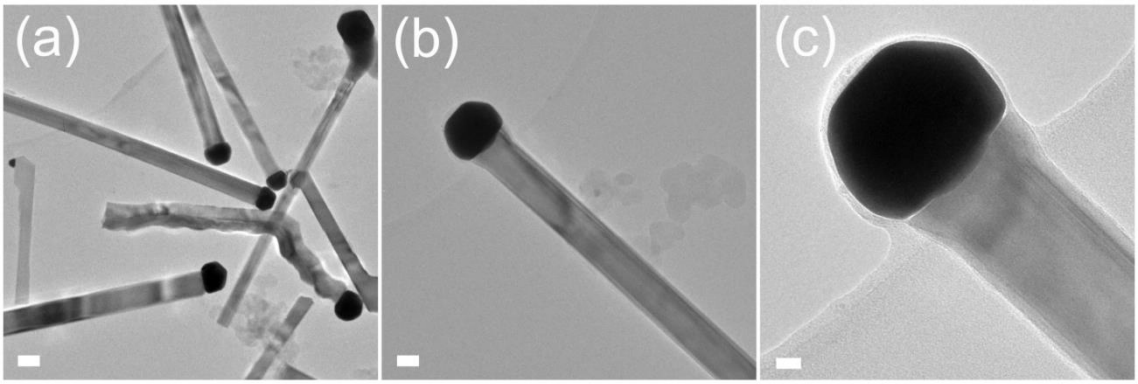


**Figure 6.10** ITO nanowires after the first growth stage. (a) High yield of ITO nanowires. (b) A single nanowire. (c) The same nanowire at higher magnification, showing no twin boundary formation and a distinct gold head as expected. Scale bars are 0.1 µm, 50 nm and 20 nm from left to right.

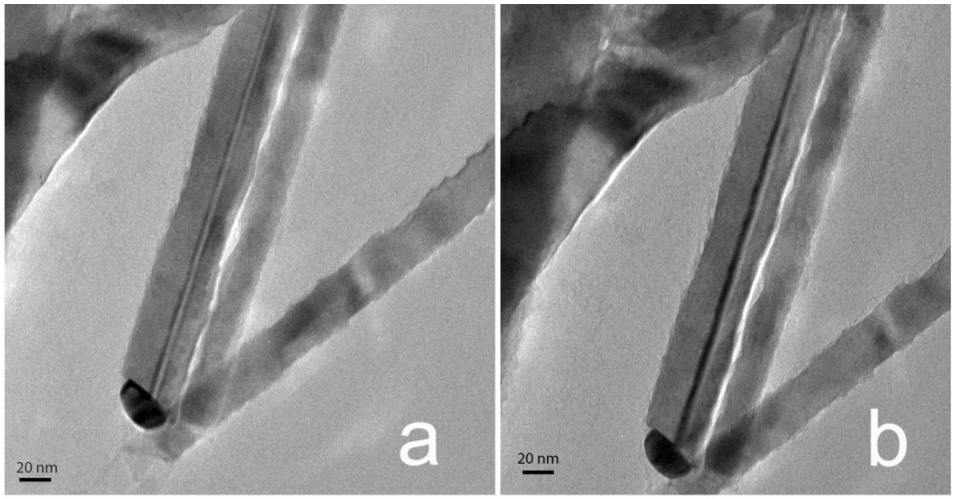


**Figure 6.11** (a) A TEM image taken during the second stage annealing at 650$^{o}$C using an in situ heating holder (images taken by Bethany Hudak). (b) Gold is observed to fill the empty core a few minutes after the heat was turned off.

## 6.4 Case study: Reverse VLS

Parts of this section are taken from "Real-Time Observation of the Solid-Liquid-Vapor Dissolution of Individual Tin(IV) Oxide Nanowires" *ACS Nano*, 2014, 8 (6), pp 5441–5448. All of the nanowires used in this project were synthesized by myself.

### Introduction

The vapor-liquid-solid (VLS) nanowire growth technique is the method of choice for the synthesis of a vast range of single-crystalline nanowires for equally numerous uses.[168-170] VLS synthesis is well-known to be the most effective method of controlling nanowire diameter during nanowire growth, via the size of the metal catalyst particle,[170] and results in wires with easily controlled lengths and high crystallinity. $SnO_2$ is an n-type semiconductor with a wide band gap (3.6 eV at 300 K) and is easily grown in a nanowire morphology using the VLS synthesis. These semiconducting nanowires are building blocks for nanoscale electronics and optoelectronic devices with specific applications to gas sensors,[171-173] dye sensitized solar cells,[174-176] field-effect transistor devices,[177,178] and Li-ion batteries.[179,180] For use in these kinds of devices, nanowires need to be stable at high temperatures and when in contact with metals.[181,182] In addition to pure $SnO_2$, there is much interest in the Sn-rich end of the $SnO_2$-$In_2O_3$ solid solution, for applications such as enhancing the selectivity of $SnO_2$ gas sensors;[182-184] the operating temperatures for both doped and pure $SnO_2$ gas sensors can reach 200-500 $^{o}$C. Though many gas sensing devices are built from thin films,[163,182-184] replacing these with 1D nanostructures can increase their performance due to the increased surface area, aspect ratio, and crystallinity associated with 1D nanostructures.[185,186] It is therefore imperative

to understand the behavior of both pure and doped-$SnO_2$ nanowires at elevated temperatures, and in particular the way in which these nanowires interact with the gold and other metallic connecting materials. For these reasons, we have undertaken a series of in situ heating experiments in which we examine the interaction of $SnO_2$ nanowires with the metal catalyst particle, which is residual at the tip of the wire after VLS synthesis. Our observations should be generalizable to other metal oxide nanowire materials and of relevance to all VLS-grown nanowire systems.

VLS growth is the key mechanism of silicon nanowire growth, and as such has been studied extensively to elucidate the key mechanistic processes and kinetics. The growth process can be divided into three main steps:[187,188] first, a silicon containing precursor is cracked at the surface of a liquid catalyst droplet, usually gold, and silicon is incorporated into the catalyst. In the second step, Si quickly diffuses through the droplet to (what will become) the solid-liquid interface, and the droplet supersaturates with Si. At sufficient supersaturation, Si crystallizes out in the third step of the mechanism to form a nanowire whose diameter depends on the initial droplet size. In the limiting case that only one of these steps is rate-determining, the growth velocity of the wire, dL/dt, may or may not depend on wire diameter. If crystallization is the only rate-determining step, the Gibbs-Thomson effect dictates that dL/dt is inversely proportional to negative wire diameter, so that larger wires grow more quickly. This was the situation described by Givargizov.[189] If incorporation is instead the rate-determining step, dL/dt is independent of nanowire diameter, but will depend on the partial pressure of the precursor vapor, as was observed by Kodambaka et al.[190] It is possible, however, for the actual situation to lie between these two limits, with the rate of growth determined by the interplay between these

steps.[187,188] Additionally, several reports in the theoretical literature[191-193] predict that nanowire growth relies on a steady-state balancing of the nanowire crystallization, with melting or dissolution back into the catalyst, and that it is important to understand both processes, since they rely on different morphological features.

Given the dependence of kinetics on the balancing of several steps, and that wire diameters can vary during growth, understanding the kinetics of growth has been greatly advanced by the real-time observation of nanowire growth in situ in the transmission electron microscope (TEM).[169,190] Recent observations of both the growth of nanowires by the VLS mechanism and also their subsequent annealing have revealed some fascinating behavior of the metal droplet at the tip of the wire. Hannon et al. observed that the catalyst droplets actually change during growth, and that diffusion of Au down the sidewalls of the growing nanowires and across the substrate can result in Ostwald ripening of the droplets, and a resulting tapering of nanowire diameter.[194] This is consistent with an observation by Sutter and Sutter that traces of Au remain on the sidewalls of Ge nanowires after VLS synthesis, and can be used to catalyze the encapsulation of the nanowire in a graphitic coating.[195] Sutter and Sutter also observed the melting and recrystallization of alloy particles at the tips of germanium and GaAs nanowires to find a strong size dependence of the alloy composition, which allowed a tunable depression of the liquidus.[196-198] Finally, metal droplets have also been reported to catalyze a reverse process of the VLS mechanism, dubbed solid-liquid-vapor (SLV), in which the droplet etches a cavity or tunnel in a soluble material to form negative nanowires or whiskers.[199,200]

Here, we use in situ heating in the TEM to observe the kinetics of gold-catalyzed dissolution of $SnO_2$ nanowires with the rutile structure. Observing this process in situ provides physical insight into the mechanism, which suggests that both overcoming adhesion of the Au alloyed droplet to the substrate surface and evaporation at the liquid-vapor interface are likely to be key rate-determining steps.

**Methods**

The nanowires were prepared using a VLS synthesis from the literature.[202] Before starting the VLS synthesis, a silicon substrate was coated in a 20 nm layer of Au deposited by electron beam evaporation. Pure $SnO_2$ nanowires were grown by mixing SnO (Alfa Aesar, purity, 99.996%) and graphite (Alfa Aesar, purity, 99.9995%) powders in a 1:1 molar ratio, and placing the mixture in a quartz tube about 5 in. upstream from a silicon substrate, all contained within a CVD furnace. The system was pumped to 1.7 Torr under 100 sccm of flowing argon, heated to 950 $^{o}$C at 20 $^{o}$C/min, and held at that temperature for 30 min. In-doped $SnO_2$ nanowires were prepared under the same reaction conditions using a 4:1:1 molar ratio of In2O3 (Alfa Aesar, purity, 99.99%)/SnO/graphite. Nanowires were characterized using XRD (Bruker D8 Advanced and Bruker D8 Discover with Cu KR radiation), SEM (Hitachi S-4300), TEM (JEOL 2010F at 200 keV and Hitachi HF-3300 at 300 keV), and EDS (Oxford INCA detector). In situ heating was performed using a Protochips Aduro heating stage, and Camtasia screen recording software was used to record videos. TEM samples were prepared by sonication of the as-grown substrates in methanol, followed by dropcasting onto the relevant commercial substrate-lacey carbon coated copper for TEM imaging, or a Protochips Aduro thermal "E-chip" for in situ TEM heating experiments. The Protochips E-chip comprises a 300

μm μm × 300 μm ceramic substrate which acts as both sample support and heater. As such, temperature changes are virtually instantaneous, resulting in isothermal conditions across the entire supported sample.

**Results and discussions**

We conducted in situ heating experiments in which we anneal $SnO_2$ and In-doped $SnO_2$ nanowires in the TEM, and observe etching of the nanowires by the Au catalyst droplet at their tips. This dissolution process is consistently reproducible under conditions of elevated temperature in the low pressure TEM environment, provided that the wire remains in contact with its gold catalyst head. It can be controlled, stopped, and started by altering the temperature, in many cases eventually leading to complete dissolution of the wire leaving nothing remaining but the original metal catalyst particle. The nanowires for this study were synthesized by a standard VLS growth method, to obtain single crystalline wires with a wide range of diameters from ~20 to 300 nm and lengths varying from several hundreds of nanometers to tens of micrometers. A high resolution high angle annular dark field (HAADF) scanning TEM image of the Au/$SnO_2$ interface from a typical nanowire is displayed in Figure 6.13 showing the [101] growth direction typical for these wires. X-ray diffraction (XRD) patterns from both pure and In doped $SnO_2$ wires are also shown in Figure 6.13, and in both cases can be indexed to the rutile phase of $SnO_2$.

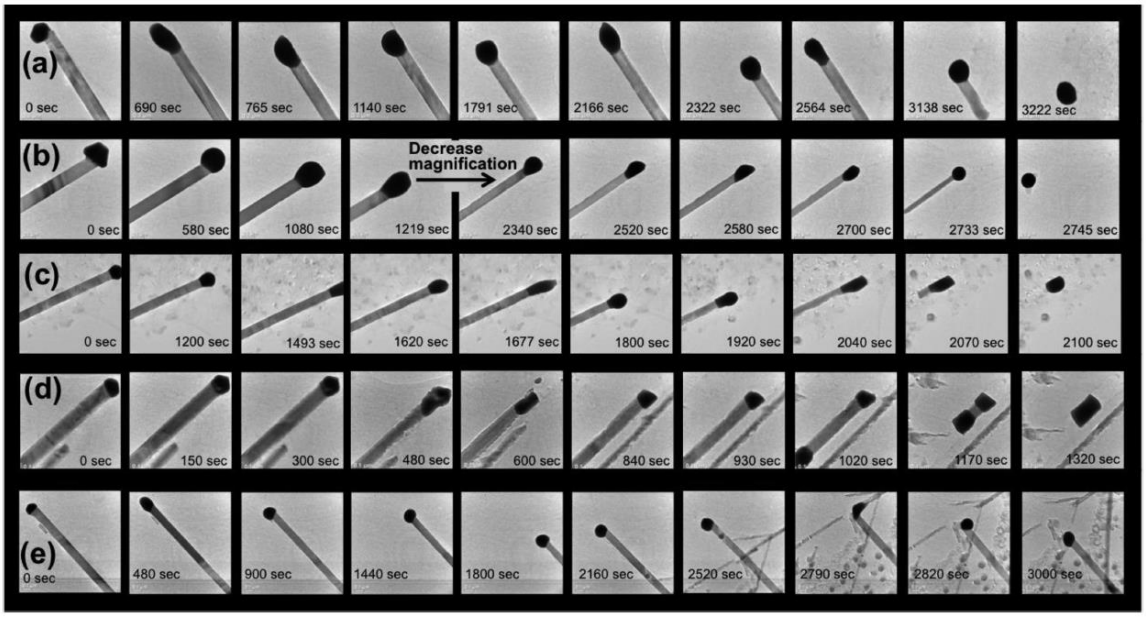


**Figure 6.12** Representative frames from five movies of nanowire heating experiments. (a) A pure $SnO_2$ nanowire is seen to dissolve into the gold catalyst particle at its head. Field of view is 1.13 μm. (b) A pure $SnO_2$ nanowire dissolves into the gold catalyst while the diameter of the wire simultaneously decreases. Field of view is 870 nm, and then increases to 1.10 μm when the magnification decreases. (c) An In-doped $SnO_2$ wire is seen to dissolve into the gold particle at its head. Field of view is 870 nm. (d) An In-doped $SnO_2$ nanowire is seen to dissolve simultaneously into gold particles at either end of the wire. Field of view is 730 nm. (e) An In-doped $SnO_2$ nanowire dissolves into the gold catalyst, and starts to change direction part way. Field of view is 1.10 μm.

To investigate the behavior of our wires at elevated temperature, we imaged individual VLS-grown wires deposited on a heating substrate (Protochips E-chip) and heated to temperatures in the in situ holder in the range of 400-800 $^{o}$C, such that etching was observed. Shown in Figure 6.12 are representative frames from movies taken from five different wires within the $SnO_2$-$In_2O_3$ solid solution. At temperatures greater than 450 $^{o}$C, the gold catalyst particle is seen to consume the entire length of these rutile-type nanowires, with what appears to be a reverse of the standard VLS mechanism. In every wire studied, dissolution of the wire is preceded by a loss of faceting in the gold catalyst head, indicating that melting of the tip is a necessary first step. This is especially apparent

in the first two panels of Figure 6.12b. The subsequent motion of the tip also suggests a fluid-like behavior. In Figure 6.12a, the gold catalyst particle migrates down the entire length of a pure-$SnO_2$ nanowire, consuming the wire over the space of ~54 min, until a stationary, isolated nanoparticle remains. In Figure 6.12b, the catalyst particle again consumes the entire length of a pure- $SnO_2$ nanowire, accompanied in this case by a simultaneous reduction in wire diameter. Similar observations were recorded for In-doped $SnO_2$ nanowires, and are shown in Figure 6.12c-e, demonstrating that this phenomenon is generally applicable into the solid solution. Figure 6.12c shows an In-doped $SnO_2$ wire in which a mechanism similar to that of Figure 6.12a is observed; the nanoparticle migrates the length of the wire resulting in a stationary, isolated nanoparticle. Figure 6.12d shows the effect of putting a wire in contact with multiple gold particles; toward the end of the recording, a second catalyst particle appears in the bottom of the screen, and the two pieces of gold consume the wire simultaneously from opposite ends, finally agglomerating into a single stationary nanoparticle. In Figure 6.12e, the particle encounters a junction of crossed wires and has the option of continuing along the initial wire or switching to a different wire; after proceeding a short distance into the new wire it switches back to the initial path until reaching a final stop. The TEM heating substrates used (Protochips Aduro platform) are composed of a thick ceramic which acts as the heater, containing a regular array of 7-µm-diameter holes and a carbon support film overlay. Due to the thickness of the ceramic, high quality TEM images are attainable only on those areas of carbon overlaying a hole in the ceramic. For this reason, should the catalyst particle migrate over the edge of a hole onto the ceramic heater, the experiment was terminated, as occurs in Figure 6.12e last panel.

The rate of the reverse VLS mechanism was controlled by varying the temperature, using higher temperatures to increase the rate at which the catalyst particle migrates the length of the wire, and removing the heat to effectively and instantaneously prevent further motion of the particle. This ability to repeatedly quench and restart the wire dissolution process was utilized to collect compositional data at intervals during the experiment, by performing energy dispersive X-ray spectroscopy (EDS) on the gold catalyst particle. EDS spectra were collected intermittently by periodically quenching the system to room temperature to stop the motion of the nanoparticle and collect the spectrum, subsequently returning to the original experimental temperature once a spectrum had been collected. To compare multiple sets of data, we performed systematic EDS collection from pure $SnO_2$ nanowires using a standard procedure, ramping the temperature at 2 $^{o}$C/s from room temperature until 700 $^{o}$C, holding the wire at 700 $^{o}$C during dissolution, and quenching and taking spectra at intervals of 8.5 min. Figure 6.14 shows EDS spectra acquired from two wires using this procedure. The Sn Lα and Lβ peaks at 3.4 and 3.6 keV and the Au Mα peak at 2.1 keV were fit to Voigt functions, and the area under the curve was found for each peak in each spectrum. Frames from the movies of the two wires taken between EDS collection times are shown in Figure 6.14a, b. Plotted in Figure 6.14c, d are the relative ratios of the integrated intensity of the Sn and Au peaks at each time during the EDS data collection.

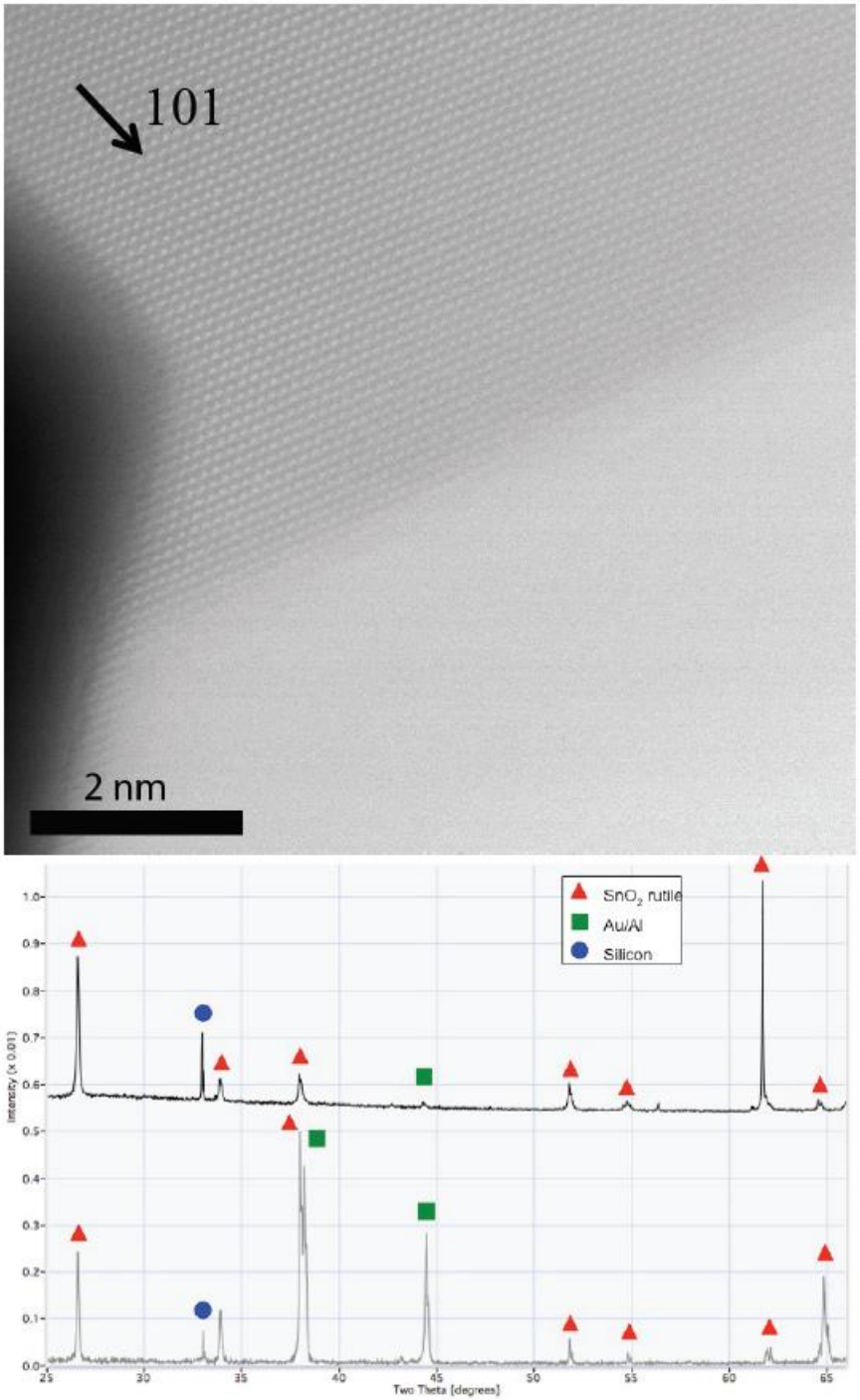


**Figure 6.13** $SnO_2$ nanowire characterization. **(a)** High resolution Z-contrast STEM image of the droplet-nanowire interface. Arrow indicates the [101] growth direction. **(b)** XRD patterns from as-grown samples of $SnO_2$ (bottom) and In-doped $SnO_2$ (top) nanowires, indexed to rutile. Al and Si peaks are present due to the stage and substrate.

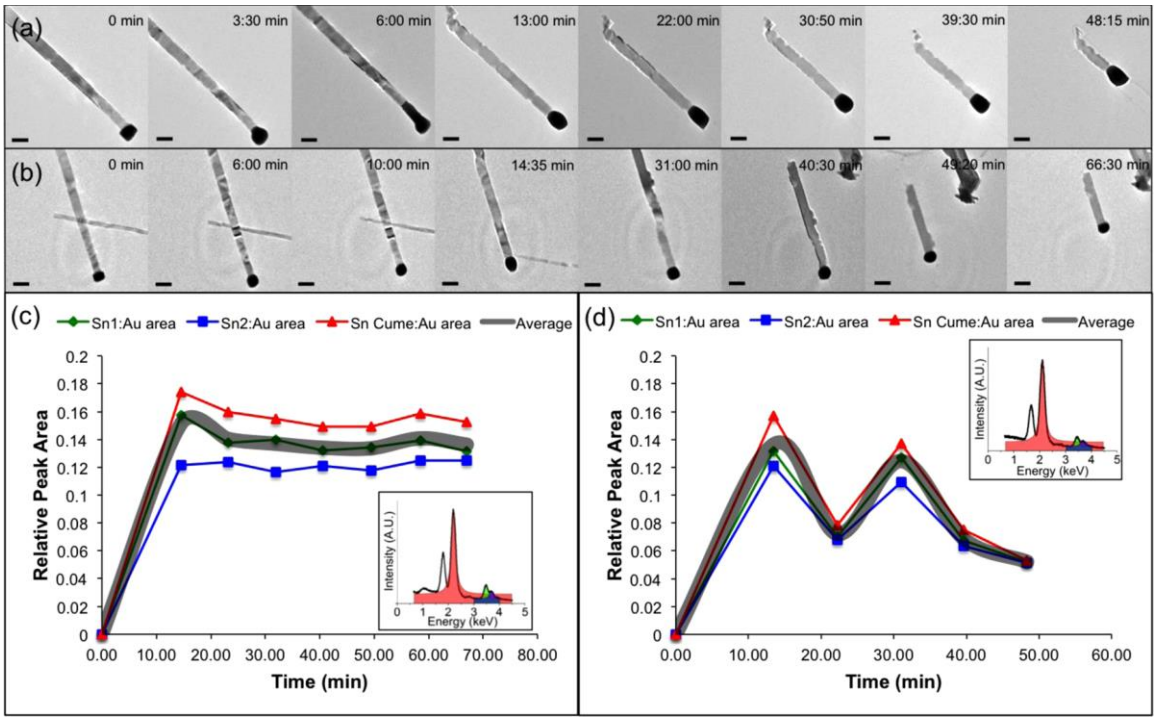


**Figure 6.14** In situ compositional analysis of two SnO2 nanowires. (a and b) Images extracted from movies of nanowire heating. Scale bars are 100 nm. (c and d) Relative EDS peak areas as a function of time taken from wires (a and b), respectively. Insets: Representative EDS spectra. Shaded regions indicate integrated area from Voigt fitting. Gold peak is shaded in red, Sn1 in green, and Sn2 in blue. The peak at 1.7 keV is Si from the substrate. Wires were heated to 700 $^{o}$C and quenched in 8.5 min intervals to stop droplet movement and acquire EDS spectra.

Initially, before heating, no Sn is detected in the catalyst particle at the wire head. After several minutes of nanoparticle migration, however, Sn Lα and Lβ peaks appear indicating the presence of Sn in the metal tip. After the initial spike in Sn concentration, the ratio of Sn/Au falls, and though fluctuating throughout the remainder of the experiment, it appears to reach a relatively steady state. Though qualitative in nature, these observations show that the steps of the VLS mechanism appear to be occurring in reverse. First, the Au droplet melts, at a temperature much closer to the Sn-Au liquidus temperature of 483 $^{o}$C than that of bulk gold (1084 $^{o}$C),[201] implying an initial diffusion of Sn into the Au droplet to form an alloy. Next, the $SnO_2$ dissolves in the droplet causing a

spike in the Sn/Au ratio in an incorporation step, which is the reverse of the initial crystallization. Finally, the Au-Sn alloy reaches a supersaturation and Sn is ejected from the droplet, presumably by evaporation, although some surface diffusion cannot be ruled out. One additional step in this SLV type process is that in order for the droplet to continue to incorporate Sn, so that the dissolution and evaporation steps may retain a steady state, it must overcome adhesion to the substrate surface so that it is mobile. These mechanistic steps are indicated schematically in Figure 6.15.

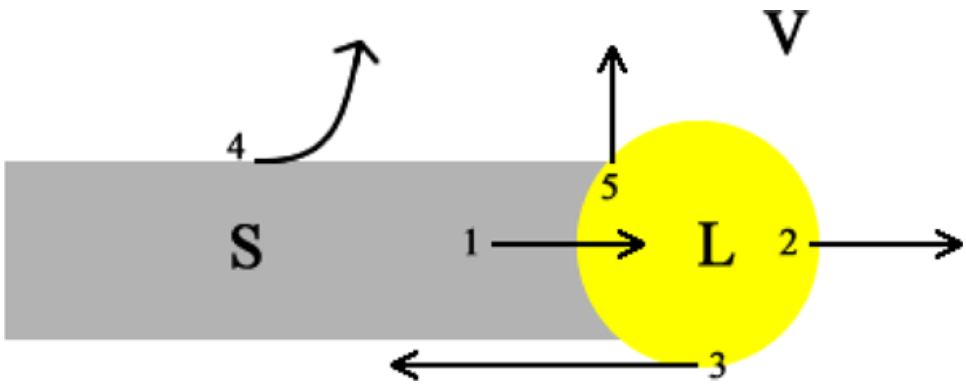


**Figure 6.15** Cartoon depicting the five processes taking place during SLV dissolution of the nanowire: (1) $SnO_2$ dissolves into Au droplet at SL interface. (2) Sn is ejected at the LV interface. (3) Adhesion between droplet and substrate is overcome so that the dissolution and ejection steps can maintain a steady state. (4) $SnO_2$ vaporization from nanowire sidewall (SV interface). (5) Possible evaporation of O at the SLV triple junction.

Though EDS clearly shows that the Sn dissolves from the wire into the droplet and is ejected, it is not clear from EDS whether the oxygen content of the wire is lost entirely at the liquid-vapor interface, or if dissociative dissolution of $SnO_2$ to SnO and O (as would be expected) occurs at the solid-liquid interface, allowing some oxygen to evaporate at the triple junction, since the spectrometer used for in situ EDS collection did not have sufficient resolution to resolve the oxygen peak.

To measure the pressure dependence of the $SnO_2$ dissolution, we conducted a series of annealing experiments (Figure 6.16 table) in which we annealed as-grown scanning electron microscope (SEM) substrates in a CVD furnace, to control the atmosphere and pressure between 2 and 500 Torr, which is representative of the entire pressure range available to us with controlled atmosphere. Oxygen mole fraction was varied between 0 and 1, with the remaining pressure exerted by Ar. For each annealing experiment, 100 sccm of gas was used in total. On annealing with the minimum total pressure and minimum oxygen partial pressure (2 Torr and 0, respectively) at 700 $^{o}$C, no change in the wire appearance was observable under SEM (Figure 6.16 a). Increasing the temperature to 900 $^{o}$C also saw no change, but degradation to the wires was observed at 1000 $^{o}$C, with noticeably fewer wires present, and those remaining having no observable catalyst tip (Figure 6.16b). Performing the same experiment but with greater mole fractions of oxygen also led to the same level of wire degradation, suggesting that total pressure, rather than oxygen partial pressure, is more dominant in the vaporization of $SnO_2$. Two further experiments were conducted at atmospheric pressure, annealing a TEM Protochips substrate with $SnO_2$ nanowires deposited upon it. In these experiments, annealing in atmospheric oxygen resulted in no observable change, but a slight degradation of the wires can be observed after annealing in an oxygen-free environment. In these experiments, the catalyst tip is still observable, but the wire morphology is no longer perfectly straight. While definitive conclusions would require us to be able to control the atmosphere while tuning the pressure between the 2 Torr available to us using the CVD furnace, and the $10^{-6}$ Torr of the TEM column, it is clear from these results that Au-catalyzed dissolution of the wires is highly dependent on pressure, requiring low

pressure for the reproducible dissolution of entire wires. We speculate that the slight dependence of wire degradation on oxygen partial pressure is indicative of a secondary, much slower, vaporization directly from the nanowire sidewalls. This conclusion is consistent with the findings of Klamchuen et al., who found that a dependence of $SnO_2$ nanowire growth on oxygen partial pressure was indicative of competing mechanisms at the SV and LV interfaces.[202]

| $P_{total}$ (Torr) | $X_{Oxygen}$ | T (°C) | T (min) | Results |
|---|---|---|---|---|
| 2 | 0 | 700 | 30 | No change |
| 2 | 0 | 900 | 30 | No change |
| 2 | 0 | 1000 | 30 | Degradation |
| 2 | 0.67 | 1000 | 30 | Degradation |
| 2 | 1 | 1000 | 30 | Degradation |
| 500 | 1 | 700 | 30 | No change |
| 760 | 0 | 700 | 60 | Small degradation |
| 760 | 0.22 | 700 | 60 | No change |

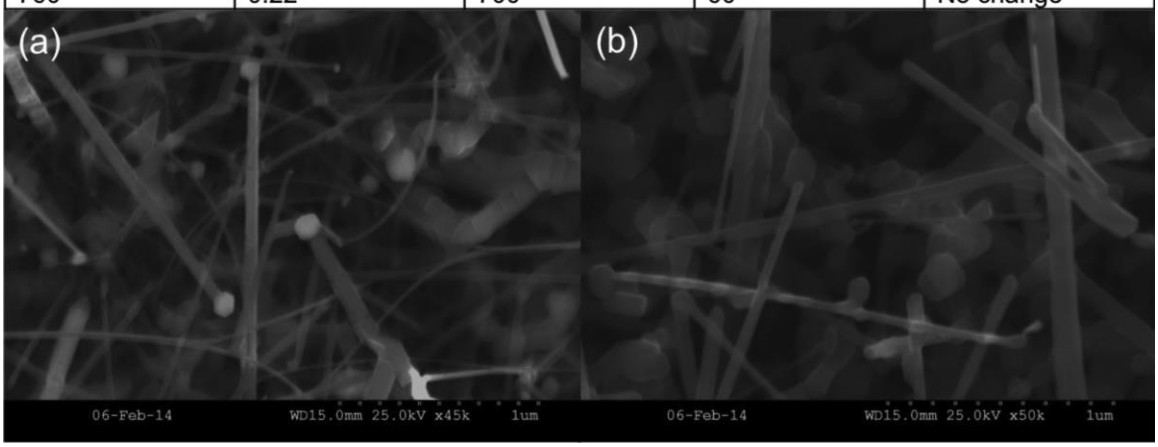


**Figure 6.16** Pressure dependence of $SnO_2$ nanowire dissolution. Table: parameters used for annealing experiments. (a) $SnO_2$ as-grown nanowires imaged by SEM; (b) $SnO_2$ nanowires annealed at $P_{total}$ = 2 Torr, $X_{oxygen}$ = 1, T = 1000 ºC. Gold droplets are no longer present and density of wires is reduced, indicating wire degradation.

## Conclusions

In conclusion, the combination of kinetic studies showing the correlation of $T_{move}$ with catalyst droplet area and dissolution rate with droplet volume, the observed lack of dependence of dissolution rate on wire diameter, and the low pressures necessary for observable wire dissolution allow us to consistently explain our observations in terms of SLV dissolution of our nanowires, dependent on two crucial steps: (1) the ability of the catalyst droplet to overcome adhesion to the substrate, such that a steady state may be reached between Sn incorporation and ejection, and (2) the evaporation of the wire from the LV interface. The method outlined herein should provide an experimental platform to explore several features relevant to the VLS growth mechanism, such as the saturation concentration of a reactant within a VLS catalyst droplet and the use of VLS catalyst metals for the controlled etching of semiconducting materials.

## 6.5 Characterization methods

Current characterization methods utilized to investigate the plasmonic functionality of materials can be roughly grouped into two categories. The first category uses an electromagnetic probe to detect the optically active (bright) modes. The second category uses an electron probe to excite and detect all of the LSPR modes, including the so-called dark modes of plasmonic materials.

UV/vis is an inexpensive and convenient technique that provides important LSPR information from an ensemble of plasmonic particles in solution, based on the particle size, dielectric medium and chemical surroundings. This spectroscopic technique monitors bulk solutions,[138,139] in which the excitation of individual LSPRs leads to a small perturbation of the measured signal, resulting in to too low of a signal to noise ratio to detect individual nanoparticles. Instead, resonant Rayleigh scattering spectroscopy is the most straightforward technique to characterize the LSPR spectrum of individual noble-metal nanoparticles, providing a high signal to noise ratio, since this is a dark field technique in which only the scattered signal is detected in the presence of very low background.[139] Improved spatial resolution was demonstrated by Klar et al., who utilized a tunable laser source equipped on a near-field scanning optical microscope (NSOM) to measure the scattering spectra of individual metallic nanoparticles.[140] In this case the resolution is limited by the size of the detector rather than the wavelength of light,[141,142] although this experimental setup is prohibitively expensive for most routine characterization.

There are two main ways in which an electron-beam may be used as a probe for plasmonic characterization: energy filtered transmission electron microscopy (EFTEM)

and electron energy loss spectroscopy (EELS); both techniques function under the same principles except that EFTEM is performed in a conventional TEM whereas EELS is performed in a STEM.[143-147] In EFTEM, by applying a magnetic field to transmitted electrons, the flight path of electrons will be different depending on the kinetic energy of the electrons. An energy filter only allows a certain defined energy range of electrons to be collected to generate images from that desired energy range. In EELS a spectrum from the full energy range is collected from each pixel in a two-dimensional image. The end result from both techniques, therefore, is a "data cube" in which an intensity is recorded for each value of x, y and energy. An advantage of EELS is that an annular dark field (ADF), or "Z-contrast" image can be taken simultaneously while collecting the spectroscopic data.[148,149] On the other hand, high spatial resolution is achieved by parallel measurement of all spatial channels in EFTEM, and the energy resolution can be improved to sub-eV range with a small energy-filtering slit width.[149,150]

In this report we will describe the development of EELS mapping to spatially resolve the plasmon modes of our new plasmonic materials.

## 6.6 STEM-EELS mapping

### 6.6.1 Methods

The experiments were performed with a Zeiss Libra 200 MC transmission electron microscope which is equipped with a Zeiss proprietary electron gun monochromator (MC) and Kohler illumination system. The monochromator enables the operator to reduce the energy resolution to less than 0.2 eV in EELS. The acceleration voltage is between 60-200 keV. The Au in hexaniobate (Au @ HNB) peapod nano-structures were

pre-made using Solvothermal method, the details are discussed in section 2.1.4. TEM samples were made using dropcasting method. Before samples insertion, the TEM samples were heated at 60 $^{O}$C on a heat plate for 30 minutes to remove possible contaminates. After sample insertion, careful alignments are performed for best image quality (both in bright and dark field) and energy resolution.

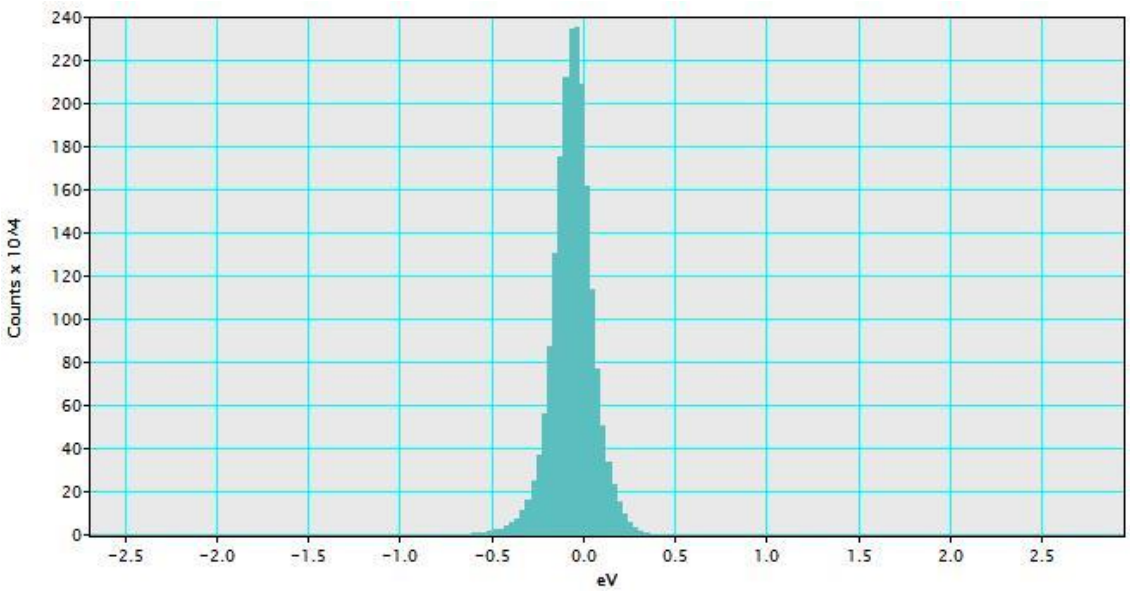


**Figure 6.17** The zero loss peak (ZLP) in EELS. The full width at half maximum (FWHM) is measured to be 0.2 eV which is also known as the energy resolution.

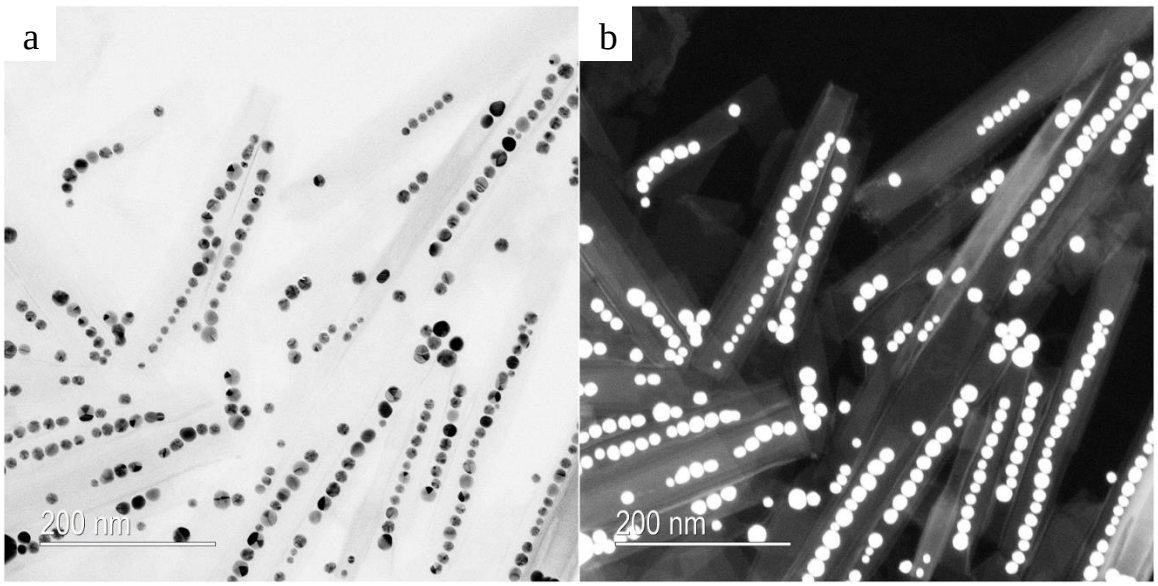


**Figure 6.18** TEM images in both (a) bright field and (b) dark field showing Au in Hexaniobte nano-peapod structures.

In Figure 6.17, an EELS spectrum at lower energy range was taken, showing the zero loss peak (ZLP) with an energy resolution of 0.2 eV under optimal conditions. In Figure 6.18, both bright and dark field TEM images are presented, showing high quality Au in Hexaniobate nano-peapod structures.

### *6.6.2 Plasmon mapping results for Au @ HNB nanowires*

Under STEM mode, certain region of interests (ROI) are assigned and EELS mappings are performed. As discussed in pervious sections, we are trying to map the localized surface plasmon resonance (LSPR) behaviors in this nano-peapod system, and we are expecting to see the coupling of LSPR between metal nanoparticles. The coupling LSPR normally results in different plasmon modes. As we use electron beam as a probe in EELS, all the LSPR modes are activated. In this section, two selected sets of data are presented.

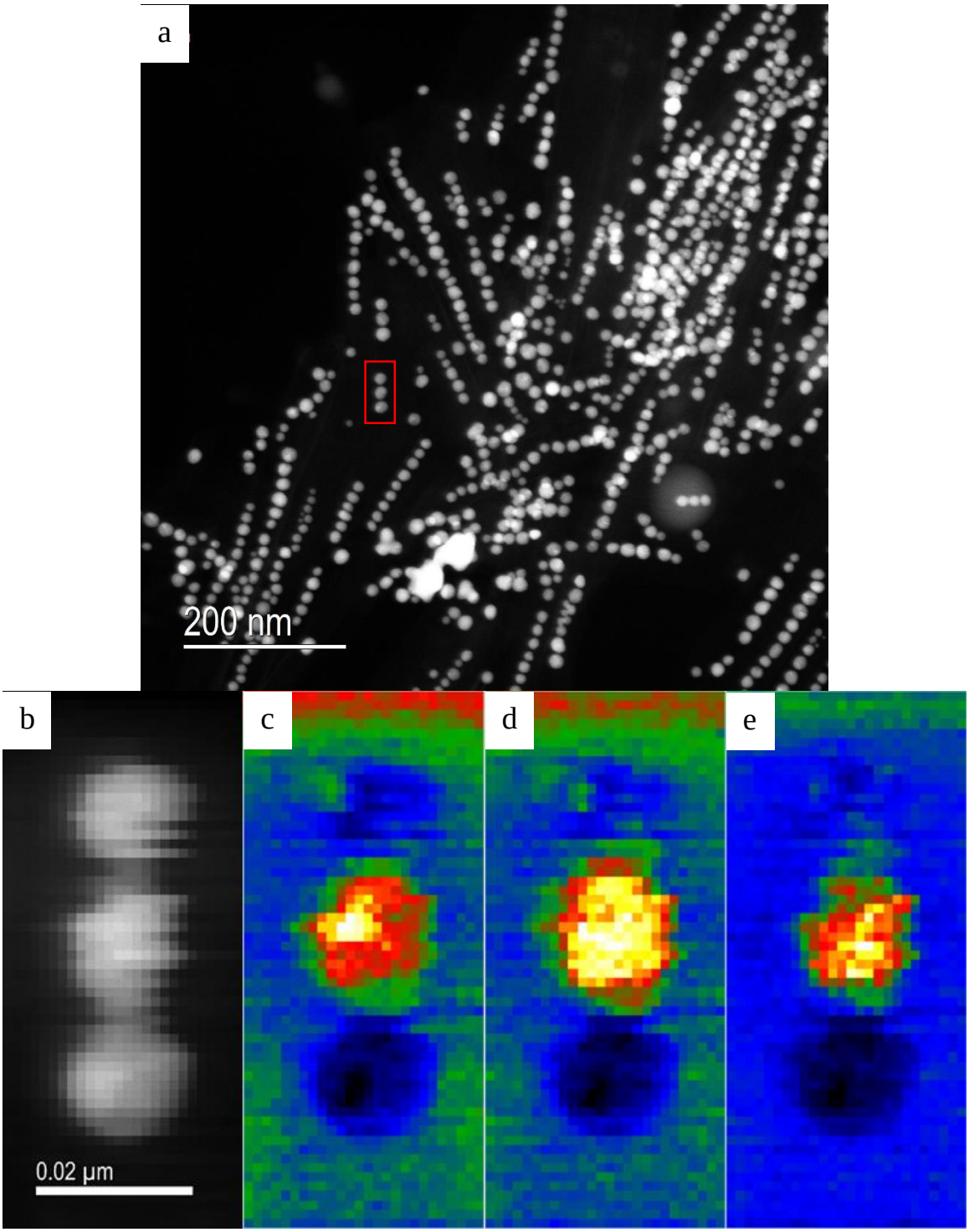


**Figure 6.19** (a) Dark field image with a red box assigned as ROI. (b) Showing the ROI in pixels. Figure (c,d,e) are EELS maps showing energy center at 0.620, 0.840 and 1.165 eV respectively with an energy resolution of 0.265 eV.

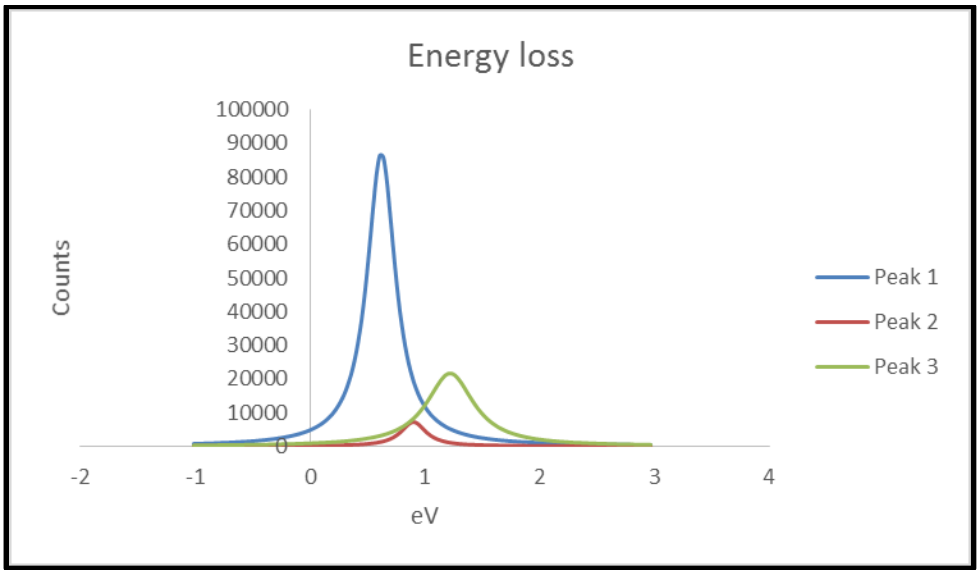


**Figure 6.20** Peak deconvolution at the tail of ZLP. Peak 1, 2 and 3 correspond to EELS maps in Figure 6.19 (a, b and c).

In this set of data, three Au nanoparticles chain with similar shape, size and spacing are assigned as ROI, and STEM-EELS plasmon mapping are performed. The results are presented in Figure 6.19 and 6.20. Figure 6.19 (a) is a dark field image shows the area where the EELS map was taken. The mapped area is shown in pixels is presented in Figure 6.19 (b). Three EELS maps are presented in Figure 6.19 (c, d and e) showing three different energy center at 0.620, 0.840 and 1.165 respectively. The maps show interesting results because all the plasmon behaviors seem to be focused on the second Au nanoparticle. Figure 6.20 is plotted after the deconvolution at the tail of ZLP, these three peaks exactly matched the energy range of Figure 6.19 (c, d and e). The X-axis represents the energy loss of the primary electron, as the energy may loss due to inelastic scattering when interacting with sample. The inelastic energy loss is exactly how much energy absorbed by the sample to activate different plasmon modes.

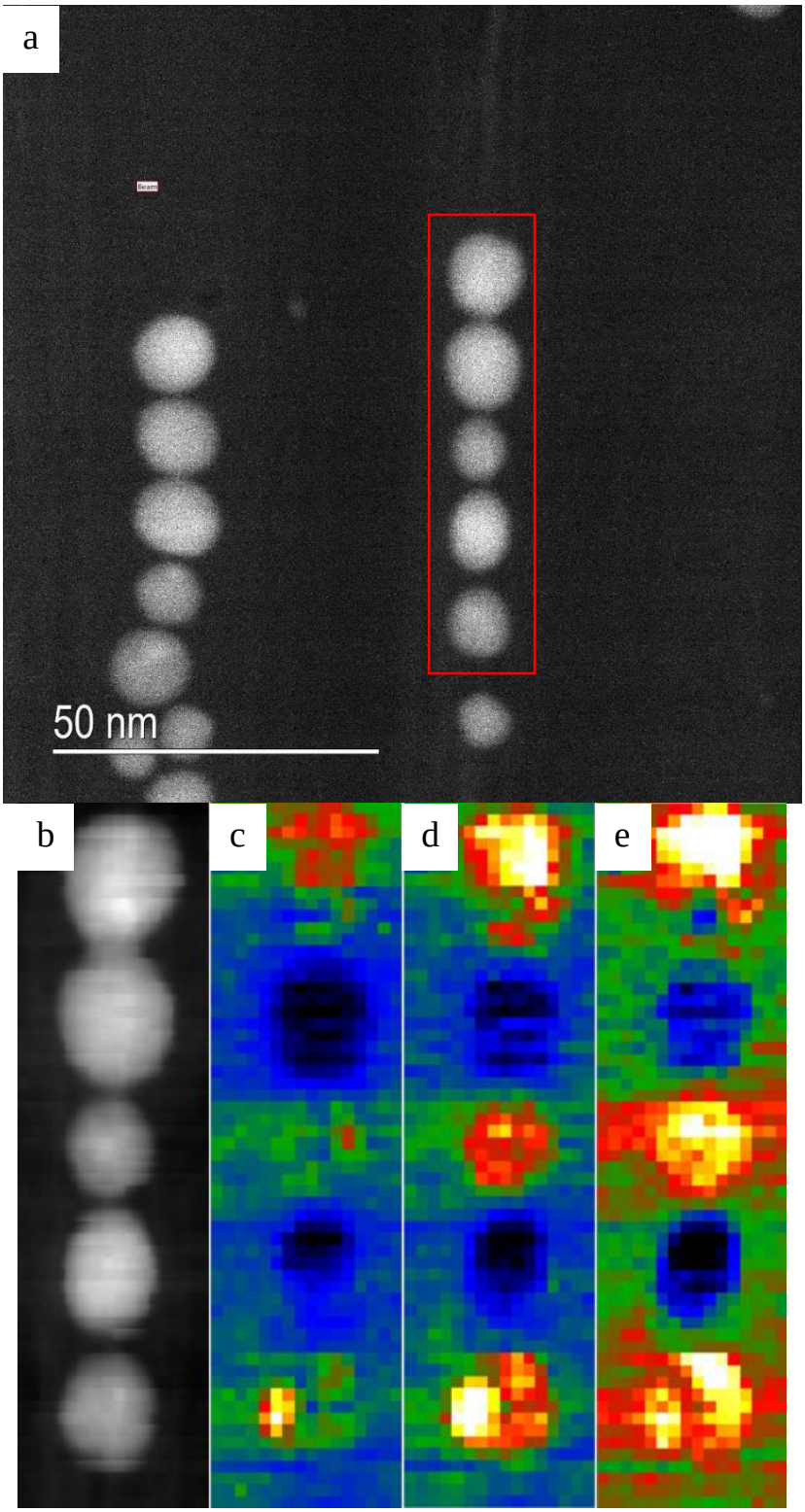


**Figure 6.21** (a) Dark field image with a red box assigned as ROI. (b) Showing the ROI in pixels. Figure (c,d,e) are EELS maps showing energy center at 0.649, 0.943 and 1.474 eV respectively with an energy resolution of 0.324 eV.

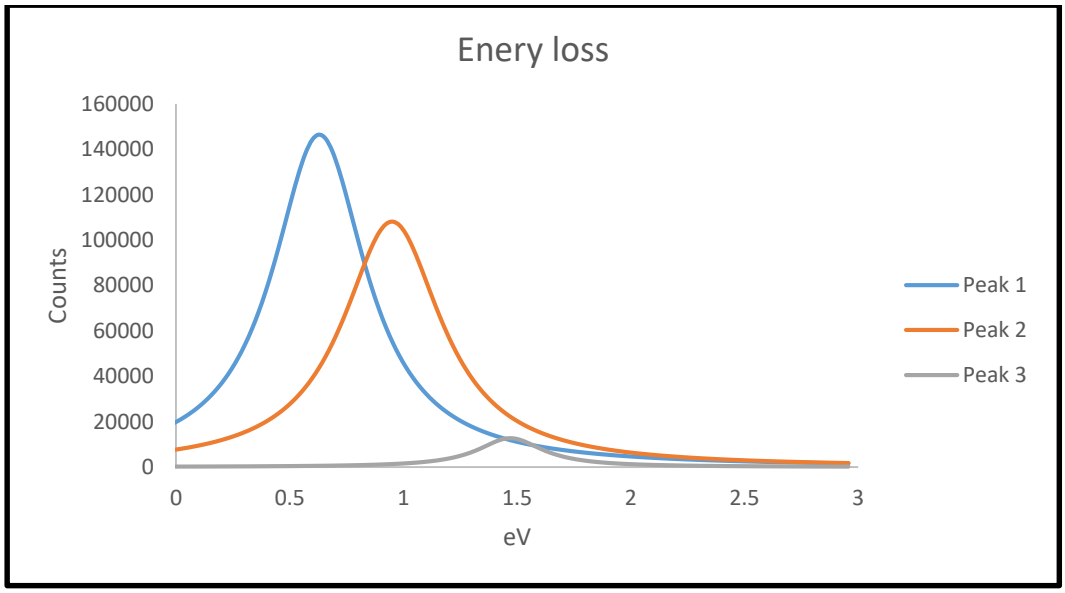


**Figure 6.22** Peak deconvolution at the tail of ZLP. Peak 1, 2 and 3 correspond to EELS maps in Figure 6.21 (a, b and c).

In the second set of data, a five-particle Au nanoparticle chain are assigned as ROI. The results are presented in Figure 6.21 and 6.22. Figure 6.21(a and b) are dark field image and ROI in pixels respectively. Figure 6.21(c, d and e) are EELS maps showing energy center at 0.649, 0.943 and 1.474 eV with an energy resolution of 0.324 eV. The deconvolution results at the tail of ZLP are shown in Figure 6.22. Peak 1, 2 and 3 correspond to Figure 6.21 (c, d and e) respectively. In Figure 6.21 (c), most of the plasmon activity focused on the first and fifth particle. In Figure 6.21 (d and e), plasmon activities localized in the first, third and fifth particle. There's no plasmon activity discovered in the second and forth particles in any energy range.

### 6.7 Conclusions

Based on the observation of the two sets of data presented in previous section, it is clearly suggesting that the LSPR on each Au particles are coupling and forming new plasmon modes. The LSPR activities would be observed on each Au nanoparticles if they are not coupled. The EELS maps show clear evidence that at certain energy ranges,

plasmon activities are localized on particular particles which differs from LSPR on individual particles. As the results confirmed, the STEM-EELS is a powerful technique on mapping plasmon behaviors. The results revealed not only the coupled plasmon modes but also the precise corresponding energies. More importantly, the standing wave characteristics of the surface plasmon have been discussed in the literature,[207,208] and can be revealed in the EELS maps.

## Chapter 7: Conclusions

In summary, this dissertation provides an overview of electron microscopy, solid-state nanomaterials synthesis, and plasmonic materials. The principle, background, and associated techniques of electron microscopy are discussed in details in early chapters. Different case studies in later chapters have demonstrated how powerful electron microscopy methods are to analyze the relationships between nanostructures and their advanced properties. Using vapor-liquid-solid synthesis methods in a chemical vapor deposition system to make different composition of metal oxide nanowires are also discussed, which includes a derived case study of reverse VLS. These case studies are great examples of using advanced electron microscopy techniques to approach nanomaterials and their characteristics.

With the newly developed *in situ* liquid cell TEM holders, a small amount of liquid sample can be inserted into the TEM without damaging the vacuum system. The tip of the liquid cell holder was composed by two pieces of silicon microchips superimposed and the little space in between can be considered as a reaction chamber. The solution is sealed between silicon nitride membranes coated on the surface of the microchips; with the etching windows on the microchips the electron beam is able to pass through the reaction chamber and observe the ongoing reactions in the solution. *In situ* observations of the assembly processes have been recorded in real time videos and the results are consistent with the initial hypothesis of LSPR induced Au nanorods tip-to-tip self-alignment.

STEM-EELS technique is another advanced technique that has been fully discussed in this dissertation. By measuring the energy loss of inelastically scattered primary

electrons, we are able to map light elements dopant distributions, study the valence states of transition metals, and map LSPR activities in nano-peapod systems.

Overall, this dissertation provides detail information of using advanced electron microscopy characterization techniques to study nanomaterials in order to improve synthesis methods, and furthermore, to control and design new nanostructures with the desired chemical and physical properties.

## References


(1) Adams, D. M.; Brus, L.; Chidsey, C. E. D.; Creager, S.; Creutz, C.; Kagan, C. R.; Kamat, P. V.; Lieberman, M.; Lindsay, S.; Marcus, R. A.; Metzger, R. M.; Michel-Beyerle, M. E.; Miller, J. R.; Newton, M. D.; Rolison, D. R.; Sankey, O.; Schanze, K. S.; Yardley, J.; Zhu, X. Charge Transfer on the Nanoscale: Current Status. *The Journal of Physical Chemistry B* **2003**, *107*, 6668-6697.

(2) Alivisatos, A. P. Semiconductor Clusters, Nanocrystals, and Quantum Dots. *Science* **1996**, *271*, 933-937.

(3) Brus, L. Electronic wave functions in semiconductor clusters: experiment and theory. *The Journal of Physical Chemistry* **1986**, *90*, 2555-2560.

(4) Iijima, S. Helical microtubules of graphitic carbon. *Nature* **1991**, *354*, 56-58.

(5) Murray, C. B.; Norris, D. J.; Bawendi, M. G. Synthesis and characterization of nearly monodisperse CdE (E = sulfur, selenium, tellurium) semiconductor nanocrystallites. *Journal of the American Chemical Society* **1993**, *115*, 8706-8715.

(6) Novoselov, K. S.; Geim, A. K.; Morozov, S. V.; Jiang, D.; Zhang, Y.; Dubonos, S. V.; Grigorieva, I. V.; Firsov, A. A. Electric Field Effect in Atomically Thin Carbon Films. *Science* **2004**, *306*, 666-669.

(7) Li, T.; Goldberger, J. E. Atomic-Scale Derivatives of Solid-State Materials. *Chemistry of Materials* **2015**, *27*, 3549-3559.

(8) Requejo-Isidro, J.; del Coso, R.; Solis, J.; Gonzalo, J.; Afonso, C. N. Role of surface-to-volume ratio of metal nanoparticles in optical properties of Cu:Al2O3 nanocomposite films. *Applied Physics Letters* **2005**, *86*, 193104.

(9) Butler, S. Z.; Hollen, S. M.; Cao, L.; Cui, Y.; Gupta, J. A.; Gutiérrez, H. R.; Heinz, T. F.; Hong, S. S.; Huang, J.; Ismach, A. F.; Johnston-Halperin, E.; Kuno, M.; Plashnitsa, V. V.; Robinson, R. D.; Ruoff, R. S.; Salahuddin, S.; Shan, J.; Shi, L.; Spencer, M. G.; Terrones, M.; Windl, W.; Goldberger, J. E. Progress, Challenges, and Opportunities in Two-Dimensional Materials Beyond Graphene. *ACS Nano* **2013**, *7*, 2898-2926.

(10) Ferrari, A. C.; Meyer, J. C.; Scardaci, V.; Casiraghi, C.; Lazzeri, M.; Mauri, F.; Piscanec, S.; Jiang, D.; Novoselov, K. S.; Roth, S.; Geim, A. K. Raman Spectrum of Graphene and Graphene Layers. *Physical Review Letters* **2006**, *97*, 187401.

(11) Kim, K. S.; Zhao, Y.; Jang, H.; Lee, S. Y.; Kim, J. M.; Kim, K. S.; Ahn, J.-H.; Kim, P.; Choi, J.-Y.; Hong, B. H. Large-scale pattern growth of graphene films for stretchable transparent electrodes. *Nature* **2009**, *457*, 706-710.

(12) Lee, C.; Wei, X.; Kysar, J. W.; Hone, J. Measurement of the Elastic Properties and Intrinsic Strength of Monolayer Graphene. *Science* **2008**, *321*, 385-388.

(13) Li, D.; Muller, M. B.; Gilje, S.; Kaner, R. B.; Wallace, G. G. Processable aqueous dispersions of graphene nanosheets. *Nat Nano* **2008**, *3*, 101-105.

(14) Erni, R.; Rossell, M. D.; Kisielowski, C.; Dahmen, U. Atomic-Resolution Imaging with a Sub-50-pm Electron Probe. *Physical Review Letters* **2009**, *102*, 096101.

(15) O'Keefe, M. A.; Allard, L. F.: *Sub-Angstrom electron microscopy for sub-Angstrom nano-metrology*; ; Ernest Orlando Lawrence Berkeley National Laboratory, Berkeley, CA (US), 2004.

(16) Bogner, A.; Jouneau, P. H.; Thollet, G.; Basset, D.; Gauthier, C. A history of scanning electron microscopy developments: Towards “wet-STEM” imaging. *Micron* **2007**, *38*, 390-401.
(17) Guiton, B. S.; Iberi, V.; Li, S. Z.; Leonard, D. N.; Parish, C. M.; Kotula, P. G.; Varela, M.; Schatz, G. C.; Pennycook, S. J.; Camden, J. P. Correlated Optical Measurements and Plasmon Mapping of Silver Nanorods. *Nano Letters* **2011**, *11*, 3482-3488.
(18) Pennycook, S. J.; Lupini, A. R.; Kadavanich, A.; McBride, J. R.; Rosenthal, S. J.; Puetter, R. C.; Yahil, A.; Krivanek, O. L.; Dellby, N.; Nellist, P. D. L.; Duscher, G.; Wang, L. G.; Pantelides, S. T.: Aberration-corrected scanning transmission electron microscopy: the potential for nano- and interface science. *Z Metallkd* **2003**, *94*, 350-357.
(19) Jesson, D. E.; Pennycook, S. J.: Incoherent Imaging of Crystals Using Thermally Scattered Electrons. *P R Soc-Math Phys Sc* **1995**, *449*, 273-293.
(20) McBride, J. R.; Kippeny, T. C.; Pennycook, S. J.; Rosenthal, S. J.: Aberration-corrected Z-contrast scanning transmission electron microscopy of CdSe nanocrystals. *Nano Letters* **2004**, *4*, 1279-1283.
(21) Goldstein, J.: *Scanning electron microscopy and x-ray microanalysis*; 3rd ed.; Kluwer Academic/Plenum Publishers: New York, 2003.
(22) Serin, V.; Andrieu, S.; Serra, R.; Bonell, F.; Tiusan, C.; Calmels, L.; Varela, M.; Pennycook, S. J.; Snoeck, E.; Walls, M.; Colliex, C.: TEM and EELS measurements of interface roughness in epitaxial Fe/MgO/Fe magnetic tunnel junctions. *Phys Rev B* **2009**, *79*.
(23) Browning, N. D.; Wallis, D. J.; Nellist, P. D.; Pennycook, S. J.: EELS in the STEM: Determination of materials properties on the atomic scale. *Micron* **1997**, *28*, 333-348.
(24) Guiton, B. S.; Iberi, V.; Li, S. Z.; Leonard, D. N.; Parish, C. M.; Kotula, P. G.; Varela, M.; Schatz, G. C.; Pennycook, S. J.; Camden, J. P.: Correlated Optical Measurements and Plasmon Mapping of Silver Nanorods. *Nano Letters* **2011**, *11*, 3482-3488.
(25) Mirsaleh-Kohan, N.; Iberi, V.; Simmons, P. D.; Bigelow, N. W.; Vaschillo, A.; Rowland, M. M.; Best, M. D.; Pennycook, S. J.; Masiello, D. J.; Guiton, B. S.; Camden, J. P.: Single-Molecule Surface-Enhanced Raman Scattering: Can STEM/EELS Image Electromagnetic Hot Spots? *J Phys Chem Lett* **2012**, *3*, 2303-2309.
(26) Kotula, P. G.; Keenan, M. R.; Michael, J. R.: Automated analysis of SEM X-ray spectral images: A powerful new microanalysis tool. *Microsc Microanal* **2003**, *9*, 1-17.
(27) Smentkowski, V. S.; Ohlhausen, J. A.; Kotula, P. G.; Keenan, M. R.: Multivariate statistical analysis of time-of-flight secondary ion mass spectrometry images-looking beyond the obvious. *Applied Surface Science* **2004**, *231*, 245-249.
(28) Smentkowski, V. S.; Ostrowski, S. G.; Keenan, M. R.: A comparison of multivariate statistical analysis protocols for ToF-SIMS spectral images. *Surf Interface Anal* **2009**, *41*, 88-96.
(29) Hausler, W.: Basics of X-ray Diffraction. *Hyperfine Interactions* **2004**, *154*, 13p.

(30) Iriarte, G. F.: Using Transmission Electron Microscopy (TEM) for Chemical Analysis of Semiconductors**.** *Microscopy: Science, Technology, Applications and Education, Book Chapter* **2010**, 1888-1896.
(31) Pennycook, S. J.: Structure determination through Z-contrast microscopy. In *Advances in Imaging and Electron Physics*; Peter W. Hawkes, P. G. M. G. C., Marco, V.-A., Eds.; Elsevier, 2002; Vol. Volume 123; pp 173-206.
(32) Murphy, C. J.; Sau, T. K.; Gole, A. M.; Orendorff, C. J.; Gao, J.; Gou, L.; Hunyadi, S. E.; Li, T. Anisotropic metal nanoparticles: Synthesis, assembly, and optical applications. *J Phys Chem B* **2005**, *109*, 13857-13870.
(33) Zahran, E. M.; Bedford, N. M.; Nguyen, M. A.; Chang, Y. J.; Guiton, B. S.; Naik, R. R.; Bachas, L. G.; Knecht, M. R. Light-activated tandem catalysis driven by multicomponent nanomaterials. *J Am Chem Soc* **2014**, *136*, 32-35.
(34) Adireddy, S.; Rostamzadeh, T.; Carbo, C. E.; Wiley, J. B. Particle placement and sheet topological control in the fabrication of Ag-hexaniobate nanocomposites. *Langmuir* **2015**, *31*, 480-485.
(35) Djieutedjeu, H.; Chang, Y. J.; Woods, J.; De Long, L.; Guiton, B. S. Colloidal synthesis of $MnSb_2Se_4$: Effect of surfactant on magnetic properties. In preparation.
(36) Gu, M.; Parent, L. R.; Mehdi, B. L.; Unocic, R. R.; McDowell, M. T.; Sacci, R. L.; Xu, W.; Connell, J. G.; Xu, P.; Abellan, P.; Chen, X.; Zhang, Y.; Perea, D. E.; Evans, J. E.; Lauhon, L. J.; Zhang, J. G.; Liu, J.; Browning, N. D.; Cui, Y.; Arslan, I.; Wang, C. M. Demonstration of an electrochemical liquid cell for operando transmission electron microscopy observation of the lithiation/delithiation behavior of Si nanowire battery anodes. *Nano Lett* **2013**, *13*, 6106-6112.
(37) Zeng, Z.; Liang, W. I.; Liao, H. G.; Xin, H. L.; Chu, Y. H.; Zheng, H. Visualization of electrode-electrolyte interfaces in LiPF6/EC/DEC electrolyte for lithium ion batteries via in situ TEM. *Nano Lett* **2014**, *14*, 1745-1750.
(38) Firlar, E.; Cinar, S.; Kashyap, S.; Akinc, M.; Prozorov, T. Direct Visualization of the Hydration Layer on Alumina Nanoparticles with the Fluid Cell STEM in situ. *Sci Rep* **2015**, *5*, 9830.
(39) Mueller, C.; Harb, M.; Dwyer, J. R.; Miller, R. J. D. Nanofluidic Cells with Controlled Pathlength and Liquid Flow for Rapid, High-Resolution In Situ Imaging with Electrons. *The Journal of Physical Chemistry Letters* **2013**, *4*, 2339-2347.
(40) Unocic, R. R.; Baggetto, L.; Veith, G. M.; Aguiar, J. A.; Unocic, K. A.; Sacci, R. L.; Dudney, N. J.; More, K. L. Probing battery chemistry with liquid cell electron energy loss spectroscopy. *Chem Commun (Camb)* **2015**, *51*, 16377-16380.
(41) Egawa, M.; Ishida, T.; Jalabert, L.; Fujita, H. In-situ realtime monitoring of nanoscale gold electroplating using micro-electro-mechanical systems liquid cell operating in transmission electron microscopy. *Applied Physics Letters* **2016**, *108*, 023104.
(42) Sutter, E.; Jungjohann, K.; Bliznakov, S.; Courty, A.; Maisonhaute, E.; Tenney, S.; Sutter, P. In situ liquid-cell electron microscopy of silver-palladium galvanic replacement reactions on silver nanoparticles. *Nat Commun* **2014**, *5*, 4946.

(43) Sutter, E. A.; Sutter, P. W. Determination of redox reaction rates and orders by in situ liquid cell electron microscopy of Pd and Au solution growth. *J Am Chem Soc* **2014**, *136*, 16865-16870.
(44) Liao, H.-G.; Cui, L.; Whitelam, S.; Zheng, H. Real-Time Imaging of Pt3Fe Nanorod Growth in Solution. *Science* **2012**, *336*, 1011-1014.
(45) Ievlev, A. V.; Jesse, S.; Cochell, T. J.; Unocic, R. R.; Protopopescu, V. A.; Kalinin, S. V. Quantitative Description of Crystal Nucleation and Growth from in Situ Liquid Scanning Transmission Electron Microscopy. *ACS Nano* **2015**, *9*, 11784-11791.
(46) Parent, L. R.; Robinson, D. B.; Woehl, T. J.; Ristenpart, W. D.; Evans, J. E.; Browning, N. D.; Arslan, I. Direct in Situ Observation of Nanoparticle Synthesis in a Liquid Crystal Surfactant Template. *ACS Nano* **2012**, *6*, 3589-3596.
(47) Nielsen, M. H.; Aloni, S.; De Yoreo, J. J. In situ TEM imaging of CaCO3 nucleation reveals coexistence of direct and indirect pathways. *Science* **2014**, *345*, 1158-1162.
(48) Patterson, J. P.; Abellan, P.; Denny, M. S., Jr.; Park, C.; Browning, N. D.; Cohen, S. M.; Evans, J. E.; Gianneschi, N. C. Observing the growth of metal-organic frameworks by in situ liquid cell transmission electron microscopy. *J Am Chem Soc* **2015**, *137*, 7322-7328.
(49) Smeets, P. J. M.; Cho, K. R.; Kempen, R. G. E.; Sommerdijk, N. A. J. M.; De Yoreo, J. J. Calcium carbonate nucleation driven by ion binding in a biomimetic matrix revealed by in situ electron microscopy. *Nature Materials* **2015**, *14*, 394-399.
(50) Jungjohann, K. L.; Bliznakov, S.; Sutter, P. W.; Stach, E. A.; Sutter, E. A. In situ liquid cell electron microscopy of the solution growth of Au-Pd core-shell nanostructures. *Nano Lett* **2013**, *13*, 2964-2970.
(51) De Clercq, A.; Dachraoui, W.; Margeat, O.; Pelzer, K.; Henry, C. R.; Giorgio, S. Growth of Pt-Pd Nanoparticles Studied In Situ by HRTEM in a Liquid Cell. *J Phys Chem Lett* **2014**, *5*, 2126-2130.
(52) Park, J.; Zheng, H.; Lee, W. C.; Geissler, P. L.; Rabani, E.; Alivisatos, A. P. Direct Observation of Nanoparticle Superlattice Formation by Using Liquid Cell Transmission Electron Microscopy. *ACS Nano* **2012**, *6*, 2078-2085.
(53) Liu, Y.; Lin, X. M.; Sun, Y.; Rajh, T. In situ visualization of self-assembly of charged gold nanoparticles. *J Am Chem Soc* **2013**, *135*, 3764-3767.
(54) Yuk, J. M.; Park, J.; Ercius, P.; Kim, K.; Hellebusch, D. J.; Crommie, M. F.; Lee, J. Y.; Zettl, A.; Alivisatos, A. P. High-Resolution EM of Colloidal Nanocrystal Growth Using Graphene Liquid Cells. *Science* **2012**, *336*, 61-64.
(55) Park, J.; Elmlund, H.; Ercius, P.; Yuk, J. M.; Limmer, D. T.; Chen, Q.; Kim, K.; Han, S. H.; Weitz, D. A.; Zettl, A.; Alivisatos, A. P. 3D structure of individual nanocrystals in solution by electron microscopy. *Science* **2015**, *349*, 290-295.
(56) Chen, Q.; Smith, J. M.; Park, J.; Kim, K.; Ho, D.; Rasool, H. I.; Zettl, A.; Alivisatos, A. P. 3D motion of DNA-Au nanoconjugates in graphene liquid cell electron microscopy. *Nano Lett* **2013**, *13*, 4556-4561.
(57) Chen, Q.; Cho, H.; Manthiram, K.; Yoshida, M.; Ye, X.; Alivisatos, A. P. Interaction Potentials of Anisotropic Nanocrystals from the Trajectory Sampling

of Particle Motion usingin SituLiquid Phase Transmission Electron Microscopy. *ACS Central Science* **2015**, *1*, 33-39.
(58) Marquez, D. T.; Scaiano, J. C. Plasmon induced self-assembly of gold nanorods in polymer films. *Chem Commun (Camb)* **2015**, *51*, 1911-1913.
(59) Baral, S.; Green, A. J.; Richardson, H. H. Effect of Ions and Ionic Strength on Surface Plasmon Absorption of Single Gold Nanowires. *ACS Nano* **2016**, *10*, 6080-6089.
(60) Jackson, S. R.; McBride, J. R.; Rosenthal, S. J.; Wright, D. W. Where's the silver? Imaging trace silver coverage on the surface of gold nanorods. *J Am Chem Soc* **2014**, *136*, 5261-5263.
(61) Rysselberghe, P. V. Remarks concerning the Clausius-Mossotti Law. *The Journal of Physical Chemistry* **1931**, *36*, 1152-1155.
(62) Murphy, C. J.; Sau, T. K.; Gole, A. M.; Orendorff, C. J.; Gao, J.; Gou, L.; Hunyadi, S. E.; Li, T. Anisotropic metal nanoparticles: Synthesis, assembly, and optical applications. *J Phys Chem B* **2005**, *109*, 13857-13870.
(63) Cole-Hamilton, D. J. Homogeneous catalysis - new approaches to catalyst separation, recovery, and recycling. *Science* **2003**, *299*, 1702-1706.
(64) Corma, A.; Garcia, H.; Xamena, F. X. L. I. Engineering Metal Organic Frameworks for Heterogeneous Catalysis. *Chem Rev* **2010**, *110*, 4606-4655.
(65) Bhandari, R.; Coppage, R.; Knecht, M. R. Mimicking nature's strategies for the design of nanocatalysts. *Catal Sci Technol* **2012**, *2*, 256-266.
(66) Li, Q.; Guo, B. D.; Yu, J. G.; Ran, J. R.; Zhang, B. H.; Yan, H. J.; Gong, J. R. Highly Efficient Visible-Light-Driven Photocatalytic Hydrogen Production of CdS-Cluster-Decorated Graphene Nanosheets. *J Am Chem Soc* **2011**, *133*, 10878-10884.
(67) Gonzalez, E.; Arbiol, J.; Puntes, V. F. Carving at the Nanoscale: Sequential Galvanic Exchange and Kirkendall Growth at Room Temperature. *Science* **2011**, *334*, 1377-1380.
(68) El-Sayed, M. A. Small is different: Shape-, size-, and composition-dependent properties of some colloidal semiconductor nanocrystals. *Accounts Chem Res* **2004**, *37*, 326-333.
(69) Walter, M. G.; Warren, E. L.; McKone, J. R.; Boettcher, S. W.; Mi, Q.; Santori, E. A.; Lewis, N. S. Solar Water Splitting Cells. *Chemical Reviews* **2010**, *110*, 6446-6473.
(70) Gomes Silva, C.; Juarez, R.; Marino, T.; Molinari, R.; Garcia, H. Influence of Excitation Wavelength (UV or Visible Light) on the Photocatalytic Activity of Titania Containing Gold Nanoparticles for the Generation of Hydrogen or Oxygen from Water. *J Am Chem Soc* **2011**, *133*, 595-602.
(71) Fujishima, A.; Honda, K. Electrochemical Photolysis of Water at a Semiconductor Electrode. *Nature* **1972**, *238*, 37.
(72) Paracchino, A.; Laporte, V.; Sivula, K.; Gratzel, M.; Thimsen, E. Highly active oxide photocathode for photoelectrochemical water reduction. *Nat Mater* **2011**, *10*, 456-461.
(73) Chen, X. B.; Shen, S. H.; Guo, L. J.; Mao, S. S. Semiconductor-based Photocatalytic Hydrogen Generation. *Chem Rev* **2010**, *110*, 6503-6570.

(74) Yamada, Y.; Tsung, C. K.; Huang, W.; Huo, Z. Y.; Habas, S. E.; Soejima, T.; Aliaga, C. E.; Somorjai, G. A.; Yang, P. D. *Nat Chem* **2011**, *3*, 372.

(75) A Krzton-Maziopa; E Pomjakushina; V Pomjakushin; D Sheptyakov; D Chernyshov; Svitlyk, V.; Conder, K. The synthesis, and crystal and magnetic structure of the iron selenide $BaFe_2Se_3$ with possible superconductivity at $T_c$ = 11 K. *Journal of Physics : Condensed Matter* **2011**, *23*, 402201-402207.

(76) Hongwang Zhang; Gen Long; Da Li; Renat Sabirianov; Zeng, H. $Fe_3Se_4$ Nanostructures with Giant Coercivity Synthesized by Solution Chemistry. *Chem. Mater* **2011**, *23*, 3769-3774.

(77) Kanatzidis, M. G. The role of solid-state chemistry in the discovery of new thermoelectric materials. *Semiconductors and Semimetals*; Terry, M. T., Ed.; Elsevier, **2001**, 69, pp 51-100.

(78) Cava, R. J.; Ji, H.; Fuccillo, M. K.; Gibson, Q. D.; Hor, Y. S. Crystal Structure and Chemistry of Topological Insulators. *Journal of Materials Chemistry C* **2013**, *1*, 3176-3189.

(79) Min-Rui Gao; Yun-Fei Xu; Jun Jiang; Yu, S.-H. Nanostructured metal chalcogenides: synthesis, modification, and applications in energy conversion and storage devices. *Chemical Society Review* **2013**, *42*, 2986-3017.

(80) Olan Olvera; Pranati Sahoo; Stephanie Tarczynski; Poudeu, P. F. P. Topochemical Solid-State Reactivity: Redox-Induced Direct Structural Transformation from $CuSe_2$ to $CuInSe_2$. *Chem Mater* **2016**, *27*, 7179-7186.

(81) Poudeu, P. F.; Djieutedjeu, H.; Ranmohotti, K. G.; Makongo, J. P.; Takas, N. Geometrical Spin Frustration and Ferromagnetic Ordering in (Mn x Pb2–x) Pb2Sb4Se10. *Inorganic chemistry* **2013**, *53*, 209-220.

(82) Ranmohotti, K. G.; Djieutedjeu, H.; Lopez, J.; Page, A.; Haldolaarachchige, N.; Chi, H.; Sahoo, P.; Uher, C.; Young, D.; Poudeu, P. F. Coexistence of High-T c Ferromagnetism and n-Type Electrical Conductivity in FeBi2Se4. *Journal of the American Chemical Society* **2015**, *137*, 691-698.

(83) Ranmohotti, K. G.; Djieutedjeu, H.; Poudeu, P. F. Chemical Manipulation of Magnetic Ordering in Mn1–x Sn x Bi2Se4 Solid–Solutions. *Journal of the American Chemical Society* **2012**, *134*, 14033-14042.

(84) Olvera, A.; Shi, G.; Djieutedjeu, H.; Page, A.; Uher, C.; Kioupakis, E.; Poudeu, P. F. $Pb_7Bi_4Se_{13}$: A Lillianite Homologue with Promising Thermoelectric Properties. *Inorganic chemistry* **2014**, *54*, 746-755.

(85) Zou, R.; Zhang, Z.; Yuen, M. F.; Hu, J.; Lee, C.-S.; Zhang, W. Dendritic Heterojunction Nanowire Arrays for High-Performance Supercapacitors. *Scientific Reports* **2015**, *5*, 7862.

(86) Zhang, Z.; Wang, Q.; Zhao, C.; Min, S.; Qian, X. One-Step Hydrothermal Synthesis of 3D Petal-like Co9S8/RGO/Ni3S2 Composite on Nickel Foam for High-Performance Supercapacitors. *ACS Applied Materials & Interfaces* **2015**, *7*, 4861-4868.

(87) Xu, J.; Luan, C.-Y.; Tang, Y.-B.; Chen, X.; Zapien, J. A.; Zhang, W.-J.; Kwong, H.-L.; Meng, X.-M.; Lee, S.-T.; Lee, C.-S. Low-Temperature Synthesis of CuInSe2 Nanotube Array on Conducting Glass Substrates for Solar Cell Application. *ACS Nano* **2010**, *4*, 6064-6070.

(88) Li, L.; Coates, N.; Moses, D. Solution-Processed Inorganic Solar Cell Based on in Situ Synthesis and Film Deposition of CuInS2 Nanocrystals. *Journal of the American Chemical Society* **2010**, *132*, 22-23.
(89) Zhao, Y.; Burda, C. Development of plasmonic semiconductor nanomaterials with copper chalcogenides for a future with sustainable energy materials. *Energy & Environmental Science* **2012**, *5*, 5564-5576.
(90) Tapley, A.; Vaccarello, D.; Hedges, J.; Jia, F.; Love, D. A.; Ding, Z. Preparation and characterization of CuInS2 nanocrystals for photovoltaic materials. *Physical Chemistry Chemical Physics* **2013**, *15*, 1431-1436.
(91) Itthibenchapong, V.; Kokenyesi, R. S.; Ritenour, A. J.; Zakharov, L. N.; Boettcher, S. W.; Wager, J. F.; Keszler, D. A. Earth-abundant Cu-based chalcogenide semiconductors as photovoltaic absorbers. *Journal of Materials Chemistry C* **2013**, *1*, 657-662.
(92) Chang, J.-Y.; Wang, G.-Q.; Cheng, C.-Y.; Lin, W.-X.; Hsu, J.-C. Strategies for photoluminescence enhancement of AgInS2 quantum dots and their application as bioimaging probes. *Journal of Materials Chemistry* **2012**, *22*, 10609-10618.
(93) Burnett, J. D.; Gourdon, O.; Ranmohotti, K. G. S.; Takas, N. J.; Djieutedjeu, H.; Poudeu, P. F. P.; Aitken, J. A. Structure–property relationships along the Fe-substituted CuInS2 series: Tuning of thermoelectric and magnetic properties. *Materials Chemistry and Physics* **2014**, *147*, 17-27.
(94) Li, G.; Zhang, B.; Rao, J.; Herranz Gonzalez, D.; Blake, G. R.; de Groot, R. A.; Palstra, T. T. M. Effect of Vacancies on Magnetism, Electrical Transport, and Thermoelectric Performance of Marcasite FeSe2−δ (δ = 0.05). *Chemistry of Materials* **2015**, *27*, 8220-8229.
(95) Wang, J.-J.; Wang, Y.-Q.; Cao, F.-F.; Guo, Y.-G.; Wan, L.-J. Synthesis of Monodispersed Wurtzite Structure CuInSe2 Nanocrystals and Their Application in High-Performance Organic−Inorganic Hybrid Photodetectors. *Journal of the American Chemical Society* **2010**, *132*, 12218-12221.
(96) Shi, W.; Zhang, X.; Che, G.; Fan, W.; Liu, C. Controlled hydrothermal synthesis and magnetic properties of three-dimensional FeSe2 rod clusters and microspheres. *Chemical Engineering Journal* **2013**, *215–216*, 508-516.
(97) Bakshi, M. S. How Surfactants Control Crystal Growth of Nanomaterials. *Crystal Growth & Design* **2016**, *16*, 1104-1133.
(98) Long, G.; Zhang, H.; Li, D.; Sabirianov, R.; Zhang, Z.; Zeng, H. Magnetic anisotropy and coercivity of Fe3Se4 nanostructures. *Applied Physics Letters* **2011**, *99*, 202103.
(99) Li, S.-j.; Li, D.; Liu, W.; Zhang, Z. High Curie temperature and coercivity performance of Fe3-xCrxSe4 nanostructures. *Nanoscale* **2015**, *7*, 5395-5402.
(100) Tian, C.; Lee, C.; Kan, E.; Wu, F.; Whangbo, M.-H. Analysis of the Magnetic Structure and Ferroelectric Polarization of Monoclinic MnSb2S4 by Density Functional Theory Calculations. *Inorganic Chemistry* **2010**, *49*, 10956-10959.
(101) Djieutedjeu, H.; Makongo, J. P. A.; Rotaru, A.; Palasyuk, A.; Takas, N. J.; Zhou, X.; Ranmohotti, K. G. S.; Spinu, L.; Uher, C.; Poudeu, P. F. P. Crystal Structure, Charge Transport, and Magnetic Properties of MnSb2Se4. *European Journal of Inorganic Chemistry* **2011**, *2011*, 3969-3977.

(102) Djieutedjeu, H.; Olvera, A.; Page, A.; Uher, C.; Poudeu, P. F. P. High-Tc Ferromagnetism and Electron Transport in p-Type Fe1–xSnxSb2Se4 Semiconductors. *Inorganic Chemistry* **2015**, *54*, 10371-10379.
(103) Djieutedjeu, H.; Zhou, X.; Chi, H.; Haldolaarachchige, N.; Ranmohotti, K. G. S.; Uher, C.; Young, D.; Poudeu, P. F. P. Donor and acceptor impurity-driven switching of magnetic ordering in MnSb2-xSnxSe4. *Journal of Materials Chemistry C* **2014**, *2*, 6199-6210.
(104) Li, S.; Zhao, H.; Zhang, H.; Ren, G.; Liu, N.; Li, D.; Yang, C.; Jin, S.; Shang, D.; Wang, W.; Lin, Y.; Gu, L.; Chen, X. Enhancement of the thermoelectric properties of MnSb2Se4 through Cu resonant doping. *RSC Advances* **2015**, *5*, 99065-99073.
(105) Maier, S. A.: *Plasmonics: Fundamentals and Applications, 1st ed*; Springer-Verlag, 2007.
(106) Kelly, K. L.; Coronado, E.; Zhao, L. L.; Schatz, G. C. The optical properties of metal nanoparticles: The influence of size, shape, and dielectric environment. *J Phys Chem B* **2003**, *107*, 668-677.
(107) Maier, S. A.; Kik, P. G.; Atwater, H. A.; Meltzer, S.; Harel, E.; Koel, B. E.; Requicha, A. A. G. Local detection of electromagnetic energy transport below the diffraction limit in metal nanoparticle plasmon waveguides. *Nat Mater* **2003**, *2*, 229-232.
(108) Maier, S. A. Plasmonics: The promise of highly integrated optical devices. *Ieee J Sel Top Quant* **2006**, *12*, 1671-1677.
(109) Sannomiya, T.; Hafner, C.; Voros, J. In situ Sensing of Single Binding Events by Localized Surface Plasmon Resonance. *Nano Letters* **2008**, *8*, 3450-3455.
(110) Nie, Z. H.; Petukhova, A.; Kumacheva, E. Properties and emerging applications of self-assembled structures made from inorganic nanoparticles. *Nat Nanotechnol* **2010**, *5*, 15-25.
(111) Hah, J. H.; Mayya, S.; Hata, M.; Jang, Y. K.; Kim, H. W.; Ryoo, M.; Woo, S. G.; Cho, H. K.; Moon, J. T. Converging lithography by combination of electrostatic layer-by-layer self-assembly and 193 nm photolithography: Top-down meets bottom-up. *J Vac Sci Technol B* **2006**, *24*, 2209-2213.
(112) Lu, W.; Lieber, C. M. Nanoelectronics from the bottom up. *Nat Mater* **2007**, *6*, 841-850.
(113) Yu, G. H.; Lieber, C. M. Assembly and integration of semiconductor nanowires for functional nanosystems. *Pure Appl Chem* **2010**, *82*, 2295-2314.
(114) Langille, M. R.; Personick, M. L.; Zhang, J.; Mirkin, C. A. Bottom-Up Synthesis of Gold Octahedra with Tailorable Hollow Features. *J Am Chem Soc* **2011**, *133*, 10414-10417.
(115) Hu, J. T.; Odom, T. W.; Lieber, C. M. Chemistry and physics in one dimension: Synthesis and properties of nanowires and nanotubes. *Accounts Chem Res* **1999**, *32*, 435-445.
(116) Pan, Z. W.; Dai, Z. R.; Wang, Z. L. Nanobelts of semiconducting oxides. *Science* **2001**, *291*, 1947-1949.
(117) Haynes, C. L.; Van Duyne, R. P. Nanosphere lithography: A versatile nanofabrication tool for studies of size-dependent nanoparticle optics. *J Phys Chem B* **2001**, *105*, 5599-5611.

(118) Wallraff, G. M.; Hinsberg, W. D. Lithographic imaging techniques for the formation of nanoscopic features. *Chem Rev* **1999**, *99*, 1801-1821.
(119) Ito, T.; Okazaki, S. Pushing the limits of lithography. *Nature* **2000**, *406*, 1027-1031.
(120) Jin, R. C.; Cao, Y. W.; Mirkin, C. A.; Kelly, K. L.; Schatz, G. C.; Zheng, J. G. Photoinduced conversion of silver nanospheres to nanoprisms. *Science* **2001**, *294*, 1901-1903.
(121) Koh, A. L.; Bao, K.; Khan, I.; Smith, W. E.; Kothleitner, G.; Nordlander, P.; Maier, S. A.; McComb, D. W. Electron Energy-Loss Spectroscopy (EELS) of Surface Plasmons in Single Silver Nanoparticles and Dimers: Influence of Beam Damage and Mapping of Dark Modes. *ACS nano* **2009**, *3*, 3015-3022.
(122) Koh, A. L.; Fernandez-Dominguez, A. I.; McComb, D. W.; Maier, S. A.; Yang, J. K. W. High-Resolution Mapping of Electron-Beam-Excited Plasmon Modes in Lithographically Defined Gold Nanostructures. *Nano Letters* **2011**, *11*, 1323-1330.
(123) Maier, S. A.; Brongersma, M. L.; Kik, P. G.; Atwater, H. A. Observation of near-field coupling in metal nanoparticle chains using far-field polarization spectroscopy. *Phys Rev B* **2002**, *65*.
(124) Maier, S. A.; Kik, P. G.; Atwater, H. A. Observation of coupled plasmon-polariton modes in Au nanoparticle chain waveguides of different lengths: Estimation of waveguide loss. *Appl Phys Lett* **2002**, *81*, 1714-1716.
(125) Maier, S. A.; Atwater, H. A. Plasmonics: Localization and guiding of electromagnetic energy in metal/dielectric structures. *Journal of Applied Physics* **2005**, *98*.
(126) Sweatlock, L. A.; Maier, S. A.; Atwater, H. A.; Penninkhof, J. J.; Polman, A. Highly confined electromagnetic fields in arrays of strongly coupled Ag nanoparticles. *Phys Rev B* **2005**, *71*.
(127) Maier, S. A.; Friedman, M. D.; Barclay, P. E.; Painter, O. Experimental demonstration of fiber-accessible metal nanoparticle plasmon waveguides for planar energy guiding and sensing. *Appl Phys Lett* **2005**, *86*.
(128) Hashizume, J.; Koyama, F. Plasmon-enhancement of optical near-field of metal nanoaperture surface-emitting laser. *Appl Phys Lett* **2004**, *84*, 3226-3228.
(129) Dawson, P.; Puygranier, B. A. F.; Goudonnet, J. P. Surface plasmon polariton propagation length: A direct comparison using photon scanning tunneling microscopy and attenuated total reflection. *Phys Rev B* **2001**, *63*.
(130) Chang, P. C.; Fan, Z. Y.; Wang, D. W.; Tseng, W. Y.; Chiou, W. A.; Hong, J.; Lu, J. G. ZnO nanowires synthesized by vapor trapping CVD method. *Chem Mater* **2004**, *16*, 5133-5137.
(131) Hsieh, C. H.; Chang, M. T.; Chien, Y. J.; Chou, L. J.; Chen, L. J.; Chen, C. D. Coaxial Metal-Oxide-Semiconductor (MOS) Au/Ga2O3/GaN Nanowires. *Nano Letters* **2008**, *8*, 3288-3292.
(132) Johnson, M. C.; Aloni, S.; McCready, D. E.; Bourret-Courchesne, E. D. Controlled vapor-liquid-solid growth of indium, gallium, and tin oxide nanowires via chemical vapor transport. *Crystal Growth & Design* **2006**, *6*, 1936-1941.
(133) Nguyen, P.; Vaddiraju, S.; Meyyappan, M. Indium and tin oxide nanowires by vapor-liquid-solid growth technique. *J Electron Mater* **2006**, *35*, 200-206.

(134) Nie, T. X.; Chen, Z. G.; Wu, Y. Q.; Guo, Y. N.; Zhang, J. Z.; Fan, Y. L.; Yang, X. J.; Jiang, Z. M.; Zou, J. Fabrication of crystal alpha-Si3N4/Si-SiOx core-shell/Au-SiOx peapod-like axial double heterostructures for optoelectronic applications. *Nanotechnology* **2012**, *23*.
(135) Kolb, F. M.; Hofmeister, H.; Scholz, R.; Zacharias, M.; Gosele, U.; Ma, D. D.; Lee, S. T. Analysis of silicon nanowires grown by combining SiO evaporation with the VLS mechanism. *J Electrochem Soc* **2004**, *151*, G472-G475.
(135) Kuo, C. L.; Huang, M. H. The growth of ultralong and highly blue luminescent gallium oxide nanowires and nanobelts, and direct horizontal nanowire growth on substrates. *Nanotechnology* **2008**, *19*.
(137) Barreca, D.; Gasparotto, A.; Tondello, E. Metal/oxide interfaces in inorganic nanosystems: what's going on and what's next? *J Mater Chem* **2011**, *21*, 1648-1654.
(138) Papavassiliou, G. C. Surface-Plasmons in Small Au-Ag Alloy Particles. *J Phys F Met Phys* **1976**, *6*, L103-L105.
(139) McFarland, A. D.; Van Duyne, R. P. Single silver nanoparticles as real-time optical sensors with zeptomole sensitivity. *Nano Letters* **2003**, *3*, 1057-1062.
(140) Klar, T.; Perner, M.; Grosse, S.; von Plessen, G.; Spirkl, W.; Feldmann, J. Surface-plasmon resonances in single metallic nanoparticles. *Phys Rev Lett* **1998**, *80*, 4249-4252.
(141) Durig, U.; Pohl, D. W.; Rohner, F. Near-Field Optical-Scanning Microscopy. *Journal of Applied Physics* **1986**, *59*, 3318-3327.
(142) Oshikane, Y.; Kataoka, T.; Okuda, M.; Hara, S.; Inoue, H.; Nakano, M. Observation of nanostructure by scanning near-field optical microscope with small sphere probe. *Sci Technol Adv Mat* **2007**, *8*, 181-185.
(143) Batson, P. E. Correction. *Phys Rev Lett* **1982**, *49*, 1682-1682.
(144) Bosman, M.; Keast, V. J.; Watanabe, M.; Maaroof, A. I.; Cortie, M. B. Mapping surface plasmons at the nanometre scale with an electron beam. *Nanotechnology* **2007**, *18*.
(145) Nelayah, J.; Kociak, M.; Stephan, O.; de Abajo, F. J. G.; Tence, M.; Henrard, L.; Taverna, D.; Pastoriza-Santos, I.; Liz-Marzan, L. M.; Colliex, C. Mapping surface plasmons on a single metallic nanoparticle. *Nat Phys* **2007**, *3*, 348-353.
(146) Keast, V. J.; Bosman, M. Applications and theoretical simulation of low-loss electron energy-loss spectra. *Mater Sci Tech-Lond* **2008**, *24*, 651-659.
(147) Arslan, I.; Hyun, J. K.; Erni, R.; Fairchild, M. N.; Hersee, S. D.; Muller, D. A. Using Electrons As a High-Resolution Probe of Optical Modes in Individual Nanowires. *Nano Letters* **2009**, *9*, 4073-4077.
(148) Egerton, R. F. Electron energy-loss spectroscopy in the TEM. *Rep Prog Phys* **2009**, *72*.
(149) Schaffer, B.; Hohenester, U.; Trugler, A.; Hofer, F. High-resolution surface plasmon imaging of gold nanoparticles by energy-filtered transmission electron microscopy. *Phys Rev B* **2009**, *79*.
(150) Egerton, R. F. New techniques in electron energy-loss spectroscopy and energy-filtered imaging. *Micron* **2003**, *34*, 127-139.
(151) Kim, H.; Park, S.; Jin, C.; Lee, C. Enhanced Photoluminescence in Au-Embedded ITO Nanowires. *Acs Appl Mater Inter* **2011**, *3*, 4677-4681.

152) Hsieh, C. H.; Chou, L. J.; Lin, G. R.; Bando, Y.; Golberg, D. Nanophotonic Switch: Gold-in-Ga2O3 Peapod Nanowires. *Nano Letters* **2008**, *8*, 3081-3085.
(153) Wu, Y. J.; Hsieh, C. H.; Chen, P. H.; Li, J. Y.; Chou, L. J.; Chen, L. J. Plasmon Resonance Spectroscopy of Gold-in-Gallium Oxide Peapod and Core/Shell Nanowires. *ACS nano* **2010**, *4*, 1393-1398.
(154) Chen, P. H.; Hsieh, C. H.; Chen, S. Y.; Wu, C. H.; Wu, Y. J.; Chou, L. J.; Chen, L. J. Direct Observation of Au/Ga2O3 Peapodded Nanowires and Their Plasmonic Behaviors. *Nano Letters* **2010**, *10*, 3267-3271.
(155) Santoni, A.; Villacorta, F. J.; Rufoloni, A.; Mancini, A. Growth of Au-catalysed Si nanowires by low pressure chemical vapour deposition on Si(100) and amorphous Si surfaces. *J Phys-Condens Mat* **2006**, *18*, 10853-10859.
(156) Reina, A.; Jia, X.; Ho, J.; Nezich, D.; Son, H.; Bulovic, V.; Dresselhaus, M. S.; Kong, J. Large Area, Few-Layer Graphene Films on Arbitrary Substrates by Chemical Vapor Deposition. *Nano Letters* **2009**, *9*, 30-35.
(157) Jiang, H.; Sun, T.; Li, C. Z.; Ma, J. Peapod-like nickel@mesoporous carbon core-shell nanowires: a novel electrode material for supercapacitors. *Rsc Adv* **2011**, *1*, 954-957.
(158) Gao, J.; Chen, R.; Li, D. H.; Jiang, L.; Ye, J. C.; Ma, X. C.; Chen, X. D.; Xiong, Q. H.; Sun, H. D.; Wu, T. UV light emitting transparent conducting tin-doped indium oxide (ITO) nanowires. *Nanotechnology* **2011**, *22*.
(159) Liu, L. F.; Lee, W.; Scholz, R.; Pippel, E.; Gosele, U. Tailor-made inorganic nanopeapods: Structural design of linear noble metal nanoparticle chains. *Angew Chem Int Edit* **2008**, *47*, 7004-7008.
(160) Ye, M. M.; Zorba, S.; He, L.; Hu, Y. X.; Maxwell, R. T.; Farah, C.; Zhang, Q.; Yin, Y. D. Self-assembly of superparamagnetic magnetite particles into peapod-like structures and their application in optical modulation. *J Mater Chem* **2010**, *20*, 7965-7969.
(161) Luo, S. D.; Yao, L. D.; Chu, W. G.; Shen, J.; Zhang, Z. X.; Li, J. B.; Yi, J. H.; Yu, R. H.; Zhou, W. Y.; Xie, S. H. InN/In2O3 peapod nanostructures and conformal conversion templated from InN counterparts via thermal oxidation. *Nanotechnology* **2007**, *18*.
(162) Binet, L.; Gourier, D. Origin of the blue luminescence of beta-Ga2O3. *J Phys Chem Solids* **1998**, *59*, 1241-1249.
(163) Phillips, J. M.; Kwo, J.; Thomas, G. A.; Carter, S. A.; Cava, R. J.; Hou, S. Y.; Krajewski, J. J.; Marshall, J. H.; Peck, W. F.; Rapkine, D. H.; Vandover, R. B. Transparent Conducting Thin-Films of Gaino3. *Appl Phys Lett* **1994**, *65*, 115-117.
(164) He, H. Y.; Orlando, R.; Blanco, M. A.; Pandey, R.; Amzallag, E.; Baraille, I.; Rerat, M. First-principles study of the structural, electronic, and optical properties of Ga2O3 in its monoclinic and hexagonal phases. *Phys Rev B* **2006**, *74*.
(165) Werfel, F.; Brummer, O. Corundum Structure Oxides Studied by Xps. *Phys Scripta* **1983**, *28*, 92-96.
(166) Kim, H.; Gilmore, C. M.; Pique, A.; Horwitz, J. S.; Mattoussi, H.; Murata, H.; Kafafi, Z. H.; Chrisey, D. B. Electrical, optical, and structural properties of indium-tin-oxide thin films for organic light-emitting devices. *Journal of Applied Physics* **1999**, *86*, 6451-6461.

(167) Frank, G.; Olazcuaga, R.; Rabenau, A. Occurrence of Corundum-Type Indium(Iii) Oxide under Ambient Conditions. *Inorganic Chemistry* **1977**, *16*, 1251-1253.
(168) Wagner, R. S.; Ellis, W. C. Vapor-Liquid-Solid Mechanism of Single Crystal Growth. *Appl. Phys. Lett.* **1964**, *4*, 89–90.
(169) Wu, Y.; Yang, P. Direct Observation of Vapor−Liquid−Solid Nanowire Growth. *J. Am. Chem. Soc.* **2001**, *123*, 3165–3166.
(170) Lu, W.; Lieber, C. M. Semiconductor Nanowires. *J. Phys. Appl. Phys.* **2006**, *39*, R387.
(171) Cui, Y.; Wei, Q.; Park, H.; Lieber, C. M. Nanowire Nanosensors for Highly Sensitive and Selective Detection of Biological and Chemical Species. *Science* **2001**, *293*, 1289–1292.
(172) Kolmakov, A.; Zhang, Y.; Cheng, G.; Moskovits, M. Detection of CO and O2 Using Tin Oxide Nanowire Sensors. *Adv. Mater.* **2003**, *15*, 997–1000.
(173) Yu, C.; Hao, Q.; Saha, S.; Shi, L.; Kong, X.; Wang, Z. L. Integration of Metal Oxide Nanobelts with Microsystems for Nerve Agent Detection. *Appl. Phys. Lett.* **2005**, *86*, 63101.
(174) Baxter, J. B.; Aydil, E. S. Nanowire-Based Dye-Sensitized Solar Cells. *Appl. Phys. Lett.* **2005**, *86*, 53114-053114–3.
(175) Gubbala, S.; Chakrapani, V.; Kumar, V.; Sunkara, M. K. Band-Edge Engineered Hybrid Structures for Dye-Sensitized Solar Cells Based on SnO2 Nanowires. *Adv. Funct. Mater.* **2008**, *18*, 2411–2418.
(176) Krishnamoorthy, T.; Tang, M. Z.; Verma, A.; Nair, A. S.; Pliszka, D.; Mhaisalkar, S. G.; Ramakrishna, S. A Facile Route to Vertically Aligned Electrospun SnO2 Nanowires on a Transparent Conducting Oxide Substrate for Dye-Sensitized Solar Cells. *J. Mater. Chem.* **2012**, *22*, 2166.
(177) Duan, X.; Huang, Y.; Cui, Y.; Wang, J.; Lieber, C. M. Indium Phosphide Nanowires as Building Blocks for Nanoscale Electronic and Optoelectronic Devices. *Nature* **2001**, *409*, 66–69.
(178) Cui, Y.; Zhong, Z.; Wang, D.; Wang, W. U.; Lieber, C. M. High Performance Silicon Nanowire Field Effect Transistors. *Nano Lett.* **2003**, *3*, 149–152.
(179) Park, M.-S.; Wang, G.-X.; Kang, Y.-M.; Wexler, D.; Dou, S.-X.; Liu. Preparation and Electrochemical Properties of SnO2 Nanowires for Application in Lithium-Ion Batteries. *Angew. Chem. Int. Ed.* **2007**, 750–753.
(180) Ko, Y.-D.; Kang, J.-G.; Park, J.-G.; Lee, S.; Kim, D.-W. Self-Supported SnO2 Nanowire Electrodes for High-Power Lithium-Ion Batteries. *Nanotechnology* **2009**, *20*, 455701.
(181) Chueh, Y.-L.; Ko, M.-T.; Chou, L.-J.; Chen, L.-J.; Wu, C.-S.; Chen, C.-D. TaSi2 Nanowires: A Potential Field Emitter and Interconnect. *Nano Lett.* **2006**, *6*, 1637–1644.
(182) Kaur, J.; Kumar, R.; Bhatnagar, M. C. Effect of Indium-Doped SnO2 Nanoparticles on NO2 Gas Sensing Properties. *Sens. Actuators B Chem.* **2007**, *126*, 478–484.
(183) Salehi, A.; Gholizade, M. Gas-Sensing Properties of Indium-Doped SnO2 Thin Films with Variations in Indium Concentration. *Sens. Actuators B Chem.* **2003**, *89*, 173–179.

(184) Salehi, A. Selectivity Enhancement of Indium-Doped SnO2 Gas Sensors. *Thin Solid Films* **2002**, *416*, 260–263.
(185) Gao, J.; Chen, R.; Li, D. H.; Jiang, L.; Ye, J. C.; Ma, X. C.; Chen, X. D.; Xiong, Q. H.; Sun, H. D.; Wu, T. UV Light Emitting Transparent Conducting Tin-Doped Indium Oxide (ITO) Nanowires. *Nanotechnology* **2011**, *22*, 195706.
(186) Wang, D.; Chen, G.; Gong, M. Effects of Indium Doping Concentration on the Morphology and Electrical Properties of One-Dimensional SnO2 Nanostructures Prepared by a Molten Salt Method. *Sci. China Phys. Mech. Astron.* **2012**, *55*, 1599–1603.
(187) Schmidt, V.; Wittemann, J. V.; Senz, S.; Gösele, U. Silicon Nanowires: A Review on Aspects of Their Growth and Their Electrical Properties. *Adv. Mater.* **2009**, *21*, 2681–2702.
(188) Schmidt, V.; Wittemann, J. V.; Gösele, U. Growth, Thermodynamics, and Electrical Properties of Silicon Nanowires†. *Chem. Rev.* **2010**, *110*, 361–388.
(189) Givargizov, E. I. Fundamental Aspects of VLS Growth. *J. Cryst. Growth* **1975**, *31*, 20–30.
(190) Kodambaka, S.; Tersoff, J.; Reuter, M. C.; Ross, F. M. Diameter-Independent Kinetics in the Vapor-Liquid-Solid Growth of Si Nanowires. *Phys. Rev. Lett.* **2006**, *96*, 96105.
(191) Roper, S. M.; Davis, S. H.; Norris, S. A.; Golovin, A. A.; Voorhees, P. W.; Weiss, M. Steady Growth of Nanowires via the Vapor-Liquid-Solid Method. *J. Appl. Phys.* **2007**, *102*, 34304.
(192) Ryu, S.; Cai, W. Molecular Dynamics Simulations of Gold-Catalyzed Growth of Silicon Bulk Crystals and Nanowires. *J. Mater. Res.* **2011**, *26*, 2199–2206.
(193) Wang, H.; Zepeda-Ruiz, L. A.; Gilmer, G. H.; Upmanyu, M. Atomistics of Vapour–liquid–solid Nanowire Growth. *Nat. Commun.* **2013**, *4*, 1956.
(194) Hannon, J. B.; Kodambaka, S.; Ross, F. M.; Tromp, R. M. The Influence of the Surface Migration of Gold on the Growth of Silicon Nanowires. *Nature* **2006**, *440*, 69–71.
(195) Sutter, E.; Sutter, P. Au-Induced Encapsulation of Ge Nanowires in Protective C Shells. *Adv. Mater.* **2006**, *18*, 2583–2588.
(196) Sutter, E. A.; Sutter, P. W. Size-Dependent Phase Diagram of Nanoscale Alloy Drops Used in Vapor−Liquid−Solid Growth of Semiconductor Nanowires. *ACS Nano* **2010**, *4*, 4943–4947.
(197) Sutter, E.; Sutter, P. Formation and Stabilization of Single-Crystalline Metastable AuGe Phases in Ge Nanowires. *Nanotechnology* **2011**, *22*, 295605.
(198) Sutter, E. A.; Sutter, P. W.; Uccelli, E.; Fontcuberta i Morral, A. Supercooling of Nanoscale Ga Drops with Controlled Impurity Levels. *Phys. Rev. B* **2011**, *84*, 193303.
(199) Givargizov, E. I.; Babasian, P. A. Negative Whiskers Formed by Solid-Liquid-Vapor Mechanism during Vaporization of ZnS. *J. Cryst. Growth* **1977**, *37*, 140–146.
(200) Kim, B.-J.; Stach, E. A. Desorption Induced Formation of Negative Nanowires in GaN. *J. Cryst. Growth* **2011**, *324*, 119–123.
(201) Okamoto, H.; Massalski, T. B. The Au−Sn (Gold-Tin) System. *Bull. Alloy Phase Diagr.* **1984**, *5*, 492–503.

(202) Klamchuen, A.; Yanagida, T.; Kanai, M.; Nagashima, K.; Oka, K.; Kawai, T.; Suzuki, M.; Hidaka, Y.; Kai, S. Role of Surrounding Oxygen on Oxide Nanowire Growth. *Appl. Phys. Lett.* **2010**, *97*, 73114.
(203) Kim, H.; Park, S.; Jin, C.; Lee, C. Enhanced Photoluminescence in Au-Embedded ITO Nanowires. *ACS Appl. Mater. Interfaces* **2011**, 3, 4677–4681.
(204) Jin, R.; Charles Cao, Y.; Hao, E.; Metraux, G. S.; Schatz, G. C.; Mirkin, C. A. Controlling anisotropic nanoparticle growth through plasmon excitation. *Nature* **2003**, *425*, 487-490.
(205) Koh, A. L.; Fernández-Domínguez, A. I.; McComb, D. W.; Maier, S. A.; Yang, J. K. W. High-Resolution Mapping of Electron-Beam-Excited Plasmon Modes in Lithographically Defined Gold Nanostructures. *Nano Letters* **2011**, *11*, 1323-1330.
(206) Adireddy, S.; Carbo, C. E.; Rostamzadeh, T.; Vargas, J. M.; Spinu, L.; Wiley, J. B. Peapod-Type Nanocomposites through the In Situ Growth of Gold Nanoparticles within Preformed Hexaniobate Nanoscrolls. *Angewandte Chemie International Edition* **2014**, *53*, 4614-4617.
(207) Wak, E.-S.; Henzie, J.; Chang, S.-H.; Gray, S. K.; Schatz, G. C.; Odom, T. W. Surface Plasmon Standing Waves in Large-Area Subwavelength Hole Arrays. *Nano Letters* **2005**, *5*, 1963-1967.
(208) Rochon, P. L.; Lévesque, L. Standing wave surface plasmon mediated forward and backward scattering. *Opt. Express* **2006**, *14*, 13050-13055.

# VITA

## YAO-JEN, CHANG

**Education:**

08/2007- 05/2010 **Murray State University (U.S.A.)**
***Master of Science in Chemistry***

09/2001- 06/2005 **TamKang University (Taiwan)**
***Bachelor of Science in Chemistry***

**Teaching Experience:**

08/2016- 12/2016 **Teaching assistant for General Chemistry recitation, University of Kentucky**

01/2015- 05/2015 **Teaching assistant for Physical Chemistry lab, University of Kentucky**

01/2014- 05/2014, 08/2014- 12/2014, 08/2010- 05/2012 **Teaching assistant for General Chemistry lab, University of Kentucky**

**Research Experience:**

05/2015- 08/2016, 05/2014- 08/2014, 05/2012- 12/2013, 05/2012- 12/2012 **Research assistant, University of Kentucky**

**Publication list:**

(1) Yu, L.; Riddle, A.; Wang, S.; Sundararajan, A.; Thompson, J.; Chang, Y.; Park, M.; Ambrose Seo, S.; Guiton, B. Solid-Liquid-Vapor Synthesis of Negative Metal Oxide Nanowire Arrays. *Chem. Matter.* **2016**, 28(24), 8924-8829.

(2) Li, G.; Yu, L.; Hudak, B.; Chang, Y.; Baek, H.; Sundararajan, A.; Strachan, D.; Yi, G.; Guiton, B. Direct Observation Of Li Diffusion In Li-Doped Zno Nanowires. *Materials Research Express* **2016**, *3*, 054001.

(3) Hudak, B.; Chang, Y.; Yu, L.; Li, G.; Edwards, D.; Guiton, B. Real-Time Observation Of The Solid–Liquid–Vapor Dissolution Of Individual Tin(IV) Oxide Nanowires. *ACS Nano* **2014**, *8*, 5441-5448.

(4) Zahran, E.; Bedford, N.; Nguyen, M.; Chang, Y.; Guiton, B.; Naik, R.; Bachas, L.; Knecht, M. Light-Activated Tandem Catalysis Driven By Multicomponent Nanomaterials. *J. Am. Chem. Soc.* **2014**, *136*, 32-35.

(5) Li, G.; Sundararajan, A.; Mouti, A.; Chang, Y.; Lupini, A.; Pennycook, S.; Strachan, D.; Guiton, B. Synthesis And Characterization Of P–N Homojunction-Containing Zinc Oxide Nanowires. *Nanoscale* **2013**, *5*, 2259.

Google scholar:

https://scholar.google.com/citations?view_op=list_works&hl=en&user=dHqa1wYAAAAAJ&gmla=AJsN-F4Ie2SV87qw2xnJ4xE1w7qzfY1XxEa_iVTrxL5-FDfLMXns2fLALqlAtUTmva7fpA9mTq822zA1pFpO22yeQHUdXJJLhYrV1JiKduBDBGp-3aARCXM